



HAL
open science

Nuclear quantum effects in hydrated nanocrystals

Sofiane Schaack

► **To cite this version:**

Sofiane Schaack. Nuclear quantum effects in hydrated nanocrystals. Quantum Physics [quant-ph]. Sorbonne Université, 2019. English. NNT : 2019SORUS370 . tel-03008642

HAL Id: tel-03008642

<https://theses.hal.science/tel-03008642>

Submitted on 16 Nov 2020

HAL is a multi-disciplinary open access archive for the deposit and dissemination of scientific research documents, whether they are published or not. The documents may come from teaching and research institutions in France or abroad, or from public or private research centers.

L'archive ouverte pluridisciplinaire **HAL**, est destinée au dépôt et à la diffusion de documents scientifiques de niveau recherche, publiés ou non, émanant des établissements d'enseignement et de recherche français ou étrangers, des laboratoires publics ou privés.



PhD Thesis

Speciality : Physics

Doctoral School : 397
Physics and Chemistry of Materials

to obtain the title of :

PhD of Sorbonne University

Defended by
Sofiane Schaack

Nuclear Quantum Effects in Hydrated Nanocrystals

prepared at Institut des NanoSciences de Paris
Under the supervision of Philippe Depondt and Fabio Finocchi

Jury :

Reviewers : Magali Benoit CEMES - CNRS
Francesco Sciortino Sapienza University

Advisors : Philippe Depondt INSP - Sorbonne University
Fabio Finocchi INSP - CNRS

Examinators : Christian Bonhomme LCMCP - Sorbonne University
José Teixeira CEA - CNRS
Livia E. Bove IMPMC - CNRS

Abstract

The quantum nature of nuclei yields unexpected and often paradoxical behaviors. Hydrogen, because of the lightness of its nucleus, is a most likely candidate for such effects. Indeed, as demonstrated about 20 years ago,¹ the pressure-induced transition from the proton-disordered ice VII to the hydrogen-bond symmetric ice X phase is significantly downshifted by the proton zero-point energy and tunneling. Using up-to-date methods and increased simulation capabilities, we now investigate more complex hydrated systems, namely, the brucite minerals ($\text{Mg}(\text{OH})_2$), the methane hydrate ($\text{CH}_4\text{-H}_2\text{O}$) and the sodium hydroxide (NaOH), which display complex mechanisms driven by the proton quantum properties.

Brucite exhibits the coexistence of thermally activated hopping and quantum tunneling with opposite behaviors as pressure is increased. The unforeseen consequence is a pressure sweet spot for proton diffusion. Simultaneously, pressure gives rise to a “quantum” quasi two-dimensional hydrogen plane, non-trivially connected with proton diffusion.

Methane hydrate displays an important increase of the inter-molecular interactions between water and enclosed methane molecules. In contrast with ice, the hydrogen bond transition does not shift by H/D isotopic substitution. This is explained by an important delocalization of the proton which also triggers a transition toward a new MH-IV methane hydrate phase, stable up to 150 GPa which represents the highest pressure reached to date by any hydrate.

Sodium hydroxide has a phase transition below room temperature at ambient pressure only in its deuterated version. This radical isotope effect can be explained by the quantum delocalization of the proton as compared with deuteron shifting the temperature-induced phase transition of NaOD towards a pressure-induced one in NaOH.

Résumé

La nature quantique des noyaux produit des comportements inattendus et souvent paradoxaux. L'hydrogène, en raison de la légèreté de son noyau, est le candidat le plus susceptible de présenter de tels comportements. En effet, comme il a été démontré il y a environ 20 ans,¹ la transition, induite par la pression, de la glace VII présentant des protons désordonnés à la phase de glace X, aux liaisons hydrogènes symétriques, était considérablement abaissée par le biais de l'énergie de point-zéro et des effets tunnels relatifs aux protons. À l'aide de méthodes modernes et grâce à l'augmentation des capacités computationnelles, nous pouvons maintenant étudier des systèmes physiques plus complexes. Lors de cette thèse, nous nous sommes attardés sur l'étude de trois systèmes hydratés, à savoir la Brucite ($\text{Mg}(\text{OH})_2$), l'hydrate de méthane ($\text{CH}_4\text{-H}_2\text{O}$) et l'hydroxyde de sodium (NaOH), dont les mécanismes complexes sont déterminés par les propriétés quantiques des protons.

Au sein des brucites coexistent deux effets en compétition: un mécanisme de réorientation thermiquement activé, et un processus de dissociation déclenché par les effets quantiques nucléaires. Ces deux effets s'opposent à mesure que la pression augmente, entraînant l'existence d'un point de pression favorable à la diffusion des protons. Simultanément, la pression donne naissance à un plan d'hydrogène "quantique" quasi bidimensionnel, non trivialement lié à la diffusion de ces derniers.

Les hydrates de méthane présentent une augmentation importante des interactions intermoléculaires entre l'eau et les molécules de méthane qui y sont enfermées. Contrairement à la glace, la transition de symétrisation de la liaison hydrogène ne change pas par substitution isotopique H/D. Ceci s'explique par une importante délocalisation du proton qui déclenche également une transition vers une nouvelle phase d'hydrate de méthane que nous avons découverte, le MH-IV, stable jusqu'à 150 GPa, qui représente la pression la plus élevée atteinte par tout hydrate connu à ce jour.

L'hydroxyde de sodium présente une transition de phase en-dessous de la température ambiante et à pression ambiante uniquement dans sa version deutérée. Cet effet isotopique important peut s'expliquer par la plus grande délocalisation quantique et par l'importance de l'énergie de point-zéro du proton par rapport au deutérium. De façon surprenante, la substitution isotopique H/D change la transition induite par la température dans NaOD en une transition déclenchée par la pression dans NaOH.

Acknowledgements

The realization of this work has been permitted with the help of the following persons who supported me at each stage of these three years.

I am deeply grateful to my advisors. Philippe Depondt whose availability, experience and openness have provided me with the most useful tools for my thesis, for his support and our long discussions about so many topics (planes included). Fabio Finocchi, for his in-depth comments throughout these three years, and his sharp eye which allowed this thesis to reach its current level.

I also thank Livia E. Bove, for our collaboration rich in results and publications.

For sharing their knowledge and for our thoughtful discussions, I thank Simon Huppert and Fabio Pietrucci.

I thank Yael Bronstein for her work without which the present study might not have been done. For their support and advice, I thank all the members of my thesis supervision committee, José Teixeira, Jean-Noël Aqua, and Annick Loiseau, as well as the head of the doctoral school at the time, Christian Bonhomme.

I would like to express my gratitude to the whole administrative team of the INSP and the ED 397, in particular to Valérie Guezo and Hakima Si Bachir for their help and cheerfulness.

For their time and reviews, I thank the members of my jury as well as all anonymous referees who helped to improve every stage of my work.

Special thanks to Massimiliano Marangolo, Nadine Witkowski, and Laurent Legrand without whom this Ph.D. would not have been possible.

For their support, understanding, for all these shared moments, I thank Elisa Meriggio, Maya Messaykeh, Clément Dulong, Thomas Plé, with special attention for “Dr. Mathieu Moog and Mr. Otter”, for our long discussions and his jokes.

For dragging me out of my work routine and for their precious friendship, thanks to Florian, Raphaël, Pierre-Antoine, Alan, Nicolas, and all the others I did not mention although essential.

I am especially grateful for the support and understanding that I received from my family.

Finally, to the one who saw all the facets of this road, whose uncompromising support helped me to overcome all potential barriers. I dedicate this work to Charlotte Hauser.

A musical score for a piano piece by Frédéric F. Chopin. The score is written for two staves, treble and bass clef. The tempo is marked "Moderato" with a metronome marking of quarter note = 60. The key signature has one flat (B-flat). The score begins with a treble clef staff containing a few notes, followed by a double bar line. The bass clef staff starts with a whole note chord. The main melody is in the treble clef, starting with a half note chord, followed by a series of eighth and sixteenth notes. There are dynamic markings "A" and "p" (piano). The score ends with a double bar line and a final chord in the treble clef.

Frédéric F. Chopin (1836)

Table of Contents

Abbreviations	xiii
Nomenclature	xv
Introduction	1
I State of the art	5
1 Theoretical framework	7
1.1 Introduction	7
1.2 Density matrix	8
1.2.1 Pure and mixed states	8
1.2.2 Time evolution	10
1.2.3 Thermal equilibrium	13
1.3 Linear Response theory	15
1.3.1 Response function	16
1.3.2 Generalized susceptibility	17
1.3.3 Fluctuations	18
1.3.4 Relaxation	19
1.3.5 Dissipation	19
1.3.6 Fluctuation-Dissipation theorem	20
1.4 Ab-Initio Molecular Dynamics	22
1.4.1 The Born-Oppenheimer approximation	22
1.4.2 The Density Functional Theory	24
2 Modelisation of Nuclear quantum effects	29
2.1 Introduction	29
2.2 Langevin methods	30
2.2.1 Langevin equation	30
2.2.2 Quantum Thermal Bath	32
2.3 Path integral formalism	34
2.3.1 Path Integral Molecular Dynamics	36
2.3.2 Ring Polymer Molecular Dynamics	41
2.4 Conclusion	43

3	Phase transitions description	45
3.1	Introduction	45
3.2	Minimum energy path sampling with Nudged Elastic Band	46
3.3	Free energy sampling with Metadynamics	48
3.3.1	Path collective variables and the path invariant vector	50
3.4	Conclusion	52
II	Investigation of Nuclear Quantum Effects	55
1	Quantum driven proton diffusion in brucite minerals	57
1.1	Introduction	57
1.2	Brucite mineral structure	58
1.3	Proton diffusion mechanism	58
1.3.1	In plane reorientation	59
1.3.2	Out of plane dissociation	60
1.3.3	Proton diffusion sweet spot	63
1.4	Comparison with Portlandite	65
1.5	Conclusion	67
2	Methane hydrate: towards a quantum-induced phase transition	69
2.1	Introduction	69
2.1.1	MH-III structure	70
2.2	MH-III under pressure	73
2.2.1	Spectral analysis	73
2.2.2	Methane ordering and locking-in	75
2.2.3	Methane-Water interaction	77
2.3	The methane hydrate IIIs	81
2.3.1	From MH-III to MH-IIIs	82
2.3.2	Nuclear quantum effects and isotopic substitution	83
2.4	The methane hydrate IV	90
2.4.1	Structural properties	91
2.4.2	Hydrogen bond symmetrization: MH-IVs	93
2.4.3	Vibrational properties	95
2.5	Transition description	97
2.5.1	Transition stages	97
2.5.2	Stability of the ice frame	98
2.5.3	Transition path	100
2.6	Conclusion	103
3	The Quantum equilibrium structure of sodium hydroxide	105
3.1	Introduction	105
3.2	Sodium hydroxide structure	106
3.3	Quantum mechanical description of structural properties	106
3.4	Towards a dynamical paraelectric state	109
3.5	From temperature- to pressure-induced transition	112
3.6	Conclusion	114

Conclusion	117
Appendices	121
A Brucite minerals	123
A.1 Computational details	123
B Methane hydrate	125
B.1 Computational details	125
B.2 Methane rotation characterization	126
C Sodium hydroxide	129
C.1 Computational details	129
C.2 Volume optimization	130
Communications	133
Bibliography	142

Abbreviations

CMD	Centroid Molecular Dynamics.
CV	Collective Variable.
DFT	Density Functional Theory.
DoF	Degrees of Freedom.
FDT	Fluctuation-Dissipation Theorem.
GGA	Generalized Gradient Approximation.
GLE	Generalized Langevin Equation.
HEG	Homogeneous Electron Gas.
LDA	Local Density Approximation.
MD	Molecular Dynamics.
MEP	Minimum Energy Reaction Path.
MTD	Metadynamics.
NEB	Nudged Elastic Band.
NQE	Nuclear Quantum Effects.
OPDF	Orientalional Probability Density Function.
Path CVs	Path Collective Variables.
PI	Path Integral.
PIGLET	Path Integral Generalized Langevin Equation Thermostat.
PIMD	Path Integral Molecular Dynamics.
PIV	Path Invariant Vector.
QTB	Quantum Thermal Bath.
RPMD	Ring Polymer Molecular Dynamics.
ZPEL	Zero-Point Energy Leakage.

Nomenclature

β	Inverse temperature.
\hbar	Reduced Planck constant.
λ_B	de Broglie wavelength.
\mathcal{Z}	Partition function.
k_b	Boltzmann constant.

Introduction

The use of quantum mechanics in condensed matter simulations is routinely confined to the description of the electronic properties, while the behavior of nuclei remains in the domain of Newton's classical dynamics. If this framework provides a good approximation for heavy particles in general, nuclei are not in principle restricted to a classical description. In some cases, they can exhibit wave behavior as other quantum particles, and show what is known as Nuclear Quantum Effects (NQE). The limit between the classical and quantum domains is sometimes unclear, and can be appreciated through the wave nature of particles as brought out by L. de Broglie in 1924 referring to Einstein's 1905 discovery of photons and wave-particle duality: each particle having a momentum can be seen as a wave with a wavelength that describes the wave packet spread related to the particle.

L. de Broglie thermal wavelength

$$\lambda_B = \frac{h}{\sqrt{2\pi mk_B T}}$$

Where k_B is the Boltzmann constant, m the mass of the particle, T the temperature and h the Planck constant.

Therefore, for cases in which the de Broglie wavelength is of the order of magnitude of the characteristic length scale of its environment (lattice parameters, inter-atomic distances, mean free path ...), the particle quantum nature cannot be neglected, and the classical approximation cannot be applied. In the present study, we aim at investigating cases for which the quantum nature of nuclei, in particular, zero-point motion and tunneling effect, is essential to fully describe their behavior. From the de Broglie thermal wavelength, one can observe that light nuclei or low-temperature systems are those for which nuclear quantum effects are in principle significant. In this thesis, we mainly address the nuclear effects that happen for light nuclei, such as hydrogen and deuterium atoms present in hydrated crystals, usually at ambient temperature, for which the proton de Broglie wavelength is about 1 Å, therefore comparable to the typical O-H bond length. However, we will see that the strength of nuclear quantum effects can be highly unpredictable as it results from a subtle balance between localization, usually induced by the potential, and quantum spread, which results from the wave-particle duality at the typical λ_B length scale.

Among the different approaches to address NQE within ab-initio simulations, the Path Integral (PI) methods,² based on Feynman description of quantum mechanics, and the so-called Quantum Thermal Bath (QTB),³ arising from the Langevin equation, have been successfully employed for several systems.^{4,5,6,7} In particular, the description of the ice VII → X transition, have been shown to be quantum driven through Path Integral Molecular Dynamics (PIMD)¹ and confirmed later with the QTB.⁴ This transition of the ice represents a case-study where the importance of the nuclear quantum effects along a one-dimensional double-well potential is now well understood. However, when other degrees of freedom are involved, sophisticated and somehow non-intuitive effects can arise. In the present study, we therefore address complex systems where the quantum behavior of nuclei leads to complex mechanisms sometimes entangled with other phenomena.

This thesis is organized as follows:

- The first part is devoted to the theory and the description of the different numerical approaches we used in the following. In particular, in Chapter 1 we introduce the density operator formalism of quantum mechanics leading to the PI formalism, then we recall the basis of the Linear response theory and the fluctuation-dissipation theorem at the root of the QTB and Ring Polymer Molecular Dynamics (RPMD) methods. This first chapter then ends with the description of Born Oppenheimer molecular dynamics and a quick reminder of the electronic quantum description with the Density Functional Theory (DFT).

Then, in Chapter 2 we describe the different approaches to treat nuclear quantum effects in our simulations. Firstly, we introduce the Langevin equation and related QTB approach. Secondly, we describe the Feynman path integral formalism leading to the PIMD method allowing a correct quantum statistical description of nuclei. To conclude this chapter, we present the RPMD method, which allows to approximate time correlation functions within the PI formalism.

Finally, in Chapter 3 we describe the Nudged Elastic Band (NEB) method allowing one to have access to the minimum energy path for phase transition descriptions, and we also present the Metadynamics (MTD) giving rise to a free energy sampling along the chosen Path Collective Variables (Path CVs).

- The second part presents the different quantum driven mechanisms observed through our investigation of real physical systems.

In Chapter 1, we present the case of proton diffusion in Brucite minerals $X(OH)_2$ ($X= Mg, Ca, Ni \dots$), which is triggered by the presence of nuclear quantum effects enhanced by pressure. We will see that the competition between quantum driven and thermally driven mechanisms leads to a pressure sweet spot for the proton diffusion in the system and that within its mineral family, Brucite could be a specific case. In this chapter, we will also show how the quantum delocalization of the proton could induce the creation of a 2D proton plane.

Then in Chapter 2, we present a study of methane hydrate (CH_4-H_2O) under high pressure. We first describe how the methane molecules confined within a hydrogen-bonded water frame reorganize into an orientationally ordered system upon compression, leading to an interaction enhancement between the latter molecules and their environment. Then, we present the quantum driven hydrogen bond symmetrization of MH-III, which displays important differences with the ice VII \rightarrow X phase transition regarding H/D isotopic substitution. In particular, we will see how a two-dimensional description of the quantum delocalization impacts this mechanism. Then, we will present a new high-pressure phase we discovered, the MH-IV, and describe its quantum induced phase transition.

Finally, in Chapter 3, we present the case of sodium hydroxide (NaOH) in which nuclear quantum effects change the structural stability of the system, leading to a strong isotope effect. In particular, we will describe why a phase transition occurs for NaOD with increasing temperature, and disappears while substituting deuterons with protons. This analysis of sodium hydroxide will also allow us to compare the equivalence of temperature and pressure effect within this system.

Part I

State of the art

1	Theoretical framework	7
1.1	Introduction	7
1.2	Density matrix	8
1.2.1	Pure and mixed states	8
1.2.2	Time evolution	10
1.2.3	Thermal equilibrium	13
1.3	Linear Response theory	15
1.3.1	Response function	16
1.3.2	Generalized susceptibility	17
1.3.3	Fluctuations	18
1.3.4	Relaxation	19
1.3.5	Dissipation	19
1.3.6	Fluctuation-Dissipation theorem	20
1.4	Ab-Initio Molecular Dynamics	22
1.4.1	The Born-Oppenheimer approximation	22
1.4.2	The Density Functional Theory	24
2	Modelisation of Nuclear quantum effects	29
2.1	Introduction	29
2.2	Langevin methods	30
2.2.1	Langevin equation	30
2.2.2	Quantum Thermal Bath	32
2.3	Path integral formalism	34
2.3.1	Path Integral Molecular Dynamics	36
2.3.2	Ring Polymer Molecular Dynamics	41
2.4	Conclusion	43
3	Phase transitions description	45
3.1	Introduction	45
3.2	Minimum energy path sampling with Nudged Elastic Band	46
3.3	Free energy sampling with Metadynamics	48
3.3.1	Path collective variables and the path invariant vector	50
3.4	Conclusion	52

Theoretical framework

1.1 Introduction

In this part, we introduce the necessary theoretical foundations to describe the different methods allowing investigation of NQE within the same framework.

First, we will introduce the formalism of quantum mechanics via the density operator and its properties both at equilibrium and its evolution under an external perturbation. It will naturally be involved in the description of the Feynman PI formalism, and also will be an essential asset to derive the Fluctuation-Dissipation Theorem (FDT) from the Linear Response Theory framework. The latter will be treated in a second part, where the different definitions of the generalized susceptibility, correlations functions, and spectral densities will be introduced as well as their different properties leading to the FDT. Finally, in the present work, all the electronic description and the inter-atomic forces are derived from the DFT within the Born-Oppenheimer approximation. Therefore, a brief description of the Kohn-Sham equations and inherent approximation will be provided.

The reader could find more detailed information about the different subjects in the following resources this document is inspired by:

Density matrix: Mark Tuckerman. *Statistical mechanics: theory and molecular simulation*. Oxford university press, 2010

Linear response theory: Noëlle Pottier. *Physique statistique hors d'équilibre-Processus irréversibles linéaires*. EDP Sciences, 2012; Nicolas Borghini. *Topics in Nonequilibrium Physics*. [Online; accessed 05-May-2019]. 2016. URL: <https://www.physik.uni-bielefeld.de/~borghini/Teaching/Nonequilibrium/Nonequilibrium.pdf>

Density Functionnal Theory: Fabio Finocchi. *Density Functional Theory for beginners*. [Online; accessed 05-May-2019]. 2011. URL: http://www.attacalite.com/wp-content/uploads/2017/04/pdf_DFT4beginners.pdf

1.2 Density matrix

While dealing with quantum systems, one usually describe their states with the related wave function $|\Psi\rangle$ of Hilbert space \mathcal{H} . This definition only refers to so-called “pure” states which are unequivocally defined by a single state vector. However, in a statistical ensemble representation, we have to treat a statistical mixture of pure states or so defined “mixed” states. The density operator here described allows describing both pure and mixed states in a generalized formulation. In this section, we will first define the density matrix of a pure state, generalize it to include mixed states and then describe its properties. In the second part, we will introduce the time evolution of the density matrix and operators in this representation and study the case of perturbed Hamiltonian. Finally, we will define the density operator for a system in thermal equilibrium.

1.2.1 Pure and mixed states

• Pure states

Quantum systems states are usually described by the related eigenfunctions $|\Psi\rangle$ which can be expressed as a linear combination of basis state vectors $\{|U_n\rangle\}$:

$$|\Psi\rangle = \sum_n c_n |U_n\rangle \quad (1.2.1)$$

where $\sum_n |c_n|^2 = 1$.

This state vector describes a “pure” state and in this representation any operator \hat{A} has its expectation value defined as:

$$\langle \hat{A} \rangle = \langle \Psi | \hat{A} | \Psi \rangle \quad (1.2.2)$$

We now introduce another formulation of quantum states with the density operator $\hat{\rho}$ being the outer product of the pure state vector and its conjugate:

$$\hat{\rho} = |\Psi\rangle\langle\Psi| \quad (1.2.3)$$

which matrix element in the $\{|U_n\rangle\}$ representation is:

$$\rho_{mn} = \langle U_m | \hat{\rho} | U_n \rangle = c_n^* c_m \quad (1.2.4)$$

Both representations are identical, and one can notice that the integral $\langle \xi | \hat{\rho} | \xi \rangle$ defines the probability to find the system in the state $|\xi\rangle$. Then we can obtain the expectation value of any operator \hat{A} using the density operator:

$$\begin{aligned} \langle \hat{A} \rangle &= \sum_{n,m} c_n^* c_m \langle U_n | \hat{A} | U_m \rangle \\ &= \sum_{n,m} \rho_{mn} \langle U_n | \hat{A} | U_m \rangle \\ &= \sum_{n,m} \langle U_m | \hat{\rho} | U_n \rangle \langle U_n | \hat{A} | U_m \rangle \\ &= \sum_m \langle U_m | \hat{\rho} \hat{A} | U_m \rangle \\ \langle \hat{A} \rangle &= \text{Tr}(\hat{\rho} \hat{A}) \end{aligned} \quad (1.2.5)$$

where $\text{Tr}(O)$ stands for the trace of matrix O .

In this definition, the density operator is analogous to the wave function which only describes pure states. Once mixed states are involved, we thus want to include them in a more general definition of the density matrix.

• **Mixed states**

In a statistical ensemble representation, we cannot express the ensemble quantum state with a single state vector $|\Psi\rangle$ but rather with a probabilistic definition: The macroscopic system can be in the microstate $|\Psi_i\rangle$ with the probability p_i ($\sum_i p_i = 1$). We thus extend the definition of the density operator $\hat{\rho}_i$ of the related pure state $|\Psi_i\rangle$ to include a mixture of pure states in the generalized density matrix $\hat{\rho}$:

Density operator

$$\begin{aligned} \hat{\rho} &= \sum_i p_i |\Psi_i\rangle\langle\Psi_i| \\ &= \sum_i p_i \hat{\rho}_i \end{aligned} \tag{1.2.6}$$

Expectation value of any operator \hat{A} expressed in terms of $\hat{\rho}$ is then:

$$\begin{aligned} \langle\hat{A}\rangle &= \sum_i p_i \langle\Psi_i|\hat{A}|\Psi_i\rangle \\ &= \sum_i p_i \text{Tr}(\hat{\rho}_i\hat{A}) \end{aligned}$$

Therefore, the expectation value of \hat{A} can be extracted from the trace of the product of $\hat{\rho}\hat{A}$:

Operator expectation value

$$\langle\hat{A}\rangle = \text{Tr}(\hat{\rho}\hat{A}) \tag{1.2.7}$$

This property will be extensively used in the following, in particular, it will ease the derivations taking advantage of the trace properties.

• **Density matrix properties**

Looking at the density matrix element in the basis $\{|U_n\rangle\}$ of \mathcal{H} :

$$\hat{\rho}_{nm} = \langle U_n^{(i)}|\hat{\rho}|U_m^{(i)}\rangle \tag{1.2.8}$$

$$= \sum_i p_i c_n^{(i)*} c_m^{(i)} \tag{1.2.9}$$

We can distinguish the different components of $\hat{\rho}$:

First, the diagonal element ($n = m$), called the population, gives the probability of occupying state $|U_n\rangle$. Secondly, the off-diagonal elements ($n \neq m$) refers to the quantum correlation between the states $|U_n\rangle$ and $|U_m\rangle$. The latter elements have a time-dependent phase factor and are called coherences, these elements are therefore inexistent in the classical description.

Finally, from the definition of the density operator, one can obtain the following properties:

- The density operator is Hermitian: $\hat{\rho}^\dagger = \hat{\rho}$
- It is positive semi-definite: $\langle \xi | \hat{\rho} | \xi \rangle \geq 0 \quad \forall | \xi \rangle$
- It is normalized: $\text{Tr}(\hat{\rho}) = 1$

1.2.2 Time evolution

The time evolution of pure states, described by the Hamiltonian $\hat{H}(t)$, is defined by the time-dependent Schrödinger equation:

$$i\hbar \frac{\partial}{\partial t} |\Psi(t)\rangle = \hat{H}(t) |\Psi(t)\rangle \quad (1.2.10)$$

Where \hbar is the Planck constant

And we can express the system time evolution with the propagator operator $\hat{\mathcal{U}}(t, t_0)$ which evolves the pure state from t_0 to t :

$$|\Psi(t)\rangle = \hat{\mathcal{U}}(t, t_0) |\Psi(t_0)\rangle \quad (1.2.11)$$

This operator being solution of the following differential equation:

$$i\hbar \frac{\partial}{\partial t} \hat{\mathcal{U}}(t, t_0) = \hat{H}(t) \hat{\mathcal{U}}(t, t_0) \quad (1.2.12)$$

And formally defined as^a:

$$\hat{\mathcal{U}}(t, t_0) = e^{-\frac{i}{\hbar} \hat{H}(t, t_0)} \quad (1.2.13)$$

• Evolution of the density operator

In a similar way, we can derive analogous to the Schrödinger an equation which is for the density operator. Taking the time derivative of the density operator we obtain:

$$\begin{aligned} \frac{\partial}{\partial t} \hat{\rho}(t) &= \frac{\partial}{\partial t} \left(\sum_i p_i |\Psi_i(t)\rangle \langle \Psi_i(t)| \right) \\ &= \sum_i p_i \left(\frac{\partial}{\partial t} |\Psi_i(t)\rangle \langle \Psi_i(t)| + |\Psi_i(t)\rangle \frac{\partial}{\partial t} \langle \Psi_i(t)| \right) \\ &= \sum_i p_i \left(\frac{1}{i\hbar} \hat{H}(t) |\Psi_i(t)\rangle \langle \Psi_i(t)| + |\Psi_i(t)\rangle \frac{1}{-i\hbar} \langle \Psi_i(t)| \hat{H}(t) \right) \\ &= \frac{1}{i\hbar} \left(\hat{H}(t) \hat{\rho}(t) - \hat{\rho}(t) \hat{H}(t) \right) \end{aligned} \quad (1.2.14)$$

Leading to the Liouville-Von Neumann equation:

Liouville-Von Neumann equation:

$$\frac{\partial}{\partial t} \hat{\rho}(t) = \frac{1}{i\hbar} [\hat{H}(t), \hat{\rho}(t)] \quad (1.2.15)$$

where $[\hat{H}(t), \hat{\rho}(t)]$ is the commutation operation between $\hat{H}(t)$ and $\hat{\rho}(t)$

^ais \hat{O} if a generic operator, then $\exp(i\hat{O}) \equiv I + \sum_{n=1}^{\infty} \frac{i^n}{n!} \prod_{i=1}^n \hat{O} \dots \hat{O}_i$ Here we consider \hat{O} as an hermitian operator so that $\exp(i\hat{O})$ is unitary.

The solution of which gives:

$$\hat{\rho}(t) = \hat{\mathcal{U}}(t, t_0)\hat{\rho}(t_0)\hat{\mathcal{U}}^\dagger(t, t_0) \quad (1.2.16)$$

Introducing the Liouville superoperator $\hat{L}(t)$ defined as:

$$i\hat{L}(t) \cdot = \frac{1}{i\hbar} [\cdot, \hat{H}(t)] \quad (1.2.17)$$

We can now express equation 1.2.15 as:

$$\frac{\partial}{\partial t}\hat{\rho}(t) = -i\hat{L}(t)\hat{\rho}(t) \quad (1.2.18)$$

Isolated system: In the particular case of a time-independent hamiltonian, the following property of the propagator operator arises:

$$\begin{aligned} \hat{\mathcal{U}}(t, t_0) &= e^{-\frac{i}{\hbar}(t-t_0)\hat{H}} \\ &= \hat{\mathcal{U}}^\dagger(t_0, t) \end{aligned} \quad (1.2.19)$$

Therefore, in the case of an isolated system the Liouville superoperator is also time independent and the density operator can be expressed as:

$$\hat{\rho}(t) = e^{-\frac{i}{\hbar}(t-t_0)\hat{H}}\hat{\rho}(t_0)e^{\frac{i}{\hbar}(t-t_0)\hat{H}} \quad (1.2.20)$$

$$= e^{-i(t-t_0)\hat{L}}\hat{\rho}(t_0) \quad (1.2.21)$$

• Operator time evolution

Schrödinger picture:^b Following the density operator time evolution, we will now describe the time evolution of operators within the density operator frame. From equation 1.2.7 and 1.2.16 we derive the time evolution of the expectation value of the operator \hat{A} within the Schrödinger picture:

$$\langle A(t) \rangle = \text{Tr}(\hat{\rho}(t)\hat{A}) \quad (1.2.22)$$

$$= \text{Tr}(\hat{\mathcal{U}}(t, t_0)\hat{\rho}(t_0)\hat{\mathcal{U}}^\dagger(t, t_0)\hat{A}) \quad (1.2.23)$$

Heisenberg picture: Within the Heisenberg picture, the pure states and thus the density operator are time independent.

Therefore we have:

$$|\Psi\rangle_H = |\Psi(t_0)\rangle \quad (1.2.24)$$

$$\hat{\rho}_H = \hat{\rho} \quad (1.2.25)$$

The time dependency resides however in the operator definition:

$$\hat{A}_H(t) = \hat{\mathcal{U}}^\dagger(t, t_0)\hat{A}(t)\hat{\mathcal{U}}(t, t_0) \quad (1.2.26)$$

Ensuring both representations to be equivalent:

$${}_H\langle\Psi|\hat{A}_H(t)|\Psi\rangle_H = \langle\Psi(t)|\hat{A}|\Psi(t)\rangle \quad (1.2.27)$$

^bWithout specific notation, state vectors or operators are defined within the Schrödinger picture ($|\Psi(t)\rangle \equiv |\Psi_S(t)\rangle$ and $\hat{A} \equiv \hat{A}_S$).

Taking advantage of the cyclic invariance of the trace allows to verify also the equivalence of the expectation value of the operator \hat{A} in both pictures:

$$\begin{aligned}\langle \hat{A}_H(t) \rangle &= \text{Tr}(\hat{\rho}_H(t) \hat{A}_H(t)) \\ &= \text{Tr}(\hat{\rho}_H(t_0) \hat{\mathcal{U}}^\dagger(t, t_0) \hat{A}(t) \hat{\mathcal{U}}(t, t_0)) \\ &= \text{Tr}(\hat{\mathcal{U}}(t, t_0) \hat{\rho}_H(t_0) \hat{\mathcal{U}}^\dagger(t, t_0) \hat{A}(t)) \\ \langle \hat{A}_H(t) \rangle &= \langle \hat{A}(t) \rangle\end{aligned}\tag{1.2.28}$$

Definition 1.2.26 leads to the time derivative of the operator $\hat{A}_H(t)$:

$$\frac{d}{dt} \hat{A}_H(t) = \frac{1}{i\hbar} [\hat{A}_H(t), \hat{H}] + \left(\frac{\partial}{\partial t} \hat{A}_H(t) \right)\tag{1.2.29}$$

If $\hat{A}_H(t)$ does not explicitly depend on the time and following the definition of the Liouville superoperator we find:

$$\frac{d}{dt} \hat{A}_H(t) = i\hat{L}_H(t) \hat{A}_H(t)\tag{1.2.30}$$

Isolated system

Finally, for time independent Hamiltonian and Liouville operators, the solution of the latter equation is:

$$\hat{A}_H(t) = e^{-i(t-t_0)\hat{L}_H} \hat{A}_H(t_0)\tag{1.2.31}$$

$$\hat{A}_H(t) = e^{i(t-t_0)\frac{\hat{H}}{\hbar}} \hat{A}_H(t_0) e^{-i(t-t_0)\frac{\hat{H}}{\hbar}}\tag{1.2.32}$$

• Dirac interaction picture

We now describe the case of the time-independent Hamiltonian \hat{H}_0 under the influence of perturbation $\hat{W}(t)$:

$$\hat{H}(t) = \hat{H}_0 + \hat{W}(t)\tag{1.2.33}$$

As we will see, a convenient way to describe such a case is to go beyond the Schrödinger and Heisenberg pictures, toward the Dirac, or so-called interaction picture. In this representation, the time dependence resides both in the state vectors and the operators.

Let us first define the propagator operators related to the time-independent Hamiltonian \hat{H}_0 and the total Hamiltonian \hat{H} :

$$\hat{\mathcal{U}}(t, t_0) = e^{\frac{-i}{\hbar} \hat{H}(t-t_0)}\tag{1.2.34}$$

$$\hat{\mathcal{U}}_0(t, t_0) = e^{\frac{-i}{\hbar} \hat{H}_0(t-t_0)}\tag{1.2.35}$$

We can now introduce the state vectors $|\Psi_I(t)\rangle$ and operators $\hat{A}_I(t)$ in the Dirac picture:

$$|\Psi_I(t)\rangle = \hat{\mathcal{U}}_0^\dagger(t, t_0) |\Psi(t)\rangle\tag{1.2.36}$$

$$\hat{A}_I(t) = \hat{\mathcal{U}}_0^\dagger(t, t_0) \hat{A}(t) \hat{\mathcal{U}}_0(t, t_0)\tag{1.2.37}$$

In this way, one can easily check that the Dirac representation is equivalent to both Schrödinger and Heisenberg pictures:

$$\langle \Psi_I(t) | \hat{A}_I(t) | \Psi_I(t) \rangle =_H \langle \Psi | \hat{A}_H(t) | \Psi \rangle_H = \langle \Psi(t) | \hat{A} | \Psi(t) \rangle \quad (1.2.38)$$

Finally, the state vector in this representation evolves as:

$$i\hbar \frac{d}{dt} | \Psi_I(t) \rangle = \hat{W}_I(t) | \Psi_I(t) \rangle \quad (1.2.39)$$

Where only the perturbative term of the total hamiltonian acts. We then obtain the density matrix and operators time evolution to be governed by the following differential equations:

$$\frac{\partial}{\partial t} \hat{\rho}_I(t) = \frac{1}{i\hbar} [\hat{W}_I(t), \hat{\rho}_I(t)] \quad (1.2.40)$$

$$\frac{d}{dt} \hat{A}_I(t) = \frac{1}{i\hbar} [\hat{A}_I(t), \hat{H}_0] + \left(\frac{\partial}{\partial t} \hat{A}_I(t) \right) \quad (1.2.41)$$

Therefore the density operator time evolution is also only subjected to the perturbative hamiltonian $\hat{W}_I(t)$, and the unperturbed term reside in the evolution of the operator $\hat{A}_I(t)$. Doing so, the interaction picture allows to remove the time dependency of the unperturbed Hamiltonian \hat{H}_0 , which is transferred to the operators, focusing on the perturbation which causes the states(density operator) to evolve. The Dirac representation is therefore convenient to treat the perturbations.

1.2.3 Thermal equilibrium

In the following, and for all investigations we made during this work, we treat quantum systems in the canonical ensemble, at thermal equilibrium. Therefore, the statistical probabilities introduced in the density operator will be expressed in term of the Boltzmann factor:

$$p_i \propto e^{-\beta E_i} \quad (1.2.42)$$

where $\beta = \frac{1}{k_b T}$ is the inverse temperature, and k_b is the Boltzmann constant.

Including this probability in the definition of the density operator, and normalizing the latter with the partition function \mathcal{Z} leads to the canonical definition:

Canonical density operator

$$\hat{\rho}_{eq} = \frac{1}{\mathcal{Z}} \sum_i e^{-\beta E_i} | \Psi_i \rangle \langle \Psi_i | = \frac{e^{-\beta \hat{H}}}{\mathcal{Z}} \quad (1.2.43)$$

Where the partition function reads:

$$\mathcal{Z} = \text{Tr} \left(e^{-\beta \hat{H}} \right) \quad (1.2.44)$$

For the sake of clarity in the following sections, we define the diagonal elements of the canonical density operator as:

$$\Pi_n = \langle U_n | \hat{\rho}_{eq} | U_n \rangle \quad (1.2.45)$$

$$= \frac{e^{-\beta E_n}}{\mathcal{Z}} \quad (1.2.46)$$

From equations 1.2.7 and 1.2.43, it naturally follows that the expectation value of the operator \hat{A} is defined as:

$$\langle \hat{A} \rangle = \text{Tr}(\hat{\rho}_{eq} \hat{A}) \quad (1.2.47)$$

$$= \frac{1}{\mathcal{Z}} \text{Tr}(e^{-\beta \hat{H}} \hat{A}) \quad (1.2.48)$$

From this definition, one can recover the definition of the thermodynamic quantities of the canonical ensemble.

In particular, the energy can be derived as:

$$E = \langle \hat{H} \rangle = \frac{1}{\mathcal{Z}} \text{Tr}(e^{-\beta \hat{H}} \hat{H}) \quad (1.2.49)$$

$$= -\frac{\partial}{\partial \beta} \ln(\text{Tr}(e^{-\beta \hat{H}})) \quad (1.2.50)$$

$$= -\frac{\partial}{\partial \beta} \ln \mathcal{Z} \quad (1.2.51)$$

While the entropy is:

$$S = -\langle k_b \ln(\hat{\rho}_{eq}) \rangle \quad (1.2.52)$$

$$= -k_b \text{Tr}(\hat{\rho}_{eq} \ln \hat{\rho}_{eq}) \quad (1.2.53)$$

And the Helmholtz free energy:

$$F = -\frac{1}{\beta} \ln \mathcal{Z} \quad (1.2.54)$$

1.3 Linear Response theory

The linear response theory describes the response of a physical system to a perturbation, which slightly drives it away from equilibrium. In particular, it relates the properties of response, susceptibility, and relaxation of the unperturbed system in terms of the equilibrium correlation function. This development has been originally formalized by R. Kubo¹¹ in 1966.

Let us begin by considering a system at thermal equilibrium described by the time-independent Hamiltonian \hat{H}_0 , therefore described by the canonical density operator $\hat{\rho}_{eq}$ as defined in equation 1.2.43. At time t_0 the system is slightly shifted from equilibrium due to a perturbation described by the additional hamiltonian term $\hat{W}(t)$:

$$\hat{W}(t) = -f(t)\hat{A} \quad (1.3.1)$$

Where \hat{A} is an hermitian operator (observable) of the system associated with the generalized force $f(t)$ which is supposed to be “small”, compared to the eigenvalues of the unperturbed system. While $t_0 \rightarrow -\infty$ we assume the system to be at thermal equilibrium. The perturbed system is then described by the perturbed hamiltonian \hat{H} :

$$\hat{H} = \hat{H}_0 + \hat{W}(t) \quad (1.3.2)$$

As already discussed in Section 1.2 a convenient way to treat the perturbation is to describe the system within the interaction picture, for which we recall the principal definitions in the following. We associate two quantum propagator $\hat{\mathcal{U}}(t, t_0)$ and $\hat{\mathcal{U}}_0(t, t_0)$ with the perturbed hamiltonian \hat{H} and the time independent (at equilibrium) one \hat{H}_0 :

$$\hat{\mathcal{U}}(t, t_0) = e^{-\frac{i}{\hbar}\hat{H}(t-t_0)} \quad \hat{\mathcal{U}}_0(t, t_0) = e^{-\frac{i}{\hbar}\hat{H}_0(t-t_0)} \quad (1.3.3)$$

The equilibrium term being separated, we can now express the state vector $|\Psi_I(t)\rangle$ and any operator $\hat{A}_I(t)$ in the interaction picture:

$$|\Psi_I(t)\rangle = \hat{\mathcal{U}}_0^\dagger(t, t_0) |\Psi(t)\rangle \quad (1.3.4)$$

$$\hat{A}_I(t) = \hat{\mathcal{U}}_0^\dagger(t, t_0) \hat{A}(t_0) \hat{\mathcal{U}}_0(t, t_0) \quad (1.3.5)$$

$$\Rightarrow \hat{W}_I(t) = \hat{\mathcal{U}}_0^\dagger(t, t_0) \hat{W}(t) \hat{\mathcal{U}}_0(t, t_0) \quad (1.3.6)$$

Finally the Liouville-Von Neuman theorem (equation 1.2.15) leads to:

$$\frac{d}{dt} \hat{\rho}_I(t) = \frac{1}{i\hbar} [\hat{W}_I(t), \hat{\rho}_I(t)] \quad (1.3.7)$$

As we have seen in Section 1.2, the density operator allows us to compute the expected value of any operator. One might derive the latter by integrating the Liouville-von Neuman equation in the Dirac representation:

$$\hat{\rho}_I(t) = \hat{\rho}_I(t_0) + \frac{i}{\hbar} \int_{t_0}^t f(t') [\hat{A}_I(t'), \hat{\rho}_I(t')] dt' \quad (1.3.8)$$

As the system is initially at thermal equilibrium ($\hat{\rho}_I(t_0) = \hat{\rho}_{eq}$) and making t_0 tend to $-\infty$ we obtain:

$$\hat{\rho}_I(t) = \hat{\rho}_{eq} + \frac{i}{\hbar} \int_{-\infty}^t f(t') [\hat{A}_I(t'), \hat{\rho}_I(t')] dt' \quad (1.3.9)$$

Recursively, one can now introduce the definition of $\hat{\rho}_I(t)$ into itself and end up with a perturbation expansion in terms of the density matrix to be truncated at the first order as we describe a linear relation in terms of $f(t)$. For the latter reason and in an equivalent ending, one also replaces $\hat{\rho}_I(t')$ with $\hat{\rho}_{eq}$ in the commutator, hence:

$$\hat{\rho}_I(t) = \hat{\rho}_{eq} + \frac{i}{\hbar} \int_{-\infty}^t f(t') [\hat{A}_I(t'), \hat{\rho}_{eq}] dt' + O(f^2) \quad (1.3.10)$$

1.3.1 Response function

We now want to describe the response of any arbitrary observable \hat{B} of the system to the perturbation associated with the operator \hat{A} . Having computed the density operator in the interaction picture and using definition 1.2.7, we can derive the expectation value of the observable \hat{B} out of equilibrium:

$$\langle \hat{B}_I(t) \rangle_{n.eq.} = \text{Tr}(\hat{B}_I(t) \hat{\rho}_I(t)) \quad (1.3.11)$$

$$= \langle \hat{B}(t) \rangle_{eq} + \frac{i}{\hbar} \int_{-\infty}^t f(t') \text{Tr}(\hat{B}_I(t) [\hat{A}_I(t'), \hat{\rho}_{eq}]) dt' \quad (1.3.12)$$

$$= \langle \hat{B}(t) \rangle_{eq} + \frac{i}{\hbar} \int_{-\infty}^t f(t') \text{Tr}(\hat{\rho}_{eq} [\hat{B}_I(t), \hat{A}_I(t')]) dt' \quad (1.3.13)$$

$$= \langle \hat{B}(t) \rangle_{eq} + \frac{i}{\hbar} \int_{-\infty}^t f(t') \langle [\hat{B}_I(t), \hat{A}_I(t')] \rangle_{eq} dt' \quad (1.3.14)$$

where we use the invariance of the trace under cyclic permutation. Taking advantage of the latter property once again and using the commutation relation between $\hat{\rho}_{eq}$ and \hat{H}_0 , we finally obtain:

$$\langle \hat{B}_I(t) \rangle_{n.eq.} = \langle \hat{B}(t) \rangle_{eq} + \frac{i}{\hbar} \int_{-\infty}^t f(t') \langle [\hat{B}_I(t-t'), \hat{A}_I] \rangle_{eq} dt' \quad (1.3.15)$$

$$= \langle \hat{B}(t) \rangle_{eq} + \frac{i}{\hbar} \int_{-\infty}^{+\infty} f(t') \langle [\hat{B}_I(t-t'), \hat{A}_I] \rangle_{eq} \theta(t-t') dt' \quad (1.3.16)$$

$$= \langle \hat{B}(t) \rangle_{eq} + \int_{-\infty}^{+\infty} \chi_{BA}(t-t') f(t') dt' \quad (1.3.17)$$

In the last line we defined the linear response function, also known as susceptibility, $\chi_{BA}(\tau)$ through the Kubo formula:

Kubo's formula

$$\chi_{BA}(\tau) = \frac{i}{\hbar} \langle [\hat{B}_I(\tau), \hat{A}] \rangle_{eq} \theta(\tau) \quad (1.3.18)$$

where θ is the Heaviside function.

So defined, the linear response function describes the relation between the perturbation related to the time correlation function between operators \hat{A} and \hat{B} at equilibrium. As the perturbation could only modify the system after it has been switched on, the linear response function should vanish for $t < t'$. In order to respect the causality relation we introduced the Heaviside function $\theta(\tau)$ and extended the upper integration boundary.

Using the formalism defined in equations 1.2.46 we can also reformulate equation 1.3.18 on the

eigenstates basis $\{|U_n\rangle\}$ as:

$$\chi(\tau) = \frac{i}{\hbar} \theta(\tau) \sum_{n,m} (\Pi_n - \Pi_m) B_{nm} A_{mn} e^{-i\omega_{mn}\tau} \quad (1.3.19)$$

where we introduced the Bohr frequency $\omega_{mn} = \frac{E_m - E_n}{\hbar}$, the matrix elements B_{nm} and A_{nm} are defined as $X_{nm} = \langle U_n | \hat{X} | U_m \rangle$ ($\hat{X} = \hat{A}, \hat{B}$) and Π_n as defined in equation 1.2.46.

1.3.2 Generalized susceptibility

We can then define the generalized susceptibility, as being the Fourier transform of the linear response function in the frequency space:

$$\tilde{\chi}_{BA}(\omega) = \lim_{\epsilon \rightarrow 0^+} \int_{-\infty}^{+\infty} \chi_{BA}(\tau) e^{i\omega\tau} e^{-\epsilon\tau} d\tau \quad (1.3.20)$$

where we introduced the last exponential term $e^{-\epsilon\tau}$ in the limit of $\epsilon \rightarrow 0^+$ to ensure that the latter expression does not diverge for $\tau \rightarrow +\infty$.

Taking the inverse Fourier transform we naturally have:

$$\chi_{BA}(\tau) = \frac{1}{2\pi} \int_{-\infty}^{+\infty} \tilde{\chi}_{BA}(\omega) e^{-i\omega\tau} d\omega \quad (1.3.21)$$

Finally, through equation 1.3.19 we can also express the generalized susceptibility in the basis of the eigenstates $\{|U_n\rangle\}$:

$$\tilde{\chi}_{BA}(\omega) = \frac{i}{\hbar} \sum_{n,m} (\Pi_n - \Pi_m) B_{nm} A_{mn} \lim_{\epsilon \rightarrow 0^+} \frac{1}{\omega_{mn} - \omega - i\epsilon} \quad (1.3.22)$$

As a time convolution product of the linear response function χ_{BA} and f , the expectation value $\langle \hat{B}_I(t) \rangle_{n.eq.}$ can therefore be computed by the product of the generalized susceptibility and the Fourier transform of $f(t)$. The generalized susceptibility can be recast in a complex function of a real frequency of the form:

$$\tilde{\chi}_{BA}(\omega) = \chi'_{BA}(\omega) + i\chi''_{BA}(\omega) \quad (1.3.23)$$

And one can derive that:

$$\chi'_{BA}(\omega) = \int \frac{1}{2} [\chi_{BA}(\tau) + \chi_{BA}(-\tau)] e^{i\omega\tau} d\tau \quad (1.3.24)$$

$$\chi''_{BA}(\omega) = \int \frac{1}{2} [\chi_{BA}(\tau) - \chi_{BA}(-\tau)] e^{i\omega\tau} d\tau \quad (1.3.25)$$

In the case $A = B$, the imaginary part $\chi''_{BA}(\omega)$ is therefore governed by the non-invariant (under time reversal) term of the generalized susceptibility. Thus it is related to dissipation process. The real and imaginary parts of the complex generalized susceptibility are linked by the Kramers-Kronig relations, which allow one to reconstruct the entire susceptibility from either the imaginary or real part.

In the following, we will define a set of correlation functions referring to the fluctuation, the dissipation, and relaxation. We will also systematically provide the definitions in the basis of the energy eigenstates $|U_n\rangle$ which will ease the derivation of the relation between them.

1.3.3 Fluctuations

In this definition, the general correlation between fluctuating quantities as well as the symmetric correlation function for which relation with the susceptibility will be given. The general definition of time correlation function between two observables \hat{A} and \hat{B} is defined as follows:

$$C_{BA}(\tau) = \langle \hat{B}_I(\tau) \hat{A} \rangle_{eq} \quad (1.3.26)$$

Which can be recast using equation 1.3.19 as:

$$C_{BA}(\tau) = \sum_{n,m} \Pi_n B_{nm} A_{mn} e^{-i\omega_{mn}\tau} \quad (1.3.27)$$

One can notice that even in the case of hermitian operators (related to observables) \hat{A} and \hat{B} the latter correlation function is in general complex. Therefore, in order to represent observable fluctuations of a quantum system, we define the following symmetric correlation function S_{BA} :

Symmetric correlation function

$$S_{BA}(\tau) = \frac{1}{2} \langle \{ \hat{B}_I(\tau), \hat{A} \} \rangle_{eq} \quad (1.3.28)$$

$$= \frac{1}{2} (C_{BA}(\tau) + C_{AB}(-\tau)) \quad (1.3.29)$$

In case of Hermitian operators, \hat{A} and \hat{B} the symmetric correlation is real as suggested by the expression of $C_{AB}(-\tau)$:

$$C_{AB}(-\tau) = C_{BA}(-\tau) \quad (1.3.30)$$

$$= C_{BA}^*(\tau) \quad (1.3.31)$$

In addition, considering $\hat{B} = \hat{A}$ at $\tau = 0$ we obtain:

$$C_{AA}(\tau) = S_{AA}(\tau) \quad (1.3.32)$$

$$= \langle \hat{A}^2 \rangle_{eq} \quad (1.3.33)$$

Then if \hat{A} is centered, both C_{AA} and S_{AA} correspond to the variance of the latter observable. Thus, in these conditions they relate to the fluctuations of the system.

Through Fourier transform, one can obtain the symmetric correlation function in the frequency domain:

$$\tilde{S}_{BA}(\omega) = \int_{-\infty}^{+\infty} S_{BA}(\tau) e^{-i\omega\tau} d\tau \quad (1.3.34)$$

In order to express the latter definition in the basis of the energy eigenstates we will use expression 1.3.29 as well as the following relation:

$$C_{AB}(-\tau) = \sum_{n,m} \Pi_n A_{nm} B_{mn} e^{i\omega_{mn}\tau} \quad (1.3.35)$$

$$= \sum_{n,m} \Pi_n A_{nm} B_{mn} e^{-i\omega_{nm}\tau} \quad (1.3.36)$$

$$= \sum_{n,m} \Pi_n A_{mn} B_{nm} e^{-i\omega_{mn}\tau} \quad (1.3.37)$$

Thus, we find:

$$S_{BA}(\tau) = \frac{1}{2} \left[\sum_{n,m} (\Pi_n + \Pi_m) B_{nm} A_{mn} e^{-i\omega_{mn}\tau} \right] \quad (1.3.38)$$

Hence:

$$\tilde{S}_{BA}(\omega) = \pi \sum_{n,m} (\Pi_n + \Pi_m) B_{nm} A_{mn} \delta(\omega - \omega_{mn}) \quad (1.3.39)$$

1.3.4 Relaxation

The following correlation function is also real-valued and was introduced by Kubo:

Kubo's canonical correlation function

$$K_{BA}(\tau) = \frac{1}{\beta} \int_0^\beta \left\langle e^{\lambda \hat{H}_0} \hat{A} e^{-\lambda \hat{H}_0} \hat{B}_I(\tau) \right\rangle_{eq} d\lambda \quad (1.3.40)$$

$$= \frac{1}{\beta} \int_0^\beta \left\langle \hat{A}_I(-i\hbar\lambda) \hat{B}_I(\tau) \right\rangle_{eq} d\lambda \quad (1.3.41)$$

The latter correlation function describes the relaxation of the system,¹² which is initially driven out of equilibrium. One can obtain:

$$K_{BA}(\tau) = \frac{1}{\beta\hbar} \sum_{n,m} (\Pi_n - \Pi_m) \frac{B_{nm} A_{mn}}{\omega_{mn}} e^{i\omega_{mn}\tau} \quad (1.3.42)$$

Leading to the definition of the canonical correlation function in the frequency domain:

$$\tilde{K}_{BA}(\omega) = \int_{-\infty}^{+\infty} K_{BA}(\tau) e^{i\omega\tau} d\tau \quad (1.3.43)$$

$$= 2\pi \sum_{n,m} \frac{\Pi_n - \Pi_m}{\beta\hbar\omega_{mn}} B_{nm} A_{mn} \delta(\omega - \omega_{mn}) \quad (1.3.44)$$

1.3.5 Dissipation

We now define the spectral density as the expectation value of the commutator of operators $\hat{B}_I(\tau)$ and \hat{A} :

$$\xi_{BA}(\tau) = \frac{1}{2\hbar} \left\langle [\hat{B}_I(\tau), \hat{A}] \right\rangle_{eq} \quad (1.3.45)$$

In analogy with the derivation of the symmetric correlation function, one can find that:

$$\xi_{BA}(\tau) = \frac{1}{2\hbar} (C_{BA}(\tau) - C_{AB}(-\tau)) \quad (1.3.46)$$

Leading to the spectral density $\tilde{\xi}_{BA}(\omega)$:

$$\tilde{\xi}_{BA}(\omega) = \frac{\pi}{\hbar} \sum_{n,m} (\Pi_n - \Pi_m) B_{nm} A_{mn} \delta(\omega - \omega_{mn}) \quad (1.3.47)$$

Which, in the case of hermitian operators, leads to the following property:

$$\tilde{\xi}_{BA}^*(\omega) = \tilde{\xi}_{AB}(\omega) \quad (1.3.48)$$

In addition, in the case $\hat{B} = \hat{A}^\dagger$ one can obtain that:

$$\tilde{\xi}_{\hat{A}^\dagger \hat{A}}(\omega) = \text{Im} \{ \tilde{\chi}_{\hat{A}^\dagger \hat{A}}(\omega) \} = \tilde{\chi}_{\hat{A}^\dagger \hat{A}}''(\omega) \quad (1.3.49)$$

The latter quantity therefore describes the dissipation.

1.3.6 Fluctuation-Dissipation theorem

Thanks to the derivation of the different correlations functions as well as the spectral density, we can then establish several important relationships between fluctuation, dissipation, and relaxation.

• Correlation-Susceptibility

We first describe the relationship between the correlation functions and the generalized susceptibility. In the time domain, the linear response function is linked to the spectral density as:

$$\chi_{BA}(\tau) = 2i\theta(\tau)\zeta_{BA}(\tau) \quad (1.3.50)$$

While it is related to the Kubo canonical correlation function as:

$$\chi_{BA}(\tau) = \beta\theta(\tau)K_{BA\dot{A}}(\tau) \quad (1.3.51)$$

$$\tilde{\chi}_{BA}(\omega) = \beta \int_0^{+\infty} K_{BA\dot{A}}(\tau)e^{i\omega\tau} d\tau \quad (1.3.52)$$

• Correlation-Spectral density

We now focus on the relations between correlation function and spectral density. In the frequency domain, the antisymmetric correlation function is linked to the dissipation, represented by the spectral density as:

$$\tilde{C}_{BA}(\omega) = \frac{2\hbar}{1 - e^{-\beta\hbar\omega}} \tilde{\xi}_{BA}(\omega) \quad (1.3.53)$$

• Kubo correlation-Spectral density

To describe the relation between the dissipation and the relaxation, we take advantage of the canonical correlation function:

$$\tilde{K}_{BA}(\omega) = \frac{2}{\beta} \frac{\tilde{\xi}_{BA}(\omega)}{\omega} \quad (1.3.54)$$

Finally, the following relation, derived by H. Callen et T. Welton in 1951,¹³ known as the FDT, describes the link between the symmetric correlation function $\tilde{S}_{BA}(\omega)$ and the spectral density $\tilde{\xi}_{BA}(\omega)$:

Quantum Fluctuation-Dissipation theorem

$$\tilde{S}_{BA}(\omega) = \hbar \coth\left(\frac{\beta\hbar\omega}{2}\right) \tilde{\xi}_{BA}(\omega) \quad (1.3.55)$$

It therefore links the fluctuations described by $\tilde{S}_{BA}(\omega)$ to the dissipation described by $\tilde{\xi}_{BA}(\omega)$. From the latter theorem, we can derive the fluctuation-dissipation relation in the classical picture as:

$$\lim_{\hbar \rightarrow 0} \hbar \coth\left(\frac{\beta\hbar\omega}{2}\right) = \frac{2k_bT}{\omega} \quad (1.3.56)$$

For which we find:

Classical Fluctuation-Dissipation theorem

$$\tilde{S}_{BA}(\omega) = \frac{2k_b T}{\omega} \tilde{\xi}_{BA}(\omega) \quad (1.3.57)$$

1.4 Ab-Initio Molecular Dynamics

In this section, we will describe the ab-initio scheme used in the simulations presented in this thesis. First, we will recall the Born-Oppenheimer approximation allowing the decoupling of the nuclear and electron wavefunction and then describe the treatment of the electronic part via the DFT. In the next section, we will then see how to describe the nuclear counterpart.

1.4.1 The Born-Oppenheimer approximation

We consider the following many body hamiltonians of the N nuclei and n electron system:

$$\hat{H} = \hat{T}_n + \hat{T}_e + \hat{V}_{NN} + \hat{V}_{ee} + \hat{V}_{eN} \quad (1.4.1)$$

Where we introduced:

The nuclear kinetic operator:

$$\hat{T}_N = -\frac{\hbar}{2} \sum_{a=1}^N \frac{1}{M_a} \nabla_a^2$$

The electron-nuclear Coulomb attraction:

$$\hat{V}_{eN} = - \sum_{a=1}^N \sum_{i=1}^n \frac{Z_a e^2}{|r_i - R_a|}$$

The electron-electron Coulomb repulsion:

$$\hat{V}_{ee} = \sum_{i=1}^n \sum_{j=1}^n \frac{e^2}{|r_i - r_j|}$$

The electronic kinetic operator:

$$\hat{T}_e = -\frac{\hbar}{2m_e} \sum_{i=1}^n \nabla_i^2$$

The nuclear-nuclear Coulomb repulsion:

$$\hat{V}_{NN} = \sum_{a=1}^N \sum_{b=1}^N \frac{Z_a Z_b e^2}{|R_a - R_b|}$$

Unfortunately, the related Schrödinger equation cannot be solved analytically for complex systems. To address this issue, we have to use the Born-Oppenheimer approximation, which allows decoupling the electronic and nuclear degrees of freedom. The underlying idea behind the Born-Oppenheimer approximation is that the nuclei being much heavier than electrons, they are assumed to be stationary as compared to the electrons. This allows to write the wavefunction in terms of nuclear $\chi(R)$ and electronic $\Psi(r; R)$ wavefunctions:

$$\phi(r; R) = \Psi(r; R) \chi(R) \quad (1.4.2)$$

In this context, the electrons are assumed to follow the nuclei adiabatically, and can be described considering an electronic hamiltonian $\hat{H}_e(R)$ which depends on the nuclei position R parametrically.

$$\hat{H}_e = \hat{T}_e + \hat{V}_{ee} + \hat{V}_{eN} + \hat{V}_{NN} \quad (1.4.3)$$

In the latter expression, the nuclear positions are assumed to be fixed, due to their infinite mass. Therefore, the nuclear positions can be considered as parameters which will only shift the related energy. Then at each fixed configuration R the electronic wavefunction $\Psi(r; R)$ is then the eigen vector of the electronic hamiltonian \hat{H}_e with eigenvalue $E_e(R)$:

$$\hat{H}_e |\Psi_e(r; R)\rangle = E_e(R) |\Psi_e(r; R)\rangle \quad (1.4.4)$$

The latter time-independent Schrödinger equation, allows one to describe the electronic part only without having to describe the nuclear part. This remarkable property is extensively used in

several ab-initio approaches. In particular, DFT describes the quantum electronic structure while nuclei are treated with classical Newtonian mechanics. The aim of the present work is exactly to go beyond this partly quantum description, however in the adiabatic approximation. Finally, once the electronic wavefunction is solved, we obtain an effective potential energy surface for the nuclei defined by $E_e(R)$:

$$\hat{H}_N = \hat{T}_N + E_e(R) \tag{1.4.5}$$

Which is therefore described by:

$$\hat{H}_N |\chi(r; R)\rangle = \left[-\frac{\hbar}{2} \sum_{a=1}^N \frac{1}{M_a} \nabla_a^2 + E_e(R) \right] |\chi(r; R)\rangle \tag{1.4.6}$$

The interactions between atoms can be computed at different levels of precision: one way is to use interatomic potentials, which express the interactions as depending on the nuclear positions \vec{R}_I in an analytical form. An example is provided by Lennard-Jones potentials. However, most of them cannot reproduce the bond breaking-reforming nor be applied for (P, T) conditions they were not suited for an exception is provided by the so-called reactive force fields. In this case, we must describe the bonding with direct reference to electronic structure. One current reference method is the DFT resulting from the work of P. Hohenberg, L.J. Sham and W. Kohn^{14,15} who received the Nobel prize for the latter.

1.4.2 The Density Functional Theory

As we have seen, the Born-Oppenheimer approximation allows us to treat the electronic and nuclear wavefunctions separately. However, the quantum wavefunction associated with a large number of electrons is both an extraordinary complex quantity and might not be the most useful one: the electron density $n(r)$ is sufficient to describe all properties of the electronic ground state, such as the energy and the bonding. Indeed, the electronic density:

$$n(r) = n \int dr_2 \dots dr_n |\Psi_0(r, \dots, r_n)|^2 \quad (1.4.7)$$

Reduces the number of degrees of freedom to deal with from $3n$ to only 3. In 1964,¹⁵ this motivates P. Hohenberg and W. Kohn to formalize the onset of the DFT.

• Hohenberg and Kohn theorem

Hohenberg and Kohn

For the non-degenerate ground state, it exists a one to one correspondence between the Hamiltonian and the ground state electron density, which determines all the properties of the system. The energy as a functional of the electron density:

$$E[n] = T[n] + E_H[n] + E_{xc}[n] + V_{ext}[n] \quad (1.4.8)$$

is minimal when the density is the actual ground state density:

$$\min(E[n]) = E[n_0] \quad (1.4.9)$$

for which $E[n_0]$ is the ground state energy.

In the latter theorems, we defined four components of the total functional of density:

- The kinetic energy functional $T[n]$
- The Hartree functional $E_H[n]$
- The exchange and correlation functional $E_{xc}[n]$ which describes the electronic exchange and correlation contributions
- The external potential energy V_{ext}

The problem of finding the ground-state electron density is recast into a minimization problem of the energy functional $E[n]$ at constant number of electrons ($N = \int d^3r n(\vec{r})$).

$$\frac{\delta}{\delta n(\vec{r})} \left[E[n] - \mu \int d^3r n(\vec{r}) \right] = 0 \quad (1.4.10)$$

Where μ is the Lagrange multiplier that is associated with the conservation of the number of electrons and can be shown to be equal to the Fermi energy.

• Kohn-Sham equations

In 1965, W. Kohn and L.J. Sham introduced the following idea: for a given system of interacting electrons, one could find a virtual system of non-interacting electrons which has the same energy density of the system of interacting electrons. The density is therefore expanded on a basis of one-particle orbitals:

$$n(\vec{r}) = \sum_{i=1}^N |\psi_i(\vec{r})|^2 \quad (1.4.11)$$

For which the energy functional is therefore recast as:

$$E[n] = T_{KS}[n] + V_{KS}^{eff} \quad (1.4.12)$$

Where V_{KS}^{eff} is the effective potential of the one-particle orbitals.

This represents the next step of the development of the DFT introduced by Kohn and Sham in 1965. By minimizing the energy with respect to the $\{\psi_i(\vec{r})\}$ we obtain the Kohn-Sham equations:

Kohn-Sham equations

$$n(r) = \sum_i^N |\psi(r)|^2 \quad (1.4.13)$$

The ground-state electron density is found by solving:

$$\left[\frac{-\hbar^2 \nabla^2}{2m} + V_{KS}^{eff}(r) \right] \psi_i(r) = \epsilon_i \phi_i(r) \quad (1.4.14)$$

$$V_{KS}^{eff}(r) = V_{ext}(r) + e^2 \int dr' \frac{n(r')}{|r - r'|} + V_{xc}(r) \quad (1.4.15)$$

With $V_{xc}(r) = \frac{\delta E_{xc}}{\delta n(r)}$ the exchange correlation potential.

The two last terms on the right-hand side of equation (1.4.15) depend on the density. Therefore, starting from a given trial density $n^t(r)$, we obtain a new potential $V_s^t(r)$. Then solving (1.4.15), we obtain the orbitals $\{\psi_i(\vec{r})\}$ that are reinjected in equation (1.4.13) to provide a new density. These equations thus have a self-consistent loop:

$$n^t(r) \rightarrow V_s^t(r) \rightarrow \psi_i^t \rightarrow n^{t+1}(r) \rightarrow \dots$$

Finally, for each set of atomic position, we can calculate inter-atomic forces $f_i(t)$ that will be used for dynamics simulations.

DFT requires several parameters to be set properly. Indeed, in order to describe correctly a system, one should first pay attention to which exchange-correlation functional to use depending on the system under study.

• Functionals

One can distinguish two main approximations concerning the exchange-correlation energy functional.

Local Density Approximation

The Local Density Approximation (LDA) is based on the Homogeneous Electron Gas (HEG) model. It considers that the electron density of the system can be seen as locally homogeneous despite the fact that globally it is not. Since the exchange energy of HEG is known and that its correlation energy can be calculated from quantum Monte-Carlo calculation or perturbation theory, the exchange-correlation energy of HEG can thus be derived (Equation (1.4.16)).

$$E_{xc}^{HEG}(\bar{n}) = V\bar{n}e_{xc}^{HEG}(\bar{n}) \quad (1.4.16)$$

With V the volume of the system, \bar{n} the mean value of electron density, and e_{xc}^{HEG} the exchange-correlation energy per electron for the HEG model.

Based on this model, the local density approximation takes advantage of this known HEG exchange-correlation energy and proposes the following formulation:

$$E_{xc}^{LDA}[n] = \int d^3r n(\vec{r}) e_{xc}^{HEG}(n(\vec{r})) \quad (1.4.17)$$

With $n(\vec{r})$ the local electronic density at \vec{r} .

Therefore, this approximation can be a good model for system close to the homogeneous electron gas^c. Moreover, LDA does not describe well long range interaction as it is focused on the local density. Among the most popular LDA functionals we can cite the Vosko-Wilk-Nusair (VWN) and the Perdew-Zunger (PZ).

Generalized Gradient Approximation

The main approximation that we use in this report is the Generalized Gradient Approximation (GGA). The purpose of this approximation is to describe the variation of the electron density in the frame of the local density approximation. To do so, functionals taking into account both the density (through LDA) and the gradient of the density of the system were constructed as:

$$E_{xc}^{GGA}[n, \sigma] = E_{xc}^{LDA}[n, \sigma] + \int d^3r f_{xc}^{GGA}(n(\vec{r}); s(\vec{r})) \quad (1.4.18)$$

With f_{xc}^{GGA} the exchange-correlation energy per electron in the generalized gradient approximation, and $s(\vec{r}) = \frac{|\nabla n(\vec{r})|}{(n(\vec{r}))^{\frac{4}{3}}}$.

This approximation is thus a correction of the local density approximation that extends it to non-homogeneous electron densities. As for the LDA, there are several non-equivalent GGA functional that differ by the particular choice of f_{xc}^{GGA} such as BLYP, PBE or PW91.

Pseudo-potentials

While representing the different electrons of the system, the pseudo-potentials characterize the way they will be taken into account during the calculations. Indeed, since only valence

^ci.e. with an electron density that does not vary too much

electrons are responsible of the chemical properties, a clever way to describe the system is to set an effective potential for core electrons, and describe valence states by pseudo-wavefunctions. Therefore, core states are frozen and valence orbitals are expanded in plane-waves via Bloch's theorem; the interaction between core and valence electrons are defined by the pseudo-potential.

$$\psi_{m,\vec{k}}(\vec{r}) = e^{i\vec{k}\vec{r}} u_{m,\vec{k}}(\vec{r}) \quad (1.4.19)$$

Where k is the wavevector and $u_{\vec{k}}(x)$ a periodic function having the periodicity of the crystal (\vec{G}).

$u_{m,\vec{k}}(\vec{r})$ is a periodic function, which can be expanded in a Fourier series running on the \vec{G} vectors as:

$$u_{m,\vec{k}}(\vec{r}) = \sum_{\{\vec{G}\}} \exp(i\vec{G}\vec{r}) \tilde{U}_m(\vec{k} + \vec{G}) \quad (1.4.20)$$

An exact representation of valence electrons implies an infinite expansion in plane-waves. Unfortunately, from a computational point of view an infinite expansion is not conceivable, thus a truncation is required.

Therefore we include in equation 1.4.20 expansion only the \vec{G} reciprocal lattice vectors such that:

$$\frac{\hbar^2 |\vec{k} + \vec{G}|^2}{2m} \leq E_{cut} \quad (1.4.21)$$

As the cutoff energy E_{cut} is systematically increased, the quality of the plane-wave basis improves and the corresponding total energy decreases. Although a large expansion gives a better description, a well-chosen cut-off energy can optimize the computational resource cost with a good description of wavefunctions.

Influence of Brillouin zone sampling

As we have seen, several parameters need to be checked and set correctly, in particular, the cut-off energy that depends upon the choice of pseudo-potential. Another parameter to be optimized is the number of k-points defining the Brillouin zone sampling. In order to describe many properties of the system, an integral over the wave vectors of the Brillouin zone is required. Let's consider $X(\vec{k})$ a function defined in the reciprocal space, which can be either the density of states, electron density, total energy or other physical quantity, we must compute its expectation value as:

$$\langle X \rangle = \frac{1}{\Omega_{BZ}} \sum \int X(\vec{k}) d^3k \quad (1.4.22)$$

With Ω_{BZ} the volume of the Brillouin zone.

This integral is computed via a discrete sum, by using a grid of k-points in the Brillouin zone. The thinner the grid, the better the precision, but the slower the calculation is.

Modelisation of Nuclear quantum effects

2.1 Introduction

Until recent awareness, the usual description of condensed matter systems implied a classical, Newtonian, description of nuclei while electrons were treated as quantum particles through well-known methods, as the DFT. Although NQE are known since Bohr and Planck discoveries, only recently efficient “all-quantum” methods treating both electrons and nuclei as quantum particle have emerged. With the development of these new methods, the importance of the NQE has been demonstrated in many cases.^{1,4,6,5} In this thesis, our approach aims to describe both nuclei and electrons as quantum particles, by the use of the DFT, PIMD, and QTB methods. While PIMD gives access to correct quantum distribution, QTB and RPMD allow describing the dynamical properties of a system through approximate velocity correlation functions.

Therefore, in this chapter, we will first describe the Langevin equation in order to introduce the QTB method. In the second part, we will focus on the Feynman description of quantum mechanics to depict the PIMD. Finally, we will present the RPMD method as derived from PIMD.

A detailed and reference book describing (not only) Path Integrals and related methods:
Mark Tuckerman. *Statistical mechanics: theory and molecular simulation*. Oxford university press, 2010

2.2 Langevin methods

While studying pollen particles through his microscope, the biologist R. Brown observed that their motions at the surface of water¹⁶ were irregular and somehow random, so-called *Brownian motion*. The physical mechanism behind Brown's observation remained unclear until 1905, where A. Einstein paved the way of the atomic theory and recent statistical mechanics approach.¹⁷ He described the diffusion process of a Brownian particle through a probabilistic description of atomic collisions between the latter and the fluid's molecules. This theory was then confirmed in 1909 by the work of J-B. Perrin.¹⁸ The Brownian motion description is therefore important in physics, one could cite the kinetic theory of gases, but also has a broader landscape of application as financial mathematics and is at the root of stochastic processes.

2.2.1 Langevin equation

In addition to Einstein's phenomenological description, P. Langevin proposed his approach in 1908,¹⁹ allowing one to describe the trajectory of such Brownian particles. To characterize Brownian motion, P. Langevin introduced two forces:

- a viscous friction force due to the fluid which is of the form $-\gamma\dot{x}$, following Stokes law, and characterized by the friction coefficient γ
- a random force $R(t)$ resulting from the random collisions with the fluid's molecules.

Therefore, for a particle of mass m in an external conservative potential, the Newtonian description of such Brownian motion leads to the Langevin equation (in one dimension):

Langevin equation

$$m\ddot{x} = -\nabla V(x) - m\gamma\dot{x} + R(t) \quad (2.2.1)$$

Where $f(x) = -\nabla V(x)$ describes the inter-atomic forces due to the conservative potential $V(x)$, m is the mass of the particle at the position $x(t)$, γ the friction coefficient, and $R(t)$ is the Langevin random force. Originally, the Langevin equation is given without the potential term.

Although devised for this, the Langevin equation applications are not restricted to the description of a Brownian particle immersed in a fluid but is generalizable to a broader landscape and is nowadays extensively used as a thermostat for molecular dynamics simulations. At this stage, we have to characterize the fluctuating Langevin force $R(t)$, and present the different approximations: first, the bath is assumed to be in a stationary state, in thermodynamic equilibrium. The random force is therefore described by a stationary stochastic process leading to the time-independent expectation value of the random force $\langle R(t) \rangle$ and $\langle R(t)R(t') \rangle$ only depends on the difference $t - t'$.

Besides, at rest, the particle should remain motionless on average, we, therefore, assume the expectation value of the random force to be null:

$$\langle R(t) \rangle = 0 \quad (2.2.2)$$

We now introduce the spectral densities of the position $S_x(\omega)$ and random force $S_R(\omega)$ through

the Wiener-Khintchine theorem:

$$\langle x(t)x(t+\tau) \rangle = \frac{1}{2\pi} \int_{-\infty}^{+\infty} S_x(\omega) e^{-i\omega\tau} d\omega \quad S_x(\omega) = \langle |x(\omega)|^2 \rangle \quad (2.2.3)$$

$$\langle R(t)R(t+\tau) \rangle = \frac{1}{2\pi} \int_{-\infty}^{+\infty} S_R(\omega) e^{-i\omega\tau} d\omega \quad S_R(\omega) = \langle |R(\omega)|^2 \rangle \quad (2.2.4)$$

As defined in Section 1.3, the classical fluctuation-dissipation theorem leads to the following relation between the power spectral density of the position $\tilde{S}_x(\omega)$ and the imaginary part of the generalized susceptibility $\chi''(\omega)$:

$$\tilde{S}_x(\omega) = \frac{2k_b T}{\omega} \chi''(\omega) \quad (2.2.5)$$

Through linear response theory, the generalized susceptibility links the position and random forces Fourier transforms as:

$$\tilde{x}(\omega) = \tilde{\chi}(\omega) \tilde{R}(\omega) \quad (2.2.6)$$

Which thus leads to the following relation:

$$\tilde{S}_x(\omega) = |\tilde{\chi}(\omega)|^2 S_R(\omega) \quad (2.2.7)$$

We can now replace the power spectral density of the position in equation 2.2.5:

$$\tilde{S}_R(\omega) = \frac{\omega}{2k_b T} \frac{\chi''(\omega)}{|\tilde{\chi}(\omega)|^2} \quad (2.2.8)$$

For simplicity sake, as we work in the linear response frame, we consider a simple one dimension harmonic oscillator at frequency ω_0 . This result can be easily generalized by considering the expansion 1.3.22. In this context, in order to determine the definition of the generalized susceptibility, one can deduce from the Fourier transform of the Langevin equation that:

$$\tilde{x}(\omega) = \frac{1}{(-m\omega^2 + i\gamma m\omega + m\omega_0^2)} \tilde{R}(\omega) \quad (2.2.9)$$

Where the definition of the generalized susceptibility naturally writes:

$$\tilde{\chi}(\omega) = \frac{1}{(-m\omega^2 + i\gamma m\omega + m\omega_0^2)} \quad (2.2.10)$$

Hence we have:

$$|\tilde{\chi}(\omega)|^2 = \frac{1}{m^2((\omega^2 - \omega_0^2)^2 + \gamma^2\omega^2)} \quad (2.2.11)$$

And the imaginary part of the generalized susceptibility is thus:

$$\chi''(\omega) = \frac{\gamma\omega}{m^2((\omega^2 - \omega_0^2)^2 + \gamma^2\omega^2)} \quad (2.2.12)$$

Finally, we end up characterizing the random force with the relation between the power spectral density of the latter and the dissipation coefficient by replacing these terms in equation 2.2.8:

Langevin white noise

$$\tilde{S}_R(\omega) = 2m\gamma k_b T \quad (2.2.13)$$

The FDT in its classical form applied to the Langevin equation, therefore describes the random force as being a Gaussian white noise. On the right-hand side of the latter definition, we find the classical thermal term $k_b T$ as being the same for all ω modes, according to the equipartition theorem. The latter definition leads to the classical Langevin thermostat, where a classical particle is plunged into a classical bath, at temperature T.

2.2.2 Quantum Thermal Bath

The Langevin thermostat is commonly used in molecular dynamics simulation to sample the canonical distribution. However, in the latter definition, the quantum nature of the particle is completely neglected. In order to take into account NQE, Dammak and coworkers introduced in 2009 a new method,³ the QTB, based on the Langevin equation, but characterizing the random force through the quantum FDT:

$$\tilde{S}_x(\omega) = \hbar \coth\left(\frac{\beta\hbar\omega}{2}\right) \chi''(\omega) \quad (2.2.14)$$

Which can be recast as:

$$\tilde{S}_x(\omega) = 2\hbar \left(\frac{1}{2} + \frac{1}{e^{\beta\hbar\omega} - 1}\right) \chi''(\omega) \quad (2.2.15)$$

Noticing that:

$$\coth\left(\frac{\beta\hbar\omega}{2}\right) = \frac{e^{\beta\hbar\omega} - 1 + 2}{e^{\beta\hbar\omega} - 1} \quad (2.2.16)$$

$$= 2 \left(\frac{1}{2} + \frac{1}{e^{\beta\hbar\omega} - 1}\right) \quad (2.2.17)$$

Therefore, following the same derivation as for the classical FDT, we obtain the following definition of the random force:

Quantum Thermal Bath Colored noise

$$\tilde{S}_R(\omega) = 2m\gamma\hbar\omega \left(\frac{1}{2} + \frac{1}{e^{\beta\hbar\omega} - 1}\right) \quad (2.2.18)$$

In this framework, the power spectral density of the random force now depends on the frequency, leading to a Gaussian colored noise. On the right-hand side of this definition, we find the quantum energetic term of the mode ω as the sum of the zero-point energy $\frac{\hbar\omega}{2}$ and the Bose-Einstein distribution. Each mode is thus thermalized with an appropriate effective temperature accounting for the zero-point energy. In contrast with the white noise derived from the classical FDT, the QTB colored noise does not vanish in the low-temperature limit, reducing the energy term to the zero-point energy:

$$\lim_{T \rightarrow 0} \tilde{S}_R(\omega) = 2m\gamma \frac{\hbar\omega}{2} \quad (2.2.19)$$

However at high temperature the system reaches the classical limit, leading to the same expression as the classical white noise:

$$\lim_{T \rightarrow \infty} \tilde{S}_R(\omega) = 2m\gamma k_b T \quad (2.2.20)$$

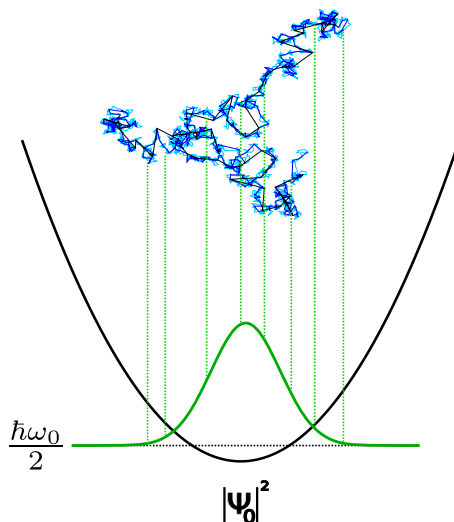


Figure 2.1. Description of the quantum distribution sampling through QTB simulations

So defined, the QTB method allows one to have access to NQE through the colored noise embedded in the Langevin equation. However, the system remains a classical object; therefore, this method describes a classical particle plunged in a quantum bath. The quantum distributions can, thus, be extracted from the trajectories propagated by the QTB, as schematically represented in Figure 2.1.

Although the QTB method is exact in the harmonic limit, while dealing with anharmonicity, this semi-classical approach is subjected to the Zero-Point Energy Leakage (ZPEL). Indeed, in this framework, the coupling between the modes of the classical system can induce an energy redistribution between them, which tends toward classical energy equipartition. This implies high-frequency modes to end up with a lower effective temperature while lower ones to be higher and could imply non-physical behavior of the system under study. However, the friction coefficient γ can be tuned to save the day. Indeed, the latter parameter couples the system to the bath and can be increased to lower the ZPEL effect, the main downside being a broadening of the vibrational spectra. In addition, a recent development²⁰ brought out a new criterion derived from the FDT to quantify the ZPEL and estimate $\chi''(\omega)$ along the trajectories, allowing the use of equation 2.2.14 in an adaptive scheme of the friction coefficient, giving rise to the adaptive-QTB addressing the departure of QTB from the quantum FDT.

Despite its drawbacks, the QTB approach has been successfully applied to several systems.^{4,5,6,21,22} Moreover, not only can it give access to NQE but also provide somewhat reliable vibrational spectra⁷ in many different systems. Finally, combined with ab-initio simulations for the determination of the forces, this approximation is computationally inexpensive and therefore can be applied for large systems with many degrees of freedom in contrast with accurate but costly PIMD simulations.

In this work, we decided to use the QTB method as a magnifying glass to probe NQE in the different systems and also to obtain reliable vibrational spectra to be compared with experimental results. Then, we used more sophisticated approaches to sample the correct quantum distributions.

2.3 Path integral formalism

Based on the work presented in 1933 by P. Dirac on the use of Lagrangian in quantum mechanics,²³ in 1948, R. Feynman introduced a new formalism of quantum mechanics²⁴ based on a generalization of the classical action principle. The idea behind the so-called path integral formalism is the following: the quantum amplitude for a particle at position x_i at time t_i to reach the position x_f at time t_f is given by the sum over all possible paths linking the two points weighted by their respective classical action $S[x(t)]$.

$$\langle x_f; t_f | x_i; t_i \rangle = \int \mathcal{D}x(t) e^{\frac{i}{\hbar} S[x(t)]} \quad (2.3.1)$$

Doing so, both the classical action arising from the minimum action principle as the integral of the Lagrangian, and an infinite number of non-classical actions contribute to the quantum amplitude. The Feynman path integral formalism satisfies the Schrödinger equation, and one can notice that the classical regime is also accessible. Indeed in the case $\hbar \rightarrow 0$ the weighted factor $e^{\frac{i}{\hbar} S[x(t)]}$ is oscillating rapidly, thus the main contribution arises from the stationary path, hence the classical action.

In this section, we will first define the density operator in the path integral formalism and its properties. Then we will use this new definition to recast the canonical partition function from which the classical isomorphism will naturally outcome. Finally, we will present a molecular dynamics scheme for the path integral formalism to take into account the NQE and briefly describe an approximate approach to extract time correlation functions.

To begin, we consider Hamiltonian operator \hat{H} as the sum of the kinetic \hat{T} and potential \hat{V} operators:

$$\hat{H} = \hat{T} + \hat{V} \quad (2.3.2)$$

For the sake of clarity, we redefine the density operator in equation 1.2.43 as follows:

$$\hat{\rho}_{eq} = e^{-\beta \hat{H}} \quad (2.3.3)$$

So that the partition function is now defined as the trace of the density operator:

$$\mathcal{Z} = \text{Tr}(\hat{\rho}_{eq}) \quad (2.3.4)$$

The idea behind path integrals resides in the reformulation of the space-coordinate quantum propagator matrix elements $\mathcal{U}(x, x'; \tau)$ (equation 1.2.19) in terms of a sum over all possible path from x to x' in time τ . Therefore, in this context, we want to treat the density operator in space-coordinate which matrix elements are:

$$\rho_{eq}(x, x'; \beta) = \langle x | \hat{\rho}_{eq} | x' \rangle \quad (2.3.5)$$

There are several derivations of the final expression (equation 2.3.22), here we present it through the convolution property of the density operator.

• Convolution property

Let us define the convolution product C between the two density operators matrix elements $\rho_{eq}(x, x'; \beta_1)$ and $\rho_{eq}(x', x''; \beta_2)$ at different temperature β_1 and β_2 :

$$C = \int dx' \rho_{eq}(x, x'; \beta_1) \rho_{eq}(x', x''; \beta_2) \quad (2.3.6)$$

Then introducing definition 2.3.5 in this equation leads to:

$$C = \int dx' \sum_{i,j} |\Psi_i(x)\rangle e^{-\beta_1 E_i} \langle \Psi_i(x') | \Psi_j(x') \rangle e^{-\beta_2 E_j} \langle \Psi_j(x'') | \quad (2.3.7)$$

$$= \sum_{i,j} |\Psi_i(x)\rangle e^{-\beta_1 E_i} \int dx' \langle \Psi_i(x') | \Psi_j(x') \rangle e^{-\beta_2 E_j} \langle \Psi_j(x'') | \quad (2.3.8)$$

$$= \sum_i |\Psi_i(x)\rangle e^{-\beta_1 E_i} e^{-\beta_2 E_i} \langle \Psi_i(x'') | \quad (2.3.9)$$

$$= \sum_i |\Psi_i(x)\rangle e^{-(\beta_1 + \beta_2) E_i} \langle \Psi_i(x'') | \quad (2.3.10)$$

We finally end up with the practical property of the space-coordinate canonical density operator:

$$C = \int dx' \rho_{eq}(x, x'; \beta_1) \rho_{eq}(x', x''; \beta_2) = \hat{\rho}_{eq}(x, x''; \beta_1 + \beta_2) \quad (2.3.11)$$

Therefore, the convolution of $\rho_{eq}(x, x'; \beta_1)$ at temperature β_1 and $\rho_{eq}(x', x''; \beta_2)$ at β_2 defines a new density operator matrix elements $\rho_{eq}(x, x''; \beta_1 + \beta_2)$ at temperature $\beta_1 + \beta_2$. The underlying effect of this property is thus to be able from a density matrix defined as temperature β to compute the density matrix at lower temperature but evaluated at two different positions. Indeed, if we consider the case $\beta_1 = \beta_2 = \beta$ in equation 2.3.11 we find that:

$$\hat{\rho}_{eq}(x, x''; 2\beta) = \int dx' \rho_{eq}(x, x'; \beta) \rho_{eq}(x', x''; \beta) \quad (2.3.12)$$

Then using the same convolution property on $\rho_{eq}(x, x''; 2\beta)$ we can compute another matrix element $\rho_{eq}(x, x'''; 4\beta)$ at twice lower temperature, repeating the process thus gives access to $\rho_{eq}(x, x^{(P)}; P\beta)$ in the full quantum regime $T \rightarrow 0$. However, one can notice that it requires an integral over all $x^{(i)}$ elements, so define “path integrals”. In addition, we can also notice that expanding this convolution property produces paths equally distributed in terms of β which therefore acts as a “duration” or “slice” of an imaginary time as we will now discuss.

• Imaginary time slicing

To introduce the imaginary time slicing, we recall the definition of the quantum propagator operator (equation 1.2.13) whose space-coordinate matrix elements are defined as:

$$\langle x | \hat{\mathcal{U}}(\tau) | x' \rangle = \mathcal{U}(x, x'; t, t_0) \quad (2.3.13)$$

$$= \mathcal{U}(x, x'; \tau) \quad (2.3.14)$$

In this way we can derive the relationship between the canonical density operator $\hat{\rho}(\beta)$ and the quantum propagator $\hat{\mathcal{U}}(\tau)$:

$$\hat{\rho}(\beta) = \hat{\mathcal{U}}(-i\beta\hbar) \quad (2.3.15)$$

$$\hat{\mathcal{U}}(\tau) = \hat{\rho}\left(\frac{-i}{\hbar}\tau\right) \quad (2.3.16)$$

As suggested before, we find that the density operator at temperature β can be expressed as a quantum propagator which evolves the system in an imaginary time $-i\beta\hbar$. On the other hand, the quantum propagator can be seen as a density operator at a temperature $-\frac{i}{\hbar}\tau$. This operation is known as the Wick rotation. Thus, introducing the convolution property of the density operator in the latter expression allows expressing the quantum propagator as a sum over all P paths $x^{(i)}$ of the density operator evaluated at the temperature $-\frac{i}{\hbar}\frac{\tau}{P}$. This approach is schematically described in Figure 2.2 and describes the onset of Feynman path integrals formulation of quantum mechanics.

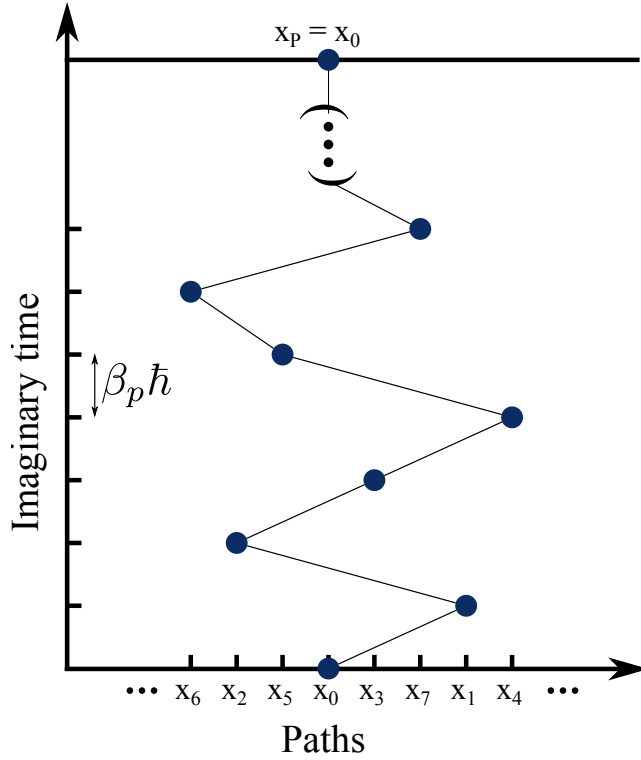


Figure 2.2. Description of time slicing within path integrals

2.3.1 Path Integral Molecular Dynamics

In this section, we take advantage of the Feynman's path integrals to derive a simulation scheme to introduce NQE in our molecular dynamics simulations.

We start from the definition of the partition function:

$$\mathcal{Z} = \text{Tr}(\hat{\rho}_{eq}) = \int dx \langle x | \hat{\rho}_{eq} | x \rangle \quad (2.3.17)$$

We then rename x to x_0 for the sake of clarity in the following and introduce the space-coordinate density matrix element:

$$\mathcal{Z} = \int dx_0 \rho_{eq}(x_0, x_0; \beta) \quad (2.3.18)$$

Then we introduce P times the convolution property 2.3.11:

$$\mathcal{Z} = \int dx_0 \int dx_1 \rho_{eq}(x_0, x_1; \frac{\beta}{2}) \rho_{eq}(x_1, x_0; \frac{\beta}{2}) \quad (2.3.19)$$

$$= \int dx_0 \int dx_1 \int dx_2 \rho_{eq}(x_0, x_2; \frac{\beta}{4}) \rho_{eq}(x_2, x_1; \frac{\beta}{4}) \rho_{eq}(x_1, x_2; \frac{\beta}{4}) \rho_{eq}(x_2, x_0; \frac{\beta}{4}) \quad (2.3.20)$$

$$= \int dx_0 dx_1 \dots dx_{P-1} \rho_{eq}(x_0, x_1; \frac{\beta}{P}) \rho_{eq}(x_1, x_2; \frac{\beta}{P}) \dots \rho_{eq}(x_{P-1}, x_0; \frac{\beta}{P}) \quad (2.3.21)$$

$$= \int dx_0 \dots dx_{P-1} \langle x_0 | \hat{\rho}_{eq}(\frac{\beta}{P}) | x_1 \rangle \langle x_1 | \hat{\rho}_{eq}(\frac{\beta}{P}) | x_2 \rangle \dots \langle x_{P-1} | \hat{\rho}_{eq}(\frac{\beta}{P}) | x_0 \rangle \quad (2.3.22)$$

Finally we end up with a new definition of the canonical partition function in the path integral formalism:

$$\mathcal{Z} = \int dx_0 \dots dx_{P-1} \langle x_0 | e^{-\beta_p \hat{H}} | x_1 \rangle \dots \langle x_{P-1} | e^{-\beta_p \hat{H}} | x_0 \rangle \quad (2.3.23)$$

where we defined: $\beta_P = \frac{\beta}{P}$.

We now want to expand the density operator despite the fact that the kinetic and potential part of the hamiltonian operator do not commute:

$$e^{-\beta_P \hat{H}} = e^{-\beta_P (\hat{T} + \hat{V})} \quad (2.3.24)$$

$$\neq e^{-\beta_P \hat{T}} e^{-\beta_P \hat{V}} \quad (2.3.25)$$

To overcome this issue, we note that β_P can be infinitely small when $P \rightarrow \infty$ and we take advantage of the symmetric Baker-Campbell-Hausdorff formula²⁵ leading to:

$$e^{-\beta_P (\hat{T} + \hat{V})} = \lim_{P \rightarrow \infty} e^{-\beta_P \frac{\hat{V}}{2}} e^{-\beta_P \hat{T}} e^{-\beta_P \frac{\hat{V}}{2}} + \mathcal{O}(\beta_P^2) \quad (2.3.26)$$

Which, when introduced into equation 2.3.23, leads to the symmetric Trotter expansion:

$$e^{-\beta (\hat{T} + \hat{V})} = \lim_{P \rightarrow \infty} \left[e^{-\beta_P \frac{\hat{V}}{2}} e^{-\beta_P \hat{T}} e^{-\beta_P \frac{\hat{V}}{2}} \right]^P + \mathcal{O}(\beta_P^2) \quad (2.3.27)$$

We thus obtain under this approximation:

$$\hat{\rho}_{eq}(\beta_P) = e^{-\beta_P \frac{\hat{V}}{2}} e^{-\beta_P \hat{T}} e^{-\beta_P \frac{\hat{V}}{2}} \quad (2.3.28)$$

Therefore:

$$\mathcal{Z} = \lim_{P \rightarrow \infty} \int dx_0 \dots dx_{P-1} \langle x_0 | \hat{\rho}_{eq}(\beta_P) | x_1 \rangle \dots \langle x_{P-1} | \hat{\rho}_{eq}(\beta_P) | x_0 \rangle \quad (2.3.29)$$

From which we evaluate the matrix elements $\langle x_i | \hat{\rho}_{eq}(\beta_P) | x_{i+1} \rangle$:

$$\langle x_i | \hat{\rho}_{eq}(\beta_P) | x_{i+1} \rangle = \langle x_i | e^{-\beta_P \frac{\hat{V}}{2}} e^{-\beta_P \hat{T}} e^{-\beta_P \frac{\hat{V}}{2}} | x_{i+1} \rangle \quad (2.3.30)$$

$$= e^{-\beta_P \frac{V(x_i)}{2}} \langle x_i | e^{-\beta_P \hat{T}} | x_{i+1} \rangle e^{-\beta_P \frac{V(x_{i+1})}{2}} \quad (2.3.31)$$

$$= e^{-\frac{\beta_P}{2} (V(x_i) + V(x_{i+1}))} \langle x_i | e^{-\beta_P \hat{T}} | x_{i+1} \rangle \quad (2.3.32)$$

We then introduce the closure relation $\int dp |p\rangle \langle p| = 1$ and evaluate the kinetic part of the density operator in the momentum-coordinate, leading to:

$$\langle x_i | \hat{\rho}_{eq}(\beta_P) | x_{i+1} \rangle = e^{-\frac{\beta_P}{2} (V(x_i) + V(x_{i+1}))} \int dp \langle x_i | p \rangle \langle p | e^{-\beta_P \hat{T}} | x_{i+1} \rangle \quad (2.3.33)$$

$$= e^{-\frac{\beta_P}{2} (V(x_i) + V(x_{i+1}))} \int dp e^{-\beta_P \frac{p^2}{2m}} \langle x_i | p \rangle \langle p | x_{i+1} \rangle \quad (2.3.34)$$

Then recalling that $\langle x | p \rangle = \frac{1}{\sqrt{2\pi\hbar}} e^{\frac{i}{\hbar} p x}$ we obtain:

$$\langle x_i | \hat{\rho}_{eq}(\beta_P) | x_{i+1} \rangle = e^{-\frac{\beta_P}{2} (V(x_i) + V(x_{i+1}))} \frac{1}{2\pi\hbar} \int dp e^{\frac{ip}{\hbar} (x_i - x_{i+1})} e^{-\beta_P \frac{p^2}{2m}} \quad (2.3.35)$$

We define:

$$A = \frac{\beta_P}{2m} \quad B = \frac{i}{\hbar} (x_i - x_{i+1}) \quad (2.3.36)$$

So that:

$$-\frac{\beta_P}{2m} p^2 + \frac{i}{\hbar} (x_i - x_{i+1}) p = -[Ap^2 - Bp] = -A \left[p - \frac{B}{2A} \right]^2 - \frac{B^2}{4A} \quad (2.3.37)$$

Allowing us to integrate by completing the square:

$$\int dp e^{\frac{iP}{\hbar}(x_i - x_{i+1})} e^{-\beta p \frac{p^2}{2m}} = \int dp e^{-A[p - \frac{B}{2A}]^2} e^{-\frac{B^2}{4A}} \quad (2.3.38)$$

$$= e^{-\frac{B^2}{4A}} \int dp e^{-A[p - \frac{B}{2A}]^2} \quad (2.3.39)$$

We then apply the change of variable $z = p - \frac{B}{2A}$ and take advantage of the gaussian integral:

$$\int dp e^{\frac{iP}{\hbar}(x_i - x_{i+1})} e^{-\beta p \frac{p^2}{2m}} = e^{-\frac{B^2}{4A}} \int dz e^{-Az^2} \quad (2.3.40)$$

$$= \sqrt{\frac{\pi}{A}} e^{-\frac{B^2}{4A}} \quad (2.3.41)$$

$$= \sqrt{\frac{2m\pi}{\beta_P}} e^{-\frac{m(x_i - x_{i+1})^2}{2\hbar^2 \beta_P}} \quad (2.3.42)$$

Hence:

$$\langle x_i | \hat{\rho}_{eq}(\beta_P) | x_{i+1} \rangle = e^{-\frac{\beta_P}{2}(V(x_i) + V(x_{i+1}))} \sqrt{\frac{m}{2\pi\beta_P\hbar^2}} e^{-\frac{m(x_i - x_{i+1})^2}{2\hbar^2 \beta_P}} \quad (2.3.43)$$

$$= \sqrt{\frac{m}{2\pi\beta_P\hbar^2}} e^{-\frac{\beta_P}{2}(V(x_i) + V(x_{i+1})) - \frac{m(x_i - x_{i+1})^2}{2\hbar^2 \beta_P}} \quad (2.3.44)$$

We can now introduce these matrix elements in the definition of the partition function:

$$\mathcal{Z} = \lim_{P \rightarrow \infty} \left(\frac{m}{2\pi\beta_P\hbar^2} \right)^{\frac{P}{2}} \int dx_0 \dots dx_{P-1} e^{-\left[\sum_{i=0}^{P-1} \frac{\beta_P}{2}(V(x_i) + V(x_{i+1})) + \frac{m(x_i - x_{i+1})^2}{2\hbar^2 \beta_P} \right]} \quad (2.3.45)$$

Where one can see that:

$$\sum_{i=0}^{P-1} [V(x_i) + V(x_{i+1})] = 2 \sum_{i=0}^{P-1} V(x_i) \quad (2.3.46)$$

Which simplifies the expression to:

$$\mathcal{Z} = \lim_{P \rightarrow \infty} \left(\frac{m}{2\pi\beta_P\hbar^2} \right)^{\frac{P}{2}} \int dx_0 \dots dx_{P-1} e^{-\left[\sum_{i=0}^{P-1} \beta_P V(x_i) + \frac{m(x_i - x_{i+1})^2}{2\hbar^2 \beta_P} \right]} \quad (2.3.47)$$

Finally, we introduce series of gaussian integrals through the prefactor:

$$\left(\frac{m}{2\pi\beta_P\hbar^2} \right)^{\frac{1}{2}} = \frac{1}{2\pi\hbar} \int dp e^{-\frac{\beta_P}{2m} p^2} \quad (2.3.48)$$

Leading to:

$$\mathcal{Z} = \lim_{P \rightarrow \infty} \left(\frac{1}{4\pi^2\hbar^2} \right)^{\frac{P}{2}} \int dp_0 \dots dp_{P-1} \int dx_0 \dots dx_{P-1} e^{-\left[\sum_{i=0}^{P-1} \frac{\beta_P}{2m_i} p_i^2 + \beta_P V(x_i) + \frac{m(x_i - x_{i+1})^2}{2\hbar^2 \beta_P} \right]} \quad (2.3.49)$$

In order to clarify the expression, we define:

$$\omega_P = \frac{\sqrt{P}}{\beta\hbar} \quad (2.3.49)$$

$$U_{eff} = \sum_{i=0}^{P-1} \frac{1}{P} V(x_i) + \frac{1}{2} m \omega_P^2 (x_i - x_{i+1})^2 \quad (2.3.50)$$

$$\tilde{m}_i = \frac{\sqrt{P}}{\beta\hbar} \quad (2.3.51)$$

Leading to the final form of the canonical partition function in the path integral formalism:

Path integral canonical partition function

$$\mathcal{Z} = \lim_{P \rightarrow \infty} \left(\frac{1}{h} \right)^P \int dp_0 \dots dp_{P-1} \int dx_0 \dots dx_{P-1} e^{-\beta_p \left[\sum_{i=0}^{P-1} \frac{p_i^2}{2\tilde{m}_i} + U_{eff}(x_0 \dots x_{P-1}) \right]} \quad (2.3.52)$$

• **Classical isomorphism**

The term in the exponential can be recast as a Hamiltonian H_{rp} describing a ring polymer lying in the potential $\frac{V(x_i)}{P}$, the beads of the ring polymer necklace interacting via harmonic forces between nearest neighbors, with a frequency ω_p which is usually called the intra-chain frequency:

$$H_{rp}(p, x) = \sum_{i=0}^{P-1} \frac{p_i^2}{2\tilde{m}_i} + U_{eff}(x_0 \dots x_{P-1}) \quad (2.3.53)$$

$$= \sum_{i=0}^{P-1} \frac{p_i^2}{2\tilde{m}_i} + \frac{1}{P} V(x_i) + \frac{1}{2} m \omega_p^2 (x_i - x_{i+1})^2 \quad (2.3.54)$$

Therefore, the path integral canonical partition function:

$$\mathcal{Z} = \lim_{P \rightarrow \infty} \left(\frac{1}{h} \right)^P \int dp_0 \dots dp_{P-1} \int dx_0 \dots dx_{P-1} e^{-\beta_p H_{rp}} \quad (2.3.55)$$

is analogous to the classical canonical partition function of a ring polymer at an effective temperature $\frac{\beta}{P}$. This analogy is known as the classical isomorphism which therefore allows representing a quantum particle as a classical ring polymer, for a number of beads composing this ring which tends to infinity. The description of the interaction between the beads is presented in Figure 2.3. Let's note that any operator is here evaluated as an average over equivalent beads ($i=1, \dots, P$) at different configurations. The beads are therefore distinguishable objects. The

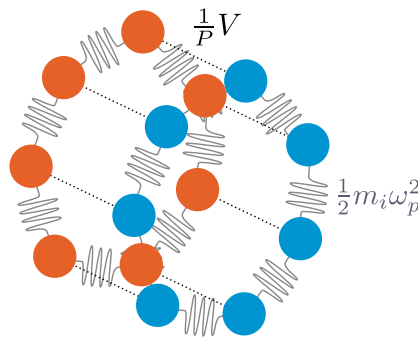


Figure 2.3. Description of the interactions between classical ring polymer.

generalization to a number N of particles in a 3-dimensional space is straightforward, and one can obtain the following generalized ring polymer hamiltonian:

$$H_{rp}(p, q) = \sum_{i=0}^{P-1} \left[\sum_{n=1}^N \frac{p_n^{(i)2}}{2\tilde{m}_n} + \frac{1}{P} V(q_1^{(i)}, \dots, q_N^{(i)}) + \frac{1}{2} m_n \omega_p^2 (q_n^{(i+1)} - q_n^{(i)})^2 \right] \quad (2.3.56)$$

Where the first sum is over the beads and the second over the N particles of the system. Thanks to this description, a molecular dynamics scheme can be derived from the Hamiltonian H_{rp} . Hamilton equations give us:

$$\dot{q}_n^{(i)} = \frac{\partial H_{rp}}{\partial p_n^{(i)}} \quad \dot{p}_n^{(i)} = -\frac{\partial H_{rp}}{\partial q_n^{(i)}} \quad (2.3.57)$$

$$= \frac{p_n^{(i)}}{\tilde{m}_n} \quad = -m\omega_p^2(2q_n^{(i)} - q_{n+1}^{(i)} - q_{n-1}^{(i)}) - \frac{1}{P} \frac{\partial V(q_1^{(i)}, \dots, q_N^{(i)})}{\partial q_n^{(i)}} \quad (2.3.58)$$

Thanks to this approach, one has access to the quantum distributions through the ring polymer dynamics governed by the latter hamiltonian, as presented in Figure 2.4. Finally, these equations can be coupled to a thermostat to ensure proper canonical sampling.

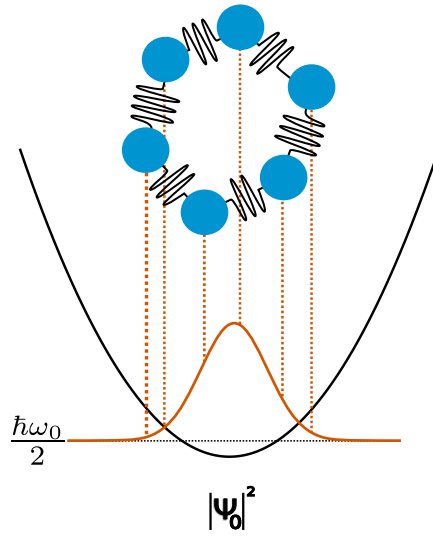


Figure 2.4. Description of the quantum distribution sampling through PIMD simulations

2.3.2 Ring Polymer Molecular Dynamics

Although in principle exact for quantum distributions in the $P \rightarrow \infty$ limit, the PIMD does not give access to dynamical properties. Missing these properties not only prevents one to explore dynamical processes such as diffusion behaviors or reaction rates but also make impossible the systematic comparison with a large part experimental results, in particular concerning vibrational spectra.

• Time correlation function

Therefore, before describing one way to obtain such information, we first recall some properties of time correlation functions. In Section 1.3 we described several correlation functions in particular, the standard quantum time correlation function defined as:

$$C_{AB}(t) = \langle \hat{A}(0)\hat{B}(t) \rangle \quad (2.3.59)$$

However, other correlation functions can be used. In particular, the Kubo correlation function:

$$K_{AB}(t) = \frac{1}{\beta \mathcal{Z}(\beta)} \int_0^\beta d\lambda \text{Tr} \left(e^{-(\beta-\lambda)\hat{H}} \hat{A} e^{-\lambda\hat{H}} e^{i\hat{H}t} \hat{B} e^{-i\hat{H}t} \right) \quad (2.3.60)$$

is real valued and invariant under time reversal making it more symmetrical than the quantum time correlation function. In addition, it is more comparable to the classical correlation function. Moreover, as we have seen it is linked to the standard correlation function as:

$$\tilde{C}_{AB}(\omega) = \frac{\beta\omega}{1 - e^{-\beta\omega}} \tilde{K}_{AB}(\omega) \quad (2.3.61)$$

Therefore, the Kubo correlation function appears to be a better choice as compared to the standard quantum correlation function, in particular for semi-classical approaches. Non-surprisingly, several approaches to approximate the latter correlation function have been investigated. In particular, the Centroid Molecular Dynamics (CMD)²⁶ and more recently RPMD²⁷ have been applied successfully to address dynamical concerns in several systems. Recently, these two approaches were rederived as a particular approximation of the more general mean-field framework of Matsubara dynamics.²⁸ In the following, we chose to describe the formalism of the Ring Polymer Molecular Dynamics as this approximation was used in the present study.

• The Ring Polymer Molecular Dynamics formalism

In 2004²⁷ I. R. Craig and D. E. Manolopoulos introduced the so-called RPMD method allowing one to have access to approximate Kubo correlation function in the path integral scheme. Following previous work,²⁹ they chose the fictitious mass \tilde{m} of each bead to be the physical one. In this formalism the Hamiltonian defined in equation 2.3.56 can be used to propagate classical molecular dynamics trajectories in an extended phase space of P degrees of freedom with an effective classical temperature of $T^* = PT$.

The expectation value of an operator $A(\mathbf{x})$ is, therefore:

$$\langle \hat{A} \rangle = \frac{1}{\mathcal{Z}} \text{Tr} \left(\rho_{eq} \hat{A} \right) \quad (2.3.62)$$

$$= \frac{1}{(2\pi\hbar)^P \mathcal{Z}} \int d\mathbf{p} \int d\mathbf{x} e^{-\beta_p H_{rp}(\mathbf{p}, \mathbf{x})} A_P(\mathbf{x}) \quad (2.3.63)$$

With $d\mathbf{x} = dx_0, \dots, dx_{P-1}$ and $d\mathbf{p} = dp_0, \dots, dp_{P-1}$
Where $A_P(\mathbf{x})$ is averaged over all the beads:

$$A_P(\mathbf{x}(t)) = \frac{1}{P} \sum_{i=0}^{P-1} A(\mathbf{x}_i(t)) \quad (2.3.64)$$

In analogy equation 2.3.63 I. R. Craig and D. E. Manolopoulos generalized this definition to a product of two operators $\hat{A}(\mathbf{x})$ and $\hat{B}(\mathbf{x})$ which naturally leads to the Kubo time correlation function of the two operators in the short time limit:

$$\langle \hat{A}\hat{B} \rangle = \frac{1}{(2\pi\hbar)^P \mathcal{Z}} \int d\mathbf{p} \int d\mathbf{x} e^{-\beta_p H_{rp}(\mathbf{p}, \mathbf{x})} A_p(\mathbf{x}) B_p(\mathbf{x}) \quad (2.3.65)$$

$$= \lim_{t \rightarrow 0} K_{AB}(t) \quad (2.3.66)$$

Therefore, thanks to this analogy, the RPMD method approximates the Kubo correlation function as:

Ring Polymer Molecular Dynamics Kubo correlation function

$$K_{AB}(t) \approx \frac{1}{(2\pi\hbar)^P \mathcal{Z}(\beta)} \int d\mathbf{p} \int d\mathbf{x} e^{-\beta_p H_p(\mathbf{p}, \mathbf{x})} A_p(\mathbf{x}(0)) B_p(\mathbf{x}(t)) \quad (2.3.67)$$

Although the expression 2.3.66 is an approximation which cannot be derived formally, it can be shown to be exact in the classical limit of high temperature, in the short time limit, for the simple case of the harmonic oscillator and finally in the case of unitary operators.

2.4 Conclusion

In this section, we described two methods allowing the quantum description of nuclei in our molecular dynamics simulations. The QTB is derived from the Langevin equation; it is a semi-classical approach to account for the NQE, and in particular, the zero-point energy. In addition to approximate quantum distributions, this method also provides reliable vibrational spectra, which is a required asset while comparing theoretical results with experimental ones. Moreover, the QTB scheme is computationally cheap while it is used on top of ab-initio calculations accounting for inter-atomic forces. However, due to the inherent semi-classical model, QTB is subjected to ZPEL. Although it can be reduced by tuning the coupling between the system and the quantum bath, while dealing with strong anharmonic systems, it can lead to incorrect physical properties. Therefore, QTB has to be carefully used, and the resulting physical properties systematically checked whether by investigating the effective temperature of the different degrees of freedom or with more sophisticated approaches recently brought out.

On the other hand, in contrast with QTB, PIMD which arises from the Feynman quantum mechanics formalism, provides correct quantum distributions at equilibrium and in the limit of a high number of replicas (beads) of the system. The inherent drawback being the computational cost of each simulation. Although recent development allows reducing the number of replicas significantly to reach convergence, PI-based methods providing correct quantum time correlation functions are still lacking. Therefore, several approximations to the Kubo correlation function, as RPMD and CMD, have been derived in order to obtain approximate time correlation function in the PI framework. However, these two methods are expensive in comparison with QTB and do not provide deeper information concerning the dynamical properties of the studied systems.

Therefore, we see in both QTB and PIMD two complementary methods to sample the NQE in our investigations. We used the QTB as a magnifying glass to probe NQE and also to obtain reliable vibrational spectra from the velocities correlation function. Doing so, we can have a fast and cheap way to obtain the pressure or temperature of interest for example. Then, we used PIMD simulations to obtain correct quantum distributions and a finer description of the different physical behaviors.

Phase transitions description

3.1 Introduction

In the following, we discuss two methods to understand the underlying process of phase transition.

As a first approach, the NEB method allows finding the Minimum Energy Reaction Path (MEP) and the saddle point of a transition, given a set of intermediate configurations that are optimized. Secondly, the MTD method allows sampling the free energy landscape in a Molecular Dynamics (MD) scheme allowing one to add thermal and quantum effect. The latter approach, however, requires to define a coordinate of reaction/transition. Therefore, in the last part, we will present the Path CVs along with the Path Invariant Vector (PIV), which will allow one to describe a transition through topological concerns.

3.2 Minimum energy path sampling with Nudged Elastic Band

The NEB method allows determining under certain conditions the MEP of a transition. It is common while dealing with phase transitions or chemical reactions to know the initial and final states of the latter. However, the processes behind a transition can be complex, and the different stages could remain unknown. In order to explore the different transition stages, the NEB method allows one to optimize a series of images of the related system along the transition.

We are looking for the different steps of the transition of a system of N atoms at initial positions $r_1^0, r_2^0, \dots, r_N^0$ and final positions r_1^F, \dots, r_N^F defining the initial $R_0(r_1^0, \dots, r_N^0)$ and the final $R_F(r_1^F, \dots, r_N^F)$ configurations. Given a number of images K , we construct a series of K intermediate configurations $R_i(r_1^i, \dots, r_N^i); i = 1, \dots, K$ by linear interpolation of the extreme configurations R_0 and R_F . Then, we link all images with springs of constant k_s and keep the extreme configurations ($i = 1, K$) fixed.

Several objectives have to be reached: we want to ensure proper spacing between images, but we also need the spring forces not to interact with the convergence to the MEP. To ensure these two conditions, we first define a unit vector tangent to the transition at the configuration R_i , $\vec{\tau}_i^{\parallel} = \frac{\vec{R}_{i+1} - \vec{R}_i}{\|\vec{R}_{i+1} - \vec{R}_i\|}$, and then decompose the different forces applied to R_i in the space $(\vec{\tau}_i^{\parallel}, \vec{\tau}_i^{\perp})$:

- Interatomic forces: $-\nabla U(R_i) = -(\nabla U(R_i) \cdot \vec{\tau}_i^{\parallel})\vec{\tau}_i^{\parallel} - (\nabla U(R_i) \cdot \vec{\tau}_i^{\perp})\vec{\tau}_i^{\perp}$
- Spring forces: $F_s(i) = (F_s(i) \cdot \vec{\tau}_i^{\perp})\vec{\tau}_i^{\perp} + (F_s(i) \cdot \vec{\tau}_i^{\parallel})\vec{\tau}_i^{\parallel}$

with $F_s = k_s(|R_{i+1} - R_i| - |R_i - R_{i-1}|)$.

Finally, we reduce the inter-atomic forces to their orthogonal $(\vec{\tau}_i^{\perp})$ component only and the NEB spring forces to their parallel component one $(\vec{\tau}_i^{\parallel})$, giving rise to the total NEB force:

Nudged Elastic Band forces

$$F_{NEB} = -(\nabla U(R_i) \cdot \vec{\tau}_i^{\perp})\vec{\tau}_i^{\perp} + F_s \vec{\tau}_i^{\parallel} \quad (3.2.1)$$

$$= -\nabla U(R_i) + \left[\nabla U(R_i) \cdot \vec{\tau}_i^{\parallel} + F_s \cdot \vec{\tau}_i^{\parallel} \right] \vec{\tau}_i^{\parallel} \quad (3.2.2)$$

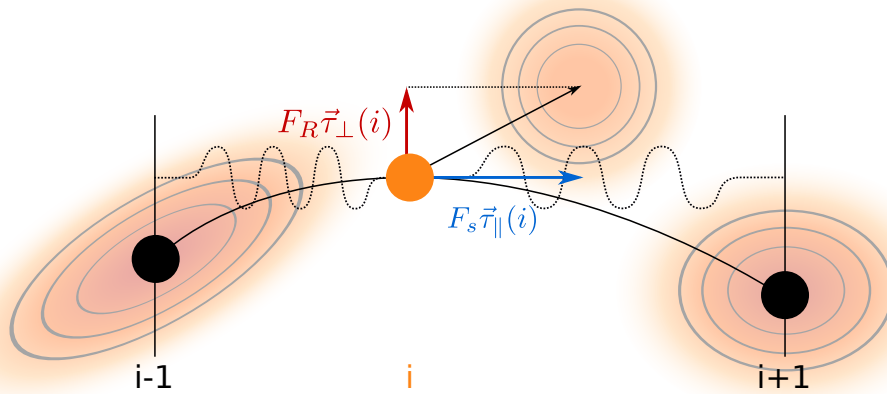


Figure 3.1. Description of the NEB convergence to the MEP.

A description of NEB forces is presented in Figure 3.1. The latter force can then be minimized through gradient descent or other optimizing schemes. As the NEB relies on different images

that are optimized through energy minimization under the constrained that are imposed by the presence of the springs, the corresponding barrier is an energy barrier at T=0K.

Although fast and easy to apply, this method is very likely to miss the saddle point due to the inherent discretized transition path with spaced steps. One possible solution has been suggested with the so-called Climbing Image NEB. After several NEB iterations, the image of the highest energy is driven toward the saddle point as:

$$F_{CI-NEB} = -\nabla U(R_i) + 2\nabla U(R_i) \cdot \frac{\vec{\tau}_i \|\vec{\tau}_i\|}{\|\vec{\tau}_i\|^2} \quad (3.2.3)$$

Doing so, one of the images climbs up the energy surface along the reaction path while minimizing the inter-atomic forces. Finally, one can notice that the NEB spring forces do not act, inducing a non-uniform configuration spacing. Although uneven, one can take advantage of the latter property to better sample the saddle point using variable spring forces constant k_i 's along the path.

3.3 Free energy sampling with Metadynamics

In order to accurately describe a phase transition, a free-energy sampling is required. Indeed, while NEB calculations allow in some cases to have a simple idea of the different stages it completely neglects thermal and quantum effects, and is limited by its inherent sequential description accounting only for internal energy, and does not give access to a full picture of the energy landscape. Therefore, we go beyond the NEB approach towards a free energy sampling, which in the canonical ensemble ($F(N, V, T)$), is described by the Helmholtz free energy:

$$F = -k_b T \log(\mathcal{Z}) \quad (3.3.1)$$

Where \mathcal{Z} is the partition function classically described as:

$$\mathcal{Z} = \frac{1}{N! h^{3N}} \int d^3 x_1 \dots d^3 x_N d^3 p_1 \dots d^3 p_N e^{-\beta H(x_1, \dots, x_N, p_1, \dots, p_N)} \quad (3.3.2)$$

where N is the number of particle, x_i and p_i the respective position and momenta of the particle i , and H the hamiltonian of the system.

While describing transitions, the reaction coordinate is often unknown as it can involve several mechanisms. In this context, and based on the relevant known characteristic of the transition, the choice of an order parameter χ to describe the reaction coordinate can be a fair approximation:

$$\chi(x_1, \dots, x_N, p_1, \dots, p_N) \quad (3.3.3)$$

The latter can be either atomic distances, angles or any relevant quantity describing the reaction. So defined, the probability of being at χ_0 along the free energy profile defined by this order parameter is given by:

$$P(\chi_0) = \frac{1}{\mathcal{Z}} \int d^3 x_1 \dots d^3 x_N d^3 p_1 \dots d^3 p_N e^{-\beta H(x_1, \dots, x_N, p_1, \dots, p_N)} \delta(\chi(x_1, \dots, x_N, p_1, \dots, p_N) - \chi_0) \quad (3.3.4)$$

where δ is the Dirac delta function

Doing so, we end up with an integral over the full phase space that cannot be reached in our simulations. We thus have to use approximations to overcome this issue. First, we assume that we do not need a complete picture of the phase space to describe the transition, and secondly that our simulation is sufficiently long, or with sufficient initial conditions to verify the ergodicity property.

In this context, the probability $P(\chi_0)$ is given by:

$$P(\chi_0) = \frac{1}{t} \int_0^t \delta(\chi(x_1, \dots, x_N, t') - \chi_0) dt' \quad (3.3.5)$$

And the free energy at this point is given by:

$$F(\chi_0) = -k_b T \log(P(\chi_0)) \delta(\chi(x_1, \dots, x_N, p_1, \dots, p_N) - \chi_0) \quad (3.3.6)$$

Then, under the defined approximations, we can extract a free energy profile from state I to state F along any order parameters χ from our MD simulations. However, for this to work and to obtain reliable free energies, the MD trajectories need to sample both states properly. While dealing with rare events and high barriers this condition is not always reachable due to either

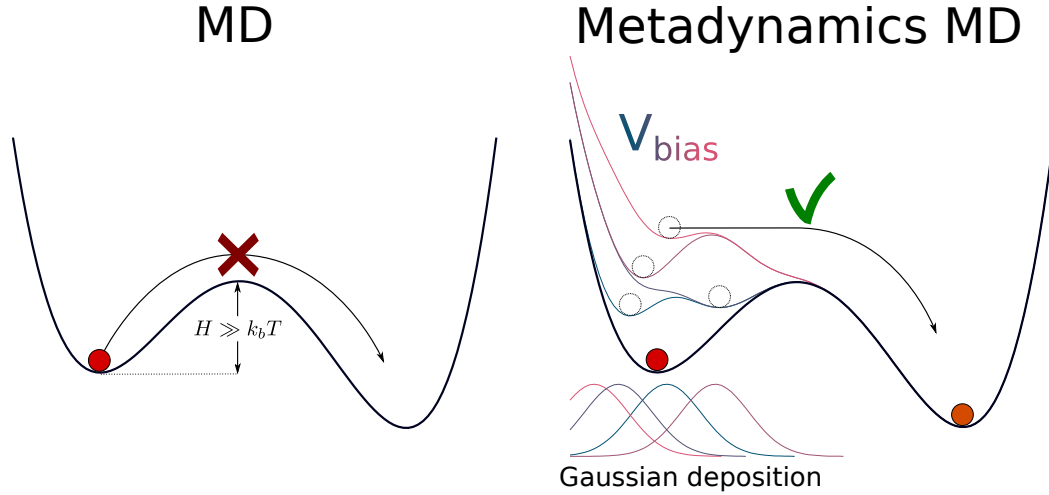


Figure 3.2. Description of the MTD approach to accelerate rare events and sample the free energy landscape.

non-sufficient thermal and quantum energies or the computational cost of ab initio simulations. Therefore, to address this issue, Laio and Parrinello introduced in 2002 a new method, the MTD,³⁰ to accelerate rare events and escape from a potential well and therefore accelerate the free energy landscape sampling. The idea behind MTD is the following: we want to force the system to explore a broader region than that around a local minimum of the collective variable χ , by penalizing the already explored ones. To this purpose, we add a local bias potential $V(\chi)$ to the free energy along the coordinate χ during the MD simulation^a.

This approach is formalized as follows:

First, we define a Collective Variable (CV)s $S = \{S^1, \dots, S^D\}$ as a set of D reaction coordinates, or order parameters, which can describe the related transition or reaction process collectively. This CV depends on the $3N$ coordinates of the system and at time t with configuration $\{x_1(t), \dots, x_N(t)\}$ will take the value $s = \{s^1, \dots, s^D\} = s(t)$.

Then, we define a history bias potential V_{bias} which will evolve with time and always be added to the free energy. At $t = 0$ $V_{bias} = 0$.

At another time t' , we add to the history bias potential a Gaussian potential $h_0 e^{-\frac{(S-s)^2}{2\sigma^2}}$ centered at $s(t')$ with a free energy height h_0 and a width of σ , all of these parameters being a set of D variables.

We then repeat the process at the time t'' , the difference $t'' - t'$ defines the bias period deposition τ . Doing so, at a certain time t , N Gaussian potential have been added to the history bias potential each period τ leading to the following history potential:

$$V_{bias}(t) = h_0 \sum_{t'=\tau, 2\tau, \dots, N\tau} e^{-\frac{(S-s(t'))^2}{2\sigma^2}} \quad (3.3.7)$$

This allows penalizing already explored space, or previous configurations, and fill the potential well allowing the system to explore other parts of the free energy landscape along the CV, as described in Figure 3.2. Then, for a sufficiently long time, the system should have explored the latter completely, and the history bias potential should have filled the different potential wells. Therefore, the sum of the different deposited Gaussians can be seen as a mold of the free energy

^aThis approach is also shared by other methods such as umbrella sampling which we will not discuss here.

landscape, leading to the following approximation of the free energy along S :

$$F(S) = \lim_{t \rightarrow \infty} -V(t) \quad (3.3.8)$$

In practice, the convergence is attained when the free energy differences between the distinct basins is not anymore modified when adding more gaussians.

MTD is, therefore, useful to accelerate rare events and obtain an approximate free energy landscape. In contrast with the NEB approach, it gives rise to a broader picture and finer description of the transition mechanism. In addition, through its molecular dynamics approach, we can have access to free energy accounting to both thermal effects when coupled to a thermostat and also to nuclear quantum effects. In particular, in the PI framework where we already defined the free energy as:

$$F = -k_b T \log(\mathcal{Z}) \quad (3.3.9)$$

$$= -k_b T \log(\text{Tr}(\rho_{eq})) \quad (3.3.10)$$

However, several parameters need to be tuned. The height and width of the Gaussian bias potential need to be carefully chosen considering the related process. To do so, a first NEB approach can give a bare idea of the barrier height potential to be reached. In parallel, a too high frequency of gaussian deposition needs to be avoided to let the system explore the potential, and a good balance between the latter parameter and the Gaussian free energy height is required. Overall, the most important parameter is the choice of CV.

3.3.1 Path collective variables and the path invariant vector

While studying phase transitions, the set of order parameters needs to catch the different physical properties involved in the latter thoroughly. This makes the choice of the CV complex and somehow imposes a particular view of the transition. In this context, several developments of Path CVs were done to address this issue.³¹ The idea behind this Path CVs is the following: assuming we have an hypothetical set of n path configurations from the initial R_i to the final R_n we define the Path CVs $S(t)$ and $z(t)$ as:

Path collective variables

$$S(t) = \frac{\sum_{k=1}^n k e^{-\lambda D(R(t), R_k)}}{\sum_{k'=1}^n e^{-\lambda D(R(t), R_{k'})}} \quad (3.3.11)$$

$$z(t) = -\frac{1}{\lambda} \log \left(\sum_{k=1}^n e^{-\lambda D(R(t), R_k)} \right) \quad (3.3.12)$$

With $R(t)$ the configuration coordinates at time t , λ a tunable parameter and D the chosen metric between $R(t)$ and $R_{k,k'}$

The first variable $S(t)$ defines the progress of the transition while the second, $z(t)$ refers to the distance of the hypothetical path. The second step is naturally the definition of the chosen metric. Recent studies have shown the efficiency of metrics based on the path invariant vector, which we now describe. The PIV is constructed from the atom-type-specific ordered blocks $v_{kk'}$ linking the atom types k and k' , and the components of which are defined as:

$$v_{kk'}^{\beta\beta'} = c_{kk'} S \left[\left(\frac{\Omega_0}{\Omega} \right)^{\frac{1}{3}} |r_{\beta k} - r_{\beta' k'}| \right] \quad (3.3.13)$$

Where $r_{\beta k}$ defines the position of the atom β of type k , Ω the volume of the simulated box, Ω_0 a reference volume, and S a switching function which decreases from 1 to zero as $|r_{\beta k} - r_{\beta' k'}|$ increases. Then the elements of the different blocks $v_{kk'}$ are sorted in ascending order and concatenated leading to the PIV of $\frac{N_{atoms}(N_{atoms}-1)}{2}$ components V_α . Doing so, an invariance upon permutation of identical atoms arises and the metric D is then defined as the Euclidian distances between the PIVs:

$$D_{AB} = \sum_{\alpha} (V_{B\alpha} - V_{A\alpha})^2 \quad (3.3.14)$$

Thanks to this approach, the description of the transition is not governed by arbitrary order parameters such as atomic bond length angles, etc. but instead by topological similarities and differences between configurations. This is an essential improvement for phase transition descriptions that we naturally followed in our investigations, and that demonstrated its reliability in several cases, in particular, it allows reconstruction of the phase diagram of water.³²

3.4 Conclusion

In this section, we described the NEB and MTD methods to investigate phase transitions.

As we have seen, the NEB approach provides information on the MEP and saddle point of the reaction, without defining any reaction coordinate. This method has the advantage of being easy to apply and computationally efficient. However, neither thermal nor quantum effects are considered, and although this method can be reliable to find saddle points, it can drive to incorrect MEP.

On the other hand, the MTD method provides a broader complete picture of transitions as it forces the system to explore the free energy landscape. The counterpart is the choice of the CV. Indeed, if the latter is not suitable for the studied transition, it can lead to an incorrect representation. To address this issue, we presented the Path CVs complete by the PIV topological metric to avoid any arbitrary choice of the CV.

Therefore, to provide information of the transition we present in the following, we used the NEB method as a first approach to have an approximate idea of the transition path and barrier of reaction in order to parametrize the MTD simulations, as a second step.

Part II

Investigation of Nuclear Quantum Effects

1	Quantum driven proton diffusion in brucite minerals	57
1.1	Introduction	57
1.2	Brucite mineral structure	58
1.3	Proton diffusion mechanism	58
1.3.1	In plane reorientation	59
1.3.2	Out of plane dissociation	60
1.3.3	Proton diffusion sweet spot	63
1.4	Comparison with Portlandite	65
1.5	Conclusion	67
2	Methane hydrate: towards a quantum-induced phase transition	69
2.1	Introduction	69
2.1.1	MH-III structure	70
2.2	MH-III under pressure	73
2.2.1	Spectral analysis	73
2.2.2	Methane ordering and locking-in	75
2.2.3	Methane-Water interaction	77
2.3	The methane hydrate IIIs	81
2.3.1	From MH-III to MH-IIIs	82
2.3.2	Nuclear quantum effects and isotopic substitution	83
2.4	The methane hydrate IV	90
2.4.1	Structural properties	91
2.4.2	Hydrogen bond symmetrization: MH-IVs	93
2.4.3	Vibrational properties	95
2.5	Transition description	97
2.5.1	Transition stages	97
2.5.2	Stability of the ice frame	98
2.5.3	Transition path	100
2.6	Conclusion	103
3	The Quantum equilibrium structure of sodium hydroxide	105
3.1	Introduction	105
3.2	Sodium hydroxide structure	106
3.3	Quantum mechanical description of structural properties	106
3.4	Towards a dynamical paraelectric state	109
3.5	From temperature- to pressure-induced transition	112
3.6	Conclusion	114

Quantum driven proton diffusion in brucite minerals

1.1 Introduction

Diffusion is among the most complex theoretical problems in solid state physics and materials science. Hydrogen diffusion, in particular, constitutes a significant challenge, for many reasons. Firstly, Hydrogen is the most abundant element in the Universe. Hydrogen atoms are amphoteric and can be incorporated almost in any mineral or material, forming stable bonds with cations and anions. When bound to O to form hydroxyl groups, the high O-H stretching frequency implies non-negligible zero-point energy of about 0.2 eV that could be crucial when hopping through local sites which are separated by barriers that classical nuclei cannot overcome simply by thermal fluctuations.^{1,33,4} Despite the complexity and computational cost of accounting for the quantum nature of light nuclei in simulations, a new field is rapidly growing with potential applications in an eclectic collection of issues including protonic conduction,³⁴ hydrogen in biological matter,³⁵ water circulation in Earth's mantle,^{5,36} or hydrogen storage.^{37,38}

All of the previous phenomena are deeply affected by proton diffusion, which is difficult to probe directly from proton quantum trajectories, although crucial for the determination of thermodynamic properties, such as proton conduction or isotope exchange. While Portlandite is of interest for industrial applications as the main component of concretes, Brucite is considered a vector for water transport into Earth's mantle that proton diffusion could trigger.

Therefore, we address the proton diffusion process occurring in Brucite $\text{Mg}(\text{OH})_2$ that appears to be a particular case among the different minerals of this class, as compared with Portlandite $\text{Ca}(\text{OH})_2$, which is also discussed. Quite a number of proton diffusion mechanisms were considered in the past: we show that the so-called "relay" mechanism,³⁹ a two-step process in which the proton hops from one oxygen atom to another and rotate with a hydrogen-containing group, is at work in $\text{Mg}(\text{OH})_2$ under high pressure. We also show in the following that at least the first step (H hopping through hydrogen bonds) is quantum driven.

Technical details of the simulations employed for this analysis can be found in the Appendix A.

1.2 Brucite mineral structure

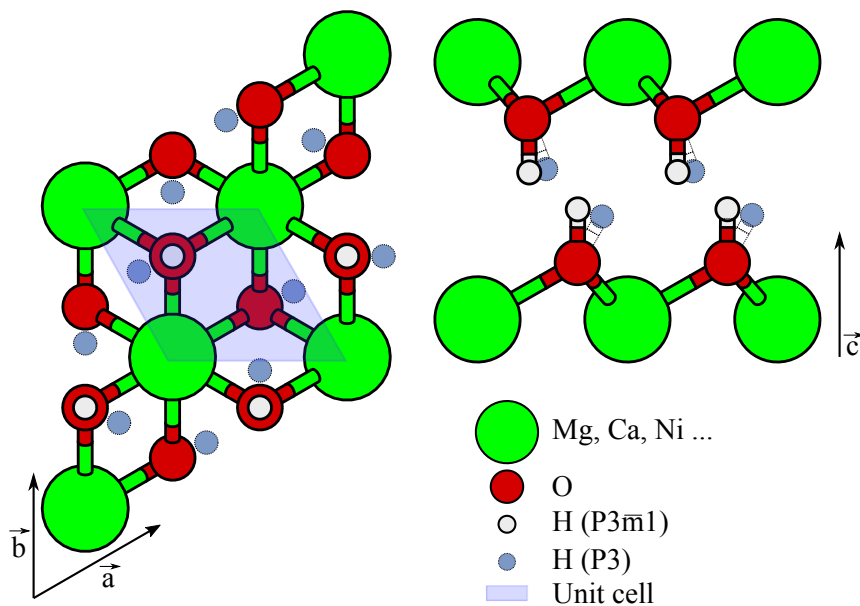


Figure 1.1. Description of Brucite minerals structure. The hydrogen atoms labeled $P_{3\bar{m}1}$ (light grey) are in the 2d Wyckoff sites, while the P_3 hydrogen atoms (dark grey) are in the disordered 6i Wyckoff sites. The latter is the stable structure at the pressures of our simulations.

The Brucite minerals are layered structures composed by stacks of metallic ions, oxygen, and hydrogen atoms in a CaI_2^- type structure. The metallic element (Mg, Ca, Ni ...) has an impact on several physical parameters, in particular, the lattice parameters and the compressibility of the system are different in the two systems we studied: Brucite ($Mg(OH)_2$) and Portlandite ($Ca(OH)_2$).⁴⁰

At ambient pressure and temperature, the Brucite minerals belong to the $P_{3\bar{m}1}$ space group with hydrogen atoms located on the threefold axis above or below oxygen atoms (2d Wyckoff sites) with a $\frac{1}{2}$ occupancy factor as shown in Figure 1.1. However, in accordance with previous experimental and simulation results,^{41,42,43,44,45} as pressure is slightly increased, due to the increase of the H-H repulsive interaction between opposite layers, we find that the hydrogen nuclei do not remain strictly above the corresponding oxygen atom and the Brucite minerals adopt a P_3 configuration. The latter is characterized by the location of hydrogen atoms in the 6i Wyckoff sites with a $\frac{1}{3}$ occupancy factor. This effect has been shown to induce a frustration of the proton orientation upon compression.^{46,47,41}

The stability of both Brucite and Portlandite upon compression have been investigated in the past and an amorphization of Portlandite was found to occur between 10 and 15GPa⁴⁶ while a phase transition to a tetragonal structure was suggested in Brucite above 20GPa at 800K by ab-initio simulations,⁴⁸ however up to now, no such transition was observed experimentally to our knowledge.^{47,49}

1.3 Proton diffusion mechanism

In a recent study⁵⁰ a proton diffusion process scheme was proposed for the case of Brucite minerals. This process requires two mechanisms to be present: a proton reorientation in the (a,b) plane, and a proton dissociation out of that plane. Indeed, if a diffusion process, that is, non-spatially limited motion of the protons from site to site, is to occur, both mechanisms must

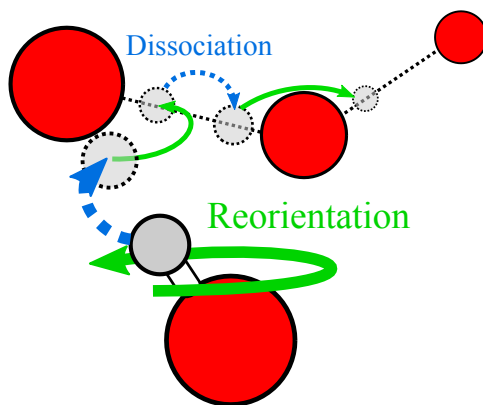


Figure 1.2. Proton hopping mechanisms, reorientation, and dissociation; diffusion requires both. Oxygen atoms are colored in red, hydrogen atoms in grey.

be present. Dissociation is necessary as it allows hopping from one oxygen atom to another, but if no reorientation happens, the proton will only be able to return to its original position: reorientation enables the proton to move on to another O-O segment and thus to hop to yet another oxygen atom (Figure 1.2). Proton diffusion in Brucite minerals is, therefore, a two-step compound process, different from a standard Grotthuss mechanism.^{51,39}

In practice, the above mentioned P3 configuration generates an effective triple-well potential for reorientations within the (a,b) plane: this we refer to as “in-plane” motion. The proton dynamics on these sites describes the reorientation motion. On the other hand, the “out of plane” dissociation mechanism involves an effective double well potential along the O-O direction characterizing the covalent and hydrogen bonds similar to the ice case.¹ It has been shown⁴² that only weak hydrogen bonds could be present in Brucite. However, as we will discuss later, taking into account nuclear quantum effects, a double-well potential is found along the O-O direction at low pressure suggesting the H-bond interaction, which can be enhanced by the pressure-induced creation of a quasi-2D hydrogen layer in the structure.

Finally, the thermal activation of the reorientation motion was assumed⁵⁰ to be a limiting factor for diffusion, while nuclear quantum effects are suggested as being a facilitating factor for the dissociation mechanism. However, proton dissociation has not been observed yet and nuclear quantum effects for the latter mechanisms have been neglected up to now.

Therefore, in the following, we undertake to unravel the complex and quantum driven proton diffusion mechanisms in Brucites by including NQE: first, we will discuss both the reorientation and dissociation mechanism upon compression, for which we will compare thermal and quantum effects. In the second part, we will address the evolution of the diffusion process upon compression. Finally, a comparison with Portlandite will be provided.

1.3.1 In plane reorientation

First, we discuss in this part the reorientation mechanism. As already described, within the P₃ structure, protons move in-plane between the 6i sites. Therefore, this motion can be effectively described by the azimuthal angle φ , as shown in the sketch of Figure 1.3. From the probability distribution of the latter $\mathcal{P}_r(\varphi)$, we extracted the Gibbs free-energy profile $G = -k_B T \log \mathcal{P}_r(\varphi)$, which includes both thermal and quantum effects.

As shown in Figure 1.3, the proton effective potential along this coordinate has a three-fold $\frac{2\pi}{3}$ symmetry with equivalent barrier heights between the three wells, as expected from the symmetry of the P₃ configuration.

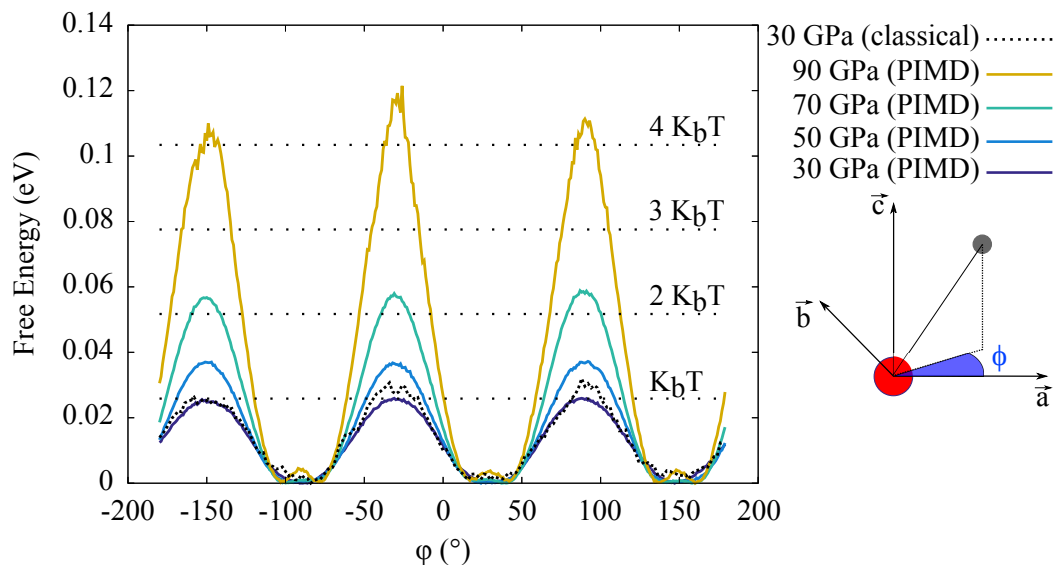


Figure 1.3. Free energy profile along the coordinate ϕ . Comparison between classical and PIMD simulations at 30GPa shows that the reorientation mechanism is dominated by thermal effects.

The barrier width between the wells of this potential is essentially proportional to $\frac{2\pi}{3}d_{\text{O-H}}\cos\theta$, θ being the zenith polar angle, that is, how far the O-H bond slants away from the c axis; $d_{\text{O-H}}$ being the covalent O-H bond distance.

Upon compression, we observe that the free energy barrier heights increase, from 20meV at 30GPa up to 100meV at 90GPa, revealing a pressure induced confinement of the proton along this coordinate. This stems essentially from the fact that the average polar angle θ increases with pressure so that the separation of the wells also increases. Thus, as the overall atom-atom separations decrease, mainly through the compression of the layers along the \vec{c} axis, the H-H repulsive interaction increases and the reorientational dynamical disorder, thermally activated at low pressure, tends to slow down, eventually to halt. It can be noted that the classical simulations, not including NQE, yield almost identical distributions meaning that the quantum behavior is in this case limited within the pressure range that was explored.

The effect of pressure contrasts with that of temperature, which tends to allow the proton to explore equivalently all the wells⁵⁰ by usual thermal activation.

1.3.2 Out of plane dissociation

In this section, we now focus on the out of plane dissociation by proton hopping between the two oxygen layers. Upon compression, the hydrogen planes get closer, due to the important compressibility of the system along the \vec{c} axis. This, in turn, can favor proton hopping from one oxygen atom to another, that is dissociation and thus out-of-plane delocalization.

• Quantum quasi 2D hydrogen plane

Figure 1.4 shows the probability distribution of the hydrogen nuclei along the c direction. Initially, each hydrogen atom belongs to either the upper or lower plane. During the simulation, the “lower layer” distribution refers to the hydrogen atom initially in the lower layer while the “upper layer” refers to those initially in the upper layer. We distinguish both the upper and lower hydrogen layers distributions from the overall one. As pressure is increased, the overall distribution width decreases as the two hydrogen layers distributions get closer, meaning that the pressure tends to merge the two hydrogen layers. At the two lower pressures, 30 and

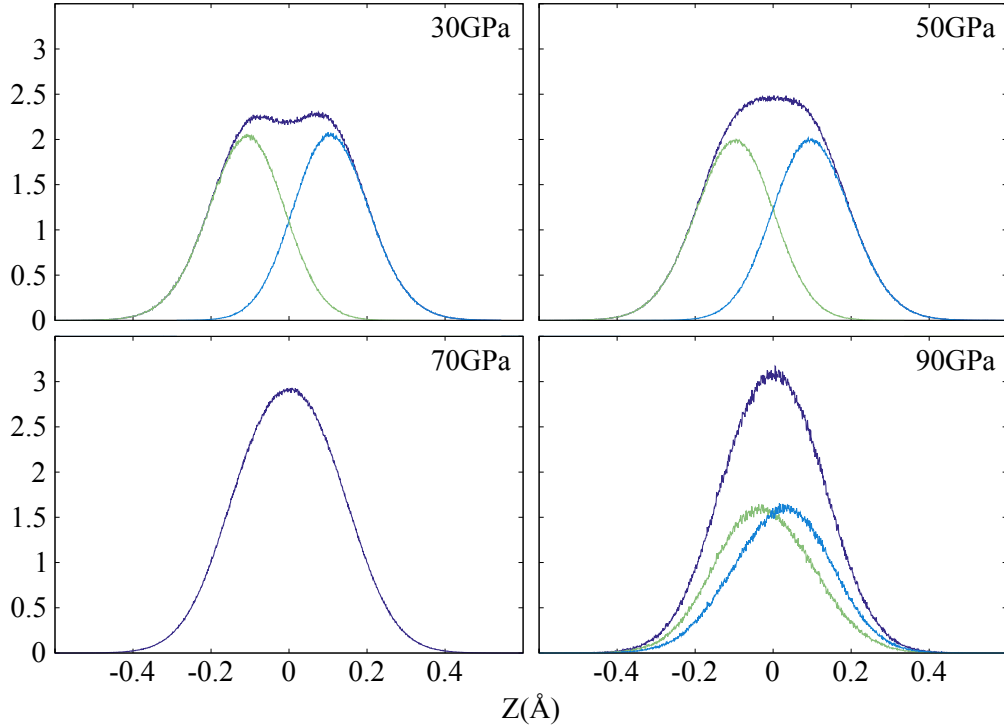


Figure 1.4. Probability distribution of the proton position along \vec{z} . The green lines relate to the bottom layer of hydrogen nuclei (Figure 1.1), the blue lines to the top layer, while the purple lines are the sum of both.

50GPa, bottom and top layer protons can be distinguished, although hopping does occur, as the protons return to their original layer by a second hop in reverse: the protons initially situated on one layer will remain on that layer with, from time to time, a short exploration of the other. At 70GPa, lower and upper layers are not distinguishable as reverse hopping does not always follow: the protons do not belong to one particular layer. This specific case will be discussed later. At the highest pressure, 90GPa, the overall distribution becomes narrower, but the lower and upper protons can again be distinguished as they return to their initial layer, despite a significant distribution overlap.

The characterization of the two hydrogen layers is however highly dependent on the quantum spread of protons. Indeed, for a delocalization of the same order of magnitude as the separation between the two layers, one cannot distinguish upper from lower layer due to quantum indetermination. In this context, the RPMD simulations account for NQE by representing each particle by a set of replicas (or beads), thus, the spread of these replicas provides insight into the quantum delocalization of the particles. Therefore, we investigated the standard deviation, in each cartesian coordinate, of the proton replicas with respect to the instantaneous centroid position. As shown in Figure 1.5 the in-plane delocalization σ_a and σ_b of the particle along the \vec{a} and \vec{b} axes are similar and both decrease upon compression. In contrast, the out-of-plane delocalization along the \vec{c} axis, described by σ_c is less than in the two other directions but increases upon compression. Finally, at high pressure (90GPa) the delocalization σ_z is of the order of the distance between the two hydrogen layers. This indicates that the two hydrogen planes merge through quantum indetermination into a so-called “Quantum 2D proton layer”. Such configuration allows the protons to form covalent bonds either with the upper or lower oxygen layer, thus easing the proton hopping.

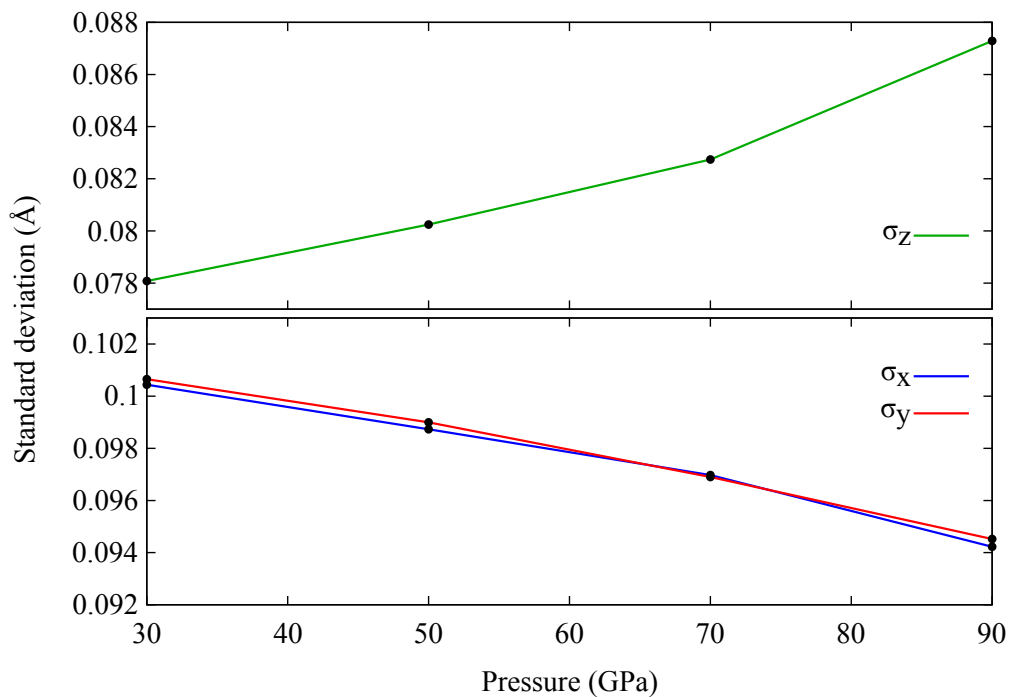


Figure 1.5. Standard deviations of the ring polymer beads positions with respect to the centroid.

• Proton dissociation

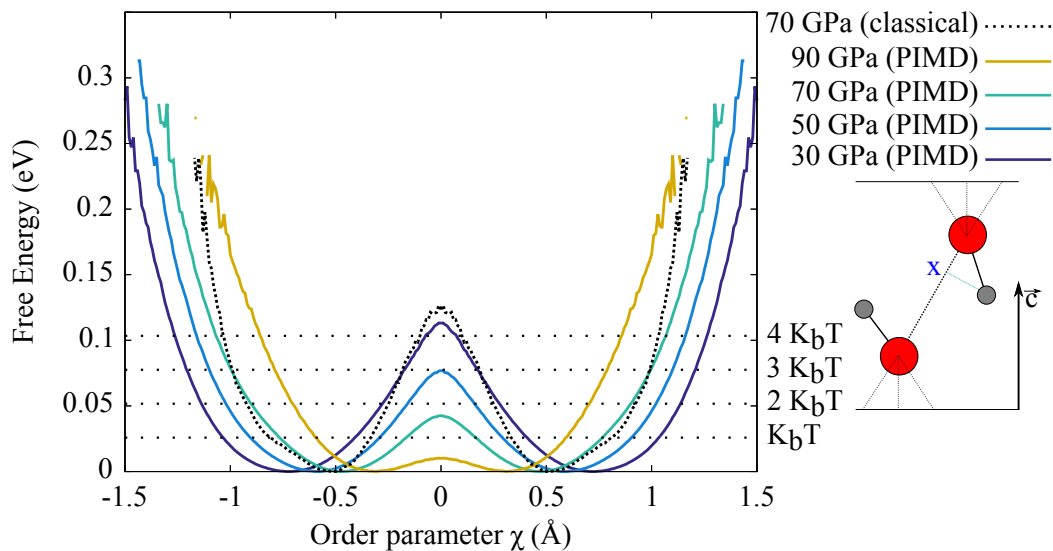


Figure 1.6. Proton free energy profile along the coordinate χ .

In addition to the formation of the single proton layer, with increasing pressure, the in-plane localization produces quasi-linear O-H-O groups through the H bond formation. This results in an effective double-well potential along the O-O direction as seen by the protons. In order to investigate this effective potential, one relevant order parameter χ is the difference between the distances that separate the hydrogen atoms from their nearest and second nearest neighbor

oxygen atoms projected on the O-O direction (see the sketch in Figure 1.6).

$$\chi = (d_{O,2-H} - d_{O,1-H}) \cdot \vec{u}_{OO} \quad (1.3.1)$$

with \vec{u}_{OO} the unitary vector in the O-O direction.

The free energy profiles along this coordinate presented in Figure 1.6 show that the proton hopping barrier height decreases upon compression, from $4k_B T$ at 30 GPa to $0.5k_B T$ at 90 GPa. This occurs while the O-O distance shrinks with pressure along the \vec{c} axis bringing the two equilibrium positions closer along χ . Under high pressure, a proton can, therefore, hop from one oxygen atom to another through either quantum tunneling or thermal activation, which constitutes the so-called “dissociation” process.⁵⁰ The difference between classical and quantum simulations is significant as it was evaluated to $\sim 3k_B T$ on this barrier. Therefore, although the proton reorientation mechanism is thermally activated, the dissociation process is mainly quantum driven.

1.3.3 Proton diffusion sweet spot

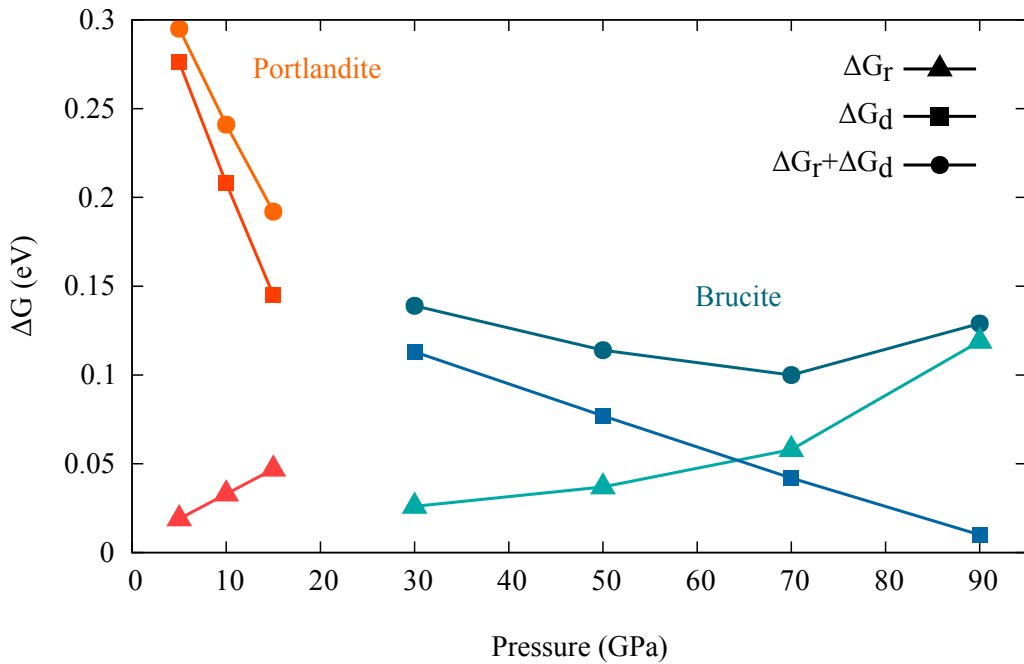


Figure 1.7. Free energy barriers evolution upon compression for Brucite and Portlandite.

The effect of the pressure on the proton reorientation mechanism is opposed to the effect on the dissociation one. However, as described earlier, the proton diffusion in Brucite minerals requires both. Therefore, due to competition between pressure effects, a pressure sweet spot exists, allowing both reorientation and dissociation mechanisms, enhancing the proton diffusion in Brucite minerals. Thus, we studied the maximum probability of diffusion, considering both the reorientation and the dissociation mechanism to be independent. This approximation was checked by calculating the correlation between the two probabilities. Under this assumption, the maximum diffusion probability is given by the product of the reorientation and dissociation maximum probabilities P_r and P_d which reduces to the sum of the two barrier heights, ΔG_r and

ΔG_d , in terms of free energy.

$$P = P_r \times P_d \quad (1.3.2)$$

$$\Delta G = -k_b T \log(P_r \times P_d) \quad (1.3.3)$$

$$= \Delta G_r + \Delta G_d \quad (1.3.4)$$

The evolution of the free energy barrier heights upon compression is given in Figure 1.7. For the case of Brucite, we observe that the barrier height for dissociation decreases from ~ 0.11 eV at 30GPa to ~ 0.01 eV at 90GPa. In contrast, the reorientation barrier increases from 0.03 eV to 0.1 eV within the same pressure range. Thus, the two curves cross at ~ 70 GPa, giving rise to a minimum of diffusion free energy barrier ΔG . Hopping rates for the two processes have the same order of magnitude at this pressure, while reorientation dominates at lower pressures and dissociation does so at higher pressures. Therefore, 70GPa represents the sweet spot for a maximum diffusion probability.

In order to give a rough estimate of the diffusion reaction rate κ , one can use the diffusion free energy barrier obtained above in the chemical kinetics Eyring-Polanyi equation:

$$\kappa = \frac{k_B T}{h} e^{-\frac{\Delta G}{k_B T}} \quad (1.3.5)$$

As shown in Table 1, the estimation of this reaction rate in Brucite naturally follows the same trend as the free energy evolution upon compression. It decreases by a factor of four between 30 and 70GPa, for which the characteristic time evaluation is $\kappa^{-1} = 8$ ps, and then increases by a factor of three at 90GPa.

		Brucite Mg(OH) ₂				Portlandite Ca(OH) ₂		
P	(GPa)	30	50	70	90	5	10	15
κ	(THz)	0.029	0.076	0.131	0.043	$6.7 \cdot 10^{-5}$	$5.6 \cdot 10^{-4}$	$3.7 \cdot 10^{-3}$
κ^{-1}	(ps)	35	13	8	23	14300	1775	267
						Transition		

Table 1. Eyring-Polanyi reaction rate κ and inverse, computed for Brucite (left) and Portlandite (right). The transition pressure for Portlandite is reported in refs. [52, 53].

• In-plane proton distribution

The barrier height analysis above is confirmed by Figure 1.8 which shows the probability distribution of the proton positions in the (a,b) plane. For $P = 30$ GPa, the situation is as expected: the proton distribution shows three broad peaks next to each oxygen atom, thus revealing reorientation processes between the 6i sites. As pressure is increased to 50GPa, the peaks become narrower and at a greater distance from the oxygen sites, therefore displaying the hindering of the reorientations and the flattening of the O-H bonds within the (a,b) plane. In addition, the density midway between oxygen atoms increases as the dissociations become easier. At $P = 70$ GPa, we observe evidence of proton diffusion process as the hydrogen nuclei spread beyond the simulation box. The onset of dissociation, while reorientations still occur, allows the protons to migrate beyond their immediate vicinity. Finally, at the highest pressure, $P = 90$ GPa, although dissociations are important, the reorientations are locked in prohibiting proton diffusion. This confirms the particularity of the pressure of 70GPa as being a sweet spot for proton diffusion.

It has to be noticed that in order to observe such a diffusion process, the simulation duration requires to be higher than the estimation of κ^{-1} . Therefore, the proton diffusion described in this paper should occur at lower pressure and can be at the root of destabilization of the system

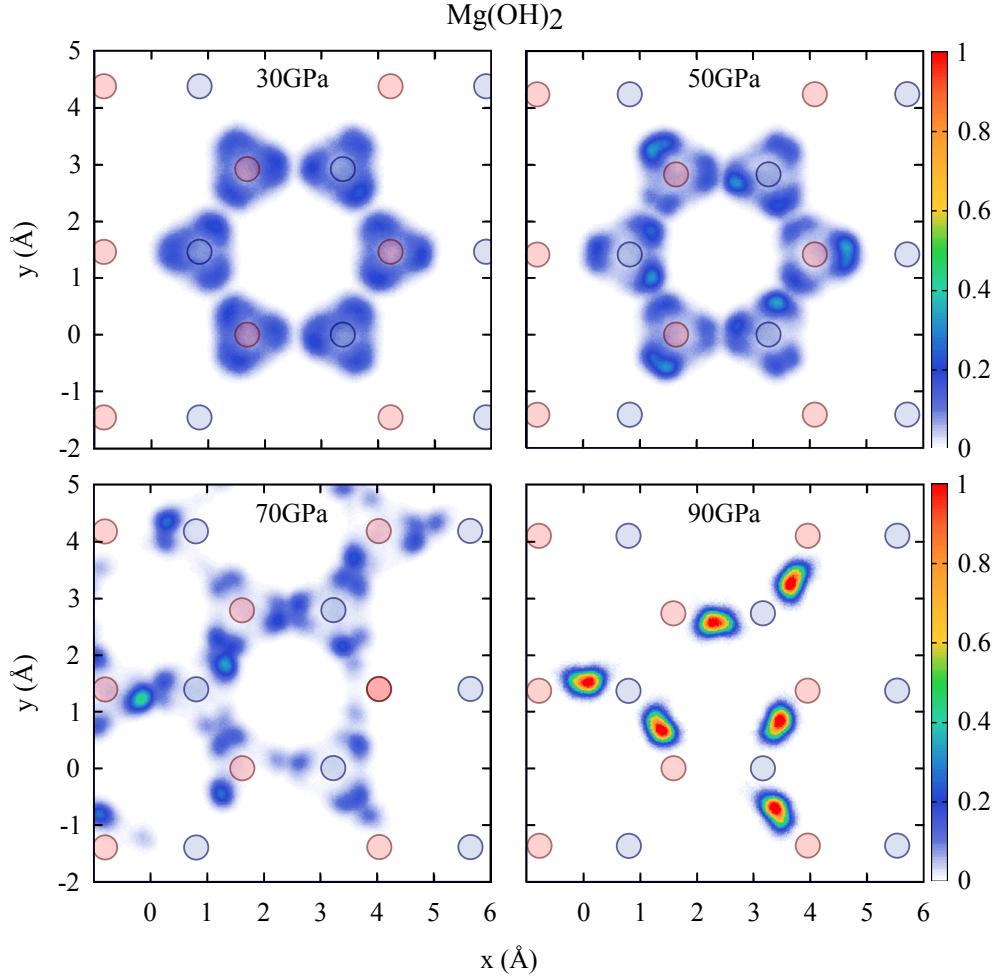


Figure 1.8. Probability distribution of the proton positions in the (a, b) plane at 30, 50, 70 and 90 GPa for Brucite $\text{Mg}(\text{OH})_2$. The circles represent the projection of the oxygen sites on the (a, b) plane (light red: bottom layer, light blue: top layer). Periodic boundary conditions are not used in computing this distribution in order to visualize the displacement of the protons.

easing suggested phase transition, or could bring information concerning the water transfer in the earth mantle.

1.4 Comparison with Portlandite

Finally, we close our discussion of proton diffusion in Brucite minerals by a comparison with Portlandite ($\text{Ca}(\text{OH})_2$) which presents the same structure for pressures up to approximately 15 GPa. The same analysis as for the Brucite was done systematically for Portlandite. In Figure 1.7, we present the evolution of free energy barriers of the proton reorientation and dissociation mechanisms. We observe that in Portlandite the reorientational barrier at 10 GPa is close to that of Brucite at 50 GPa. However, the pressure effect on the latter barrier is more important in Portlandite as shown by the larger increase rate of 2.8 meV/GPa while it is evaluated to be 1.6 meV/GPa in Brucite. This rapid increase can be understood from the fact that the Van der Waals radius of calcium atoms is larger than for magnesium and thus tends to expand the lattice in the (a, b) plane. Indeed, our calculations at 10 GPa give the in-plane first neighbor O-O distances to be $\sim 3.45 \text{ \AA}$ in Portlandite while $\sim 3.06 \text{ \AA}$ in Brucite. In addition, the out-of-plane

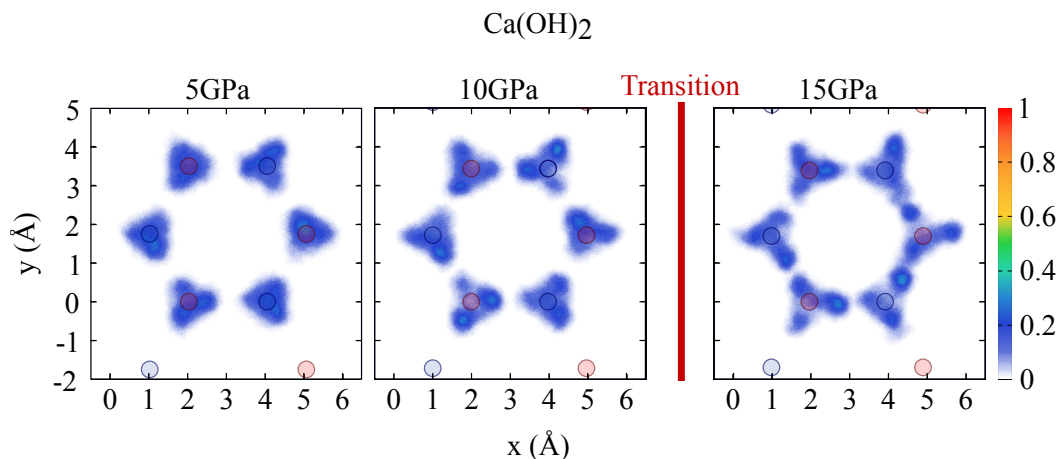


Figure 1.9. Probability distribution of the proton positions in the (a,b) plane at 5, 10 and 15GPa for Portlandite $\text{Ca}(\text{OH})_2$.

first neighbor O-O distances are equivalent in both systems. This implies larger polar angles θ in Portlandite, that efficiently hinder the reorientation mechanism, including at relatively low pressures. On the other hand, the dissociation barriers in Portlandite are greater than in Brucite but decrease much faster with a decay of 14 meV/GPa as compared to 2meV/GPa in Brucite. This derives from the larger compressibility of the Portlandite with respect to the Brucite structure, as demonstrated in recent work.⁴⁰ It has to be noticed that the large value of the dissociation barrier in Portlandite implies a long simulation duration in order to be observed, well beyond the scope of path integral methods, to address properly the statistic of the latter, and thus barrier height evaluation. Nevertheless, some events are detected as some of the replicas of the RPMD simulations do occasionally reach the top giving rise to estimation provided here. Finally, the crossing point of the two barriers in Portlandite should occur beyond 20GPa with a diffusion barrier comparable to that of Brucite at 70GPa. However, a transition towards an amorphous phase is reported between 10 and 15GPa^{52,53} and our own simulations reveal the instability of the system at 20GPa. Therefore, as shown in Figure 1.9, no diffusion was observed for Portlandite within the time scale of our simulations. Indeed, the reaction rate estimates, given in Table 1, yield much longer times than in Brucite.

This comparison suggests that Brucite could be a particular case for proton diffusion within its mineral family. Among the other systems sharing the same structure, our first analysis of Theophrastite ($\text{Ni}(\text{OH})_2$) indicates that this system should present the same mechanism at approximately the same pressure, due to comparable Van der Waals radii between magnesium and nickel atoms.

1.5 Conclusion

To summarize, we analyzed the proton diffusion mechanism⁵⁰ in both Brucite ($\text{Mg}(\text{OH})_2$) and Portlandite ($\text{Ca}(\text{OH})_2$) under pressure, taking into account nuclear quantum effects. Proton diffusion in those crystals involves two stages to be active: a reorientation motion within the (a,b) plane, and a proton dissociation between two oxygen atoms on opposite layers. Firstly, we have seen that the reorientation mechanism is thermally activated and that the pressure tends to localize the proton in a certain orientation, making reorientation motion less likely. Secondly, in contrast with the reorientation, we showed that the dissociation mechanism was quantum driven and was made easier by increasing pressure through the formation of a quantum quasi-2D hydrogen layer.

These two antagonistic effects give rise to a pressure sweet spot for proton diffusion through those minerals, found to be 70GPa in Brucite. However, this diffusion process could also occur at much lower pressure, although it is less probable, and could be at the root of destabilization of the structure, as suggested by a possible phase transition⁴⁸ at 20GPa or decomposition into MgO and H_2O at 30GPa.⁴⁹ Beyond this pressure threshold, the reorientation becomes a bottleneck for proton diffusion, while dissociation is the rate-limiting step at lower pressure.

Finally, by systematic comparison with Portlandite, we demonstrate the specificity of Brucite for proton diffusion. Indeed, the proton diffusion barrier minimum in Portlandite occurs at pressures well beyond its transition towards an amorphous phase.

Methane hydrate: towards a quantum-induced phase transition

2.1 Introduction

Gas hydrates are inclusion compounds, in crystalline clathrate structures composed of a hydrogen-bonded water network forming polyhedral cavities wherein small non-polar gas molecules are confined.^{54,55,56} They spontaneously form in Nature with several guest molecules such as carbon dioxide, hydrogen, nitrogen, and methane. However, the kinetics of their formation is largely unknown and only recently has been addressed.^{57,58,59,60} Gas clathrates have been subjected to growing interest last decades⁶¹ in particular for energy issues and global warming concerns. The gas storage capacity of such compounds are indeed relevant for addressing the global demand for fossil energy, hydrogen storage^{62,63} or for CO₂ sequestrations.⁶⁴ In addition, the guest-host repulsive interactions make clathrate hydrates interesting systems for the study of hydrophobic interactions, and their unexpected stability is also of interest for the description of planetary interior.

Due to the character of the guest-host interaction, clathrate hydrates were expected to be stable for relatively modest pressures. However, it was observed quite recently^{65,66} that upon compression, gas clathrates usually present phase transitions^{67,68,66,69} involving reorganization of the polyhedral ice cages toward hydrogen bonded structure close to the ice phases. These structures are thus known as filled ices,⁶⁵ in which the water network forms channels occupied by the guest molecules.⁶⁶ These structures allow stabilization at high pressure of both low-density ice phases such as the Ic or ice II phases induced by the guest-host interactions but also can be used to form metastable phase of ice (XVII) by removing guest molecules from the water network at ambient pressure.⁷⁰ Among the different filled ice phases, only three structures have been observed so far in addition to a recently discovered “chiral hydrate”.^{70,71} In this study, we focus on the filled ice structure shared by krypton, argon, nitrogen, and methane hydrates.^{72,66} In particular, we studied the methane hydrate III first observed by Loveday et al.,⁶⁷ and found to be stable beyond a pressure of a few GPa at ambient temperature.

This work has been conducted in collaboration with an experimental team composed of U. Ranieri, R. Gaal, W.F. Kuhs and led by L. E. Bove. Therefore, if not explicitly indicated, the experimental results presented in this chapter come from their work. Technical details of the simulations employed for this analysis can be found in the Appendix B.

Methane hydrate is the most widespread naturally occurring gas hydrate as it is present in large quantities in subsurface deposits, both in oceanic shelves sediments and in permafrost regions.⁵⁶ Therefore, as ocean warms up, a destabilization of the compound could release a significant quantity of greenhouse methane gas.⁷³ On the other hand, methane hydrates are present on Titan^{67,74} and on giant ice planets such as Uranus or Neptune where methane and water are abundant and coexist at very high pressure. In addition, methane hydrates are also suspected to exist at depth in many water-rich objects populating the outer solar system⁷² and space probes have sporadically detected the presence of methane in the atmosphere of Mars⁷⁵ whose origin might be linked to the destabilization of hydrates existing at depths.⁷⁶ Therefore, several experimental studies in the last years focused on the high-pressure behavior of methane hydrates.^{65,72,66,77,78,79,80,81,82,83,84,85,86,87,88,89,90}

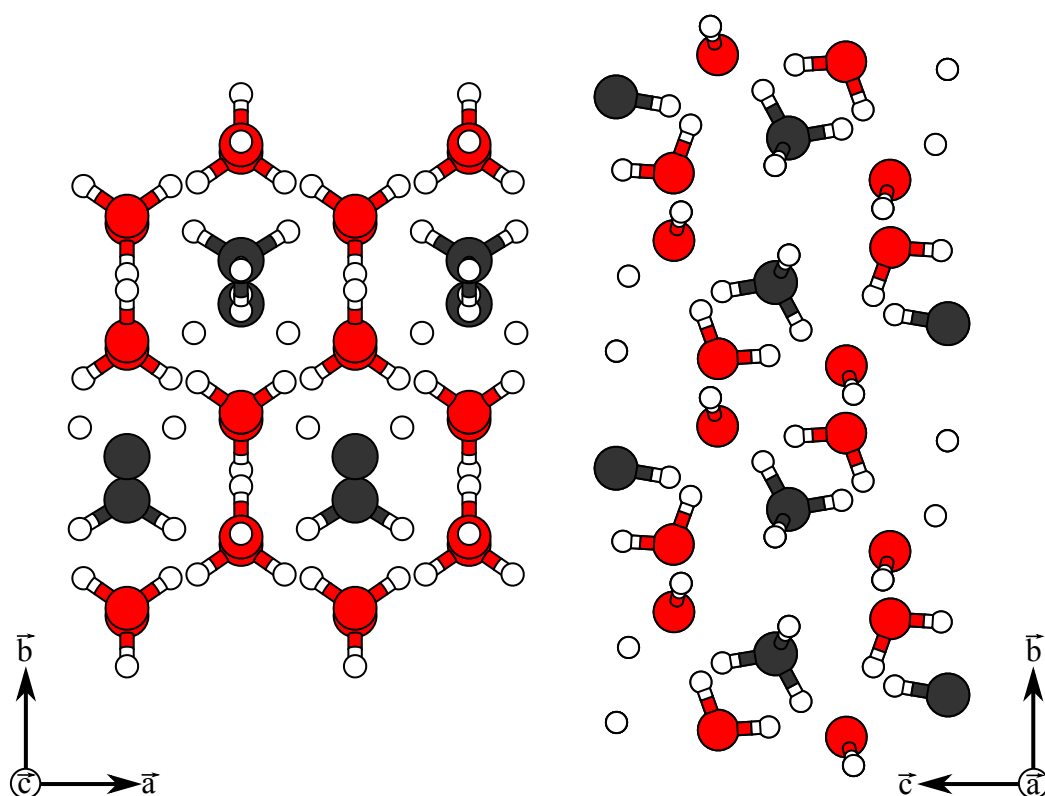


Figure 2.1. Sketch of the MH-III structure.

2.1.1 MH-III structure

The MH-III phase structure belongs to the $Imcm$ space group with oxygen atoms located on the $8i$ Wyckoff sites and carbon atoms located on the $4e$ sites.⁶⁶ As shown in Figure 2.1, the MH-III structure has its water network related to the ice Ih , in particular within the (a, b) plane where six-fold water rings are stacked thus leading to hexagonal channels along c wherein are enclosed the methane molecules. In contrast, it presents differences with the ice Ih within the (b, c) plane where we find 4-fold and 8-fold water rings, the latter forming octagonal channels along a where methane molecule are arranged in a zig-zag fashion along b and c . In addition, due to the different water rings present in the structure, inequivalent O-H-O bond lengths are found due to different O-O distances (2.811, 2.807 and 2.783 Å). These different O-O distances are shown in Figure 2.2, as we will discuss, they can induce several hydrogen bond symmetrization in the structure. The optimal $H_2O:CH_4$ ratio is two, which is the stoichiometry we used to model

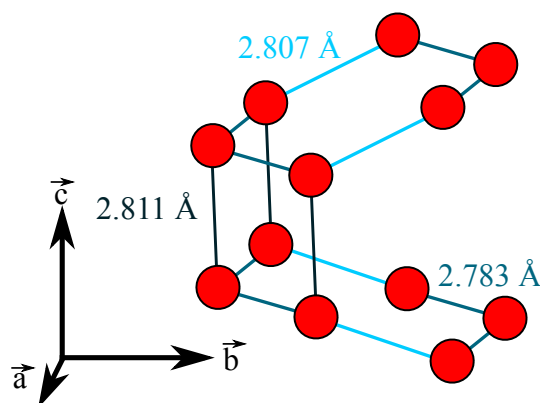


Figure 2.2. Sketch of inequivalent O-O distances present within the MH-III structure. Values of the O-O distances are given for pressure of ~ 2.3 GPa

the structure.

The different experimental results provided by Raman spectroscopy,^{82,83,84,85,86,87,91} x-ray diffraction,^{65,82,77,78,80,81,87,79} neutron diffraction^{65,72,92} and also theoretical calculations⁹³ raised several open questions that we want to address in this chapter.

• Guest-Host interactions

Upon compression, many entangled phenomena are expected to occur in the system. Notably, the enhancement of the guest-host interactions could give rise to a coupling between the guest and host dynamics, which are expected to stabilize the structure.^{94,95} In particular, a Fermi resonance between the O-D stretching mode of the water frame and the overtone of the D₂O bending was observed⁸⁸ at 15GPa. In this context, a splitting of the C-H stretching mode occurring above 20GPa was observed by Raman spectroscopy^{80,87,85} and has been assumed to be a marker of a possible methane orientational ordering along with an eventual distortion of the latter molecules.⁸⁸ However, up to now, no microscopic description of the guest-host interactions has been provided, and neither the possible orientational ordering of the methane molecule nor the guest-host coupling has been confirmed.

• Hydrogen bond symmetrization

As being composed of a hydrogen-bonded water network, a symmetrization transition⁹⁶ of the MH-III structure is expected to occur upon compression. A hydrogen bond symmetrization transition was first observed in the VII \rightarrow X transition of ice for which the quantum properties of the hydrogen nuclei play an essential role.^{1,4} The most striking one regards the computed transition pressure at room temperature, which is reduced in ice from approximately 100 GPa within the classical frame down to 65 GPa, in agreement with the experimental findings, when nuclear quantum effects are included. In methane hydrate, the symmetrization transition was guessed to occur above 60 GPa from an analysis of the O-O distances within *ab-initio* molecular simulations^{89,88} without taking into account NQE, but it has not been confirmed yet.

• New high-pressure phase

Finally, a pressure-induced phase transition from MH-III toward another high-pressure phase of methane hydrate was suggested by several experimental studies. In particular, new features were observed in X-ray diffraction experiments^{81,97,80,87} suggesting another structure which appears

beyond 40-50GPa.^{80,81,85,87} As conjectured by these results, this new high-pressure structure remains stable to at least 86GPa.⁸¹ However, X-ray diffraction patterns did not allow to identify it, and the new phase remains unsolved up to now.

Therefore, in the present chapter, we address these issues by accounting for the nuclear quantum effects which, as we will see, are essential to describe the methane hydrate under high pressure. In the first section, we will discuss the behavior of the enclosed methane molecules within MH-III and the pressure-enhanced guest-host interactions. Then, in the second section, we will describe the hydrogen bond symmetrization mechanism leading to the MH-III phase. In the third part, we will present the new MH-IV phase we discovered and characterized the MH-III → MH-IV transition in the last part.

2.2 MH-III under pressure

Most available experimental data concern vibrational spectra in MH-III, mainly obtained by Raman spectroscopy under high pressure. Therefore in order to interpret the Raman data and to understand the behavior of both methane and water molecules and their interaction in MH-III, we first provide an analysis of the vibrational spectra from QTB simulations at ambient temperature. From a dynamical matrix analysis, we can characterize each vibrational mode revealed by the Fourier transform of the velocity autocorrelation functions.

2.2.1 Spectral analysis

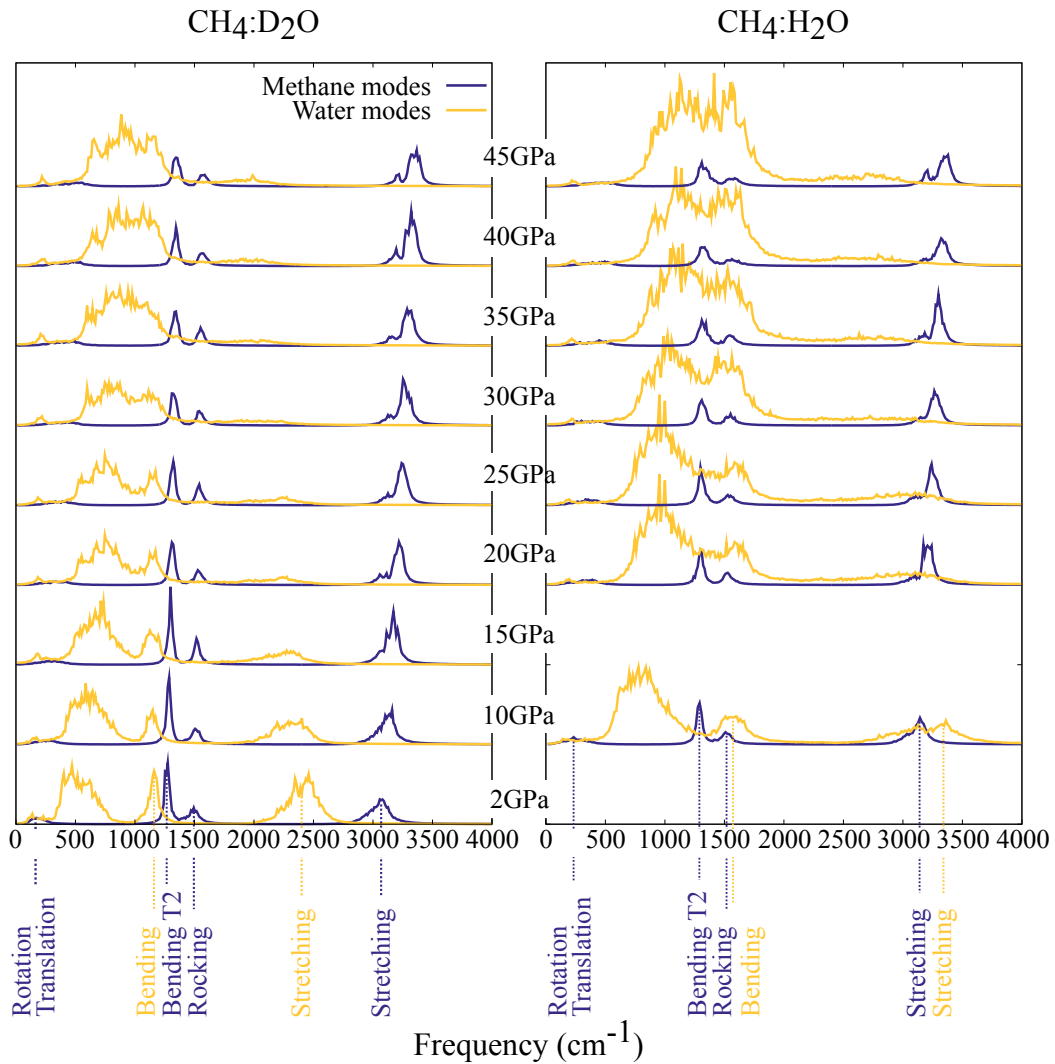


Figure 2.3. Methane and water frame vibrational spectra calculated with the Fourier transform of the velocities autocorrelation functions. left: deuterated system $\text{CH}_4:\text{D}_2\text{O}$; right: protonated system $\text{CH}_4:\text{H}_2\text{O}$.

In Figure 2.3, we present the vibrational spectra of the deuterated and protonated ice frames. In both structures, we can distinguish the water and methane bending and stretching modes as well as the methane rocking mode. In the deuterated system, the water stretching modes intensities flatten and their frequencies downshift upon compression providing a hint of H-bond symmetrization transition, as we will discuss in the next Section 2.3. Moreover, as its frequency

downshifts, the peak relative to the O-D stretching becomes wider with pressure and extends over the CH₄ rocking mode. Thus, this gives rise to the progressive mode coupling and eventually the resonance between these modes, occurring at ~ 20 -25GPa in CH₄:D₂O.

In the protonated system, the water stretching modes also flatten, and their frequencies downshift but at much higher frequencies while the methane rocking and H₂O bending modes vibrate at the same frequency as the deuterated system, even at the lowest pressure. Therefore, in CH₄:H₂O, the coupling already occurs at the formation of the system, between the H₂O bending and the CH₄ rocking modes, while the OH stretching is not likely to interfere with the CH₄ bending modes.

From the simulated vibrational spectra, we extract the frequency of each well-defined mode, in order to investigate the possible change of behavior of the system upon compression.

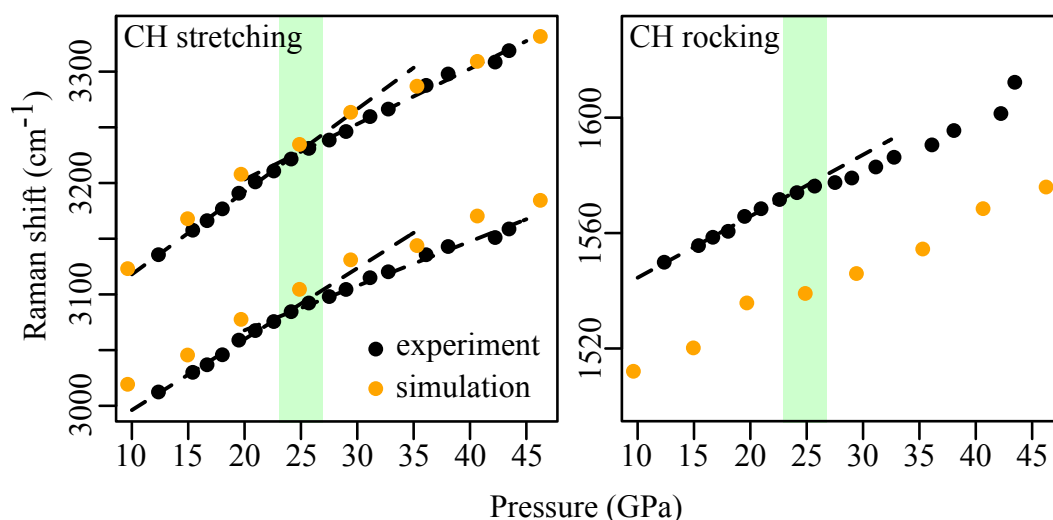


Figure 2.4. CH₄ stretching (left) and rocking (right) mode frequencies as a function of pressure for the CH₄:D₂O system. Simulation results are extracted from QTB trajectories. Dashed lines are linear fit of the experimental data points below 25GPa. A deviation from the linear trend is evident for all data points above 25GPa.

In Figure 2.4, we reported the calculated frequencies of the methane stretching and rocking modes of the deuterated system to be compared with experimental Raman results. Despite the difference of about 35 cm^{-1} between the observed and calculated CH₄-rocking mode, the latter frequency at 25GPa is located at a value that is quite similar to the calculated one reported in ref.⁸⁸ and remains within the expected DFT precision.

Interestingly, both experimental and theoretical results show that the observed vibrational modes follow the same evolution upon compression. Indeed, all frequency dependencies on pressure deviate present a slight change of slope occurring at $P \approx 20$ GPa. It involves the methane molecules but also the D₂O network as the experimental values of the lattice mode present the same behavior. We do not present these results here as the latter mode was not characterizable in our simulation. The observed changes of slope of the pressure dependence in both water frame and guest modes around 20GPa suggest an enhanced coupling of the guest and host dynamics, which has been conjectured but never detailed so far.

Further investigations are thus required to understand the role of methane and water molecules and their interactions. To do so, in the next section, we focus our attention on the methane behavior in MH-III upon compression, by a microscopic description of the latter.

2.2.2 Methane ordering and locking-in

In this section, we focus on the dynamics and orientation of the methane molecules. The orientation of the methane molecules enclosed within the water frame was investigated by calculating the Orientational Probability Density Function (OPDF) $P_{\text{CH}}(\theta, \phi)$ of the C-H bonds for different pressures. For the sake of clarity, we first performed this analysis for a single methane molecule.

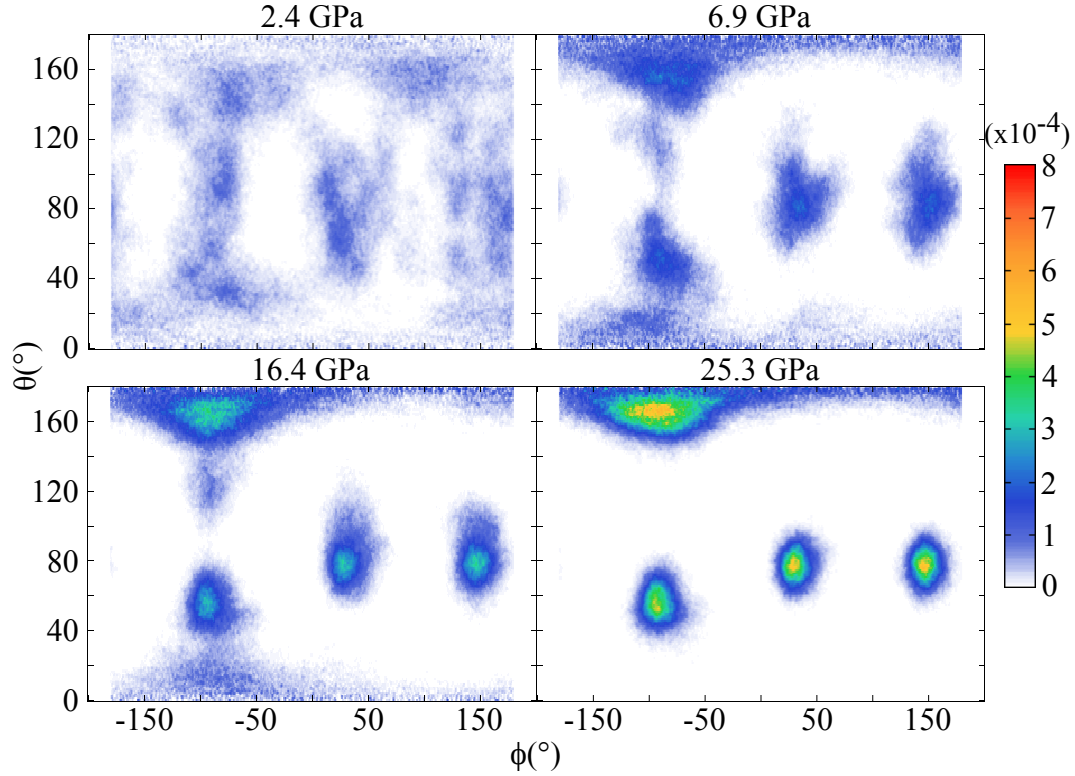


Figure 2.5. Probability distributions of CH vector polar angles $P_{\text{CH}}(\theta, \phi)$ extracted from PIMD simulation of $\text{CH}_4:\text{D}_2\text{O}$ at 6.9, 16.4, 25.3 and 36.4GPa, for one methane molecule.

As shown in Figure 2.5, at 2.4GPa, the probability distribution does not display clear favored orientational configurations. This indicates an important methane orientational disorder at low pressure probably induced by the molecule rotations. However, upon compression toward 25.3GPa, a clear structure appears in the OPDF where four well-defined peaks at $\phi, \theta \sim \{-90^\circ, 50^\circ; 40^\circ, 70^\circ; 150^\circ, 70^\circ; -90^\circ, 170^\circ\}$, corresponding to the four C-H bonds of the molecule. This indicates a progressive methane orientational ordering, occurring in MH-III upon compression.

By analyzing all the methane molecules present in the system, we can distinguish the four OPDF at 36GPa corresponding to four configurations that the methane molecules can adopt at high pressure, as shown in Figure 2.6.a. We labeled A_\pm and B_\pm these four configurations and present them in Figure 2.6.b. In our formalism, A and B configurations are equivalent by a rotation of π around \vec{b} and a rotation of π around \vec{a} while the difference between + and - configurations of the same type (A or B) corresponds to a rotation of π around \vec{b} . Therefore, the high-pressure structure yields A_+/B_- (or A_-/B_+) stacking along the b axis, while we observe A_+/B_+ (or A_-/B_-) stacking along axis c and finally A_+/A_- (or B_+/B_-) stacking along a . This characterizes the methane orientational ordering, which is not altered as pressure is increased up to 35GPa.

These results also tend to demonstrate the progressive locking-in of the methane rotational

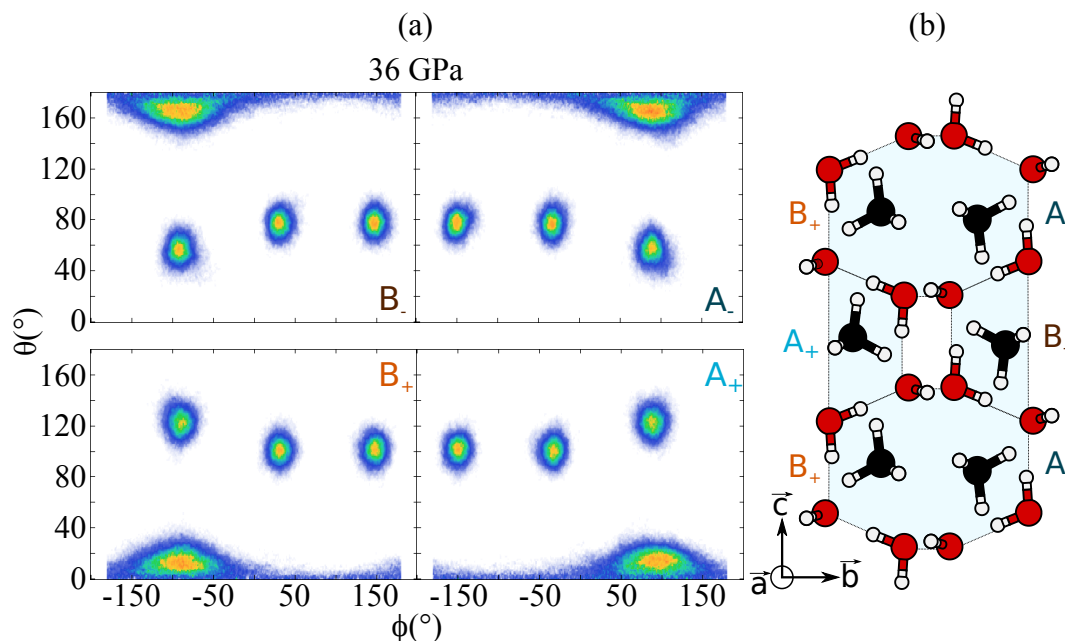


Figure 2.6. (a) Methane molecule configurations at 36GPa. (b) Sketch of the corresponding configurations in the structure.

motion as suggested by the increasing anisotropy of the OPDF upon compression. Indeed, at low pressure, we observe non-negligible probability density between the four configurations, that disappears for higher pressure. Thus, in order to better estimate the pressure dependence of the methane rotational motions, the OPDF $P_{CH}(\theta, \phi)$ were integrated either on ϕ or θ to yield marginal distributions $P_{CH}(\theta)$ and $P_{CH}(\phi)$.

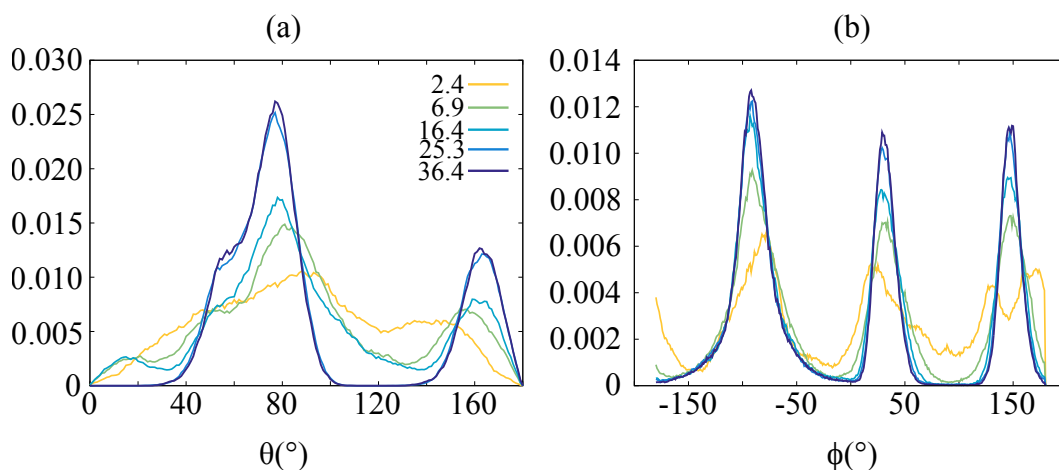


Figure 2.7. Methane orientational marginal probability distributions $P_{CH}(\theta)$ (left) and $P_{CH}(\phi)$ (right).

As shown in Figure 2.7, $P_{CH}(\phi)$ displays three main peaks at the positions defined earlier. The probability between them is non-negligible at low pressure but almost disappear at 6.9GPa. However, the probability distribution over θ shows a broad peak, almost isotropic over the angle range at the lowest pressure with no defined structure, indicating a considerable disorder along this coordinate. The related rotation motions were characterized (see Section B) and shown to be fully described by reorientation motions along one of the ternary axis of the methane molecules. Upon compression, two main peaks appear at 80° and 160° . While at the two intermediate

pressures, namely 6.9 and 16.4GPa, the non-negligible probability density which is present between the maxima, disappears at 25.3GPa, and the probability distribution does not evolve anymore upon compression. These results reveal the progressive locking-in of the methane rotations from 2.4GPa where it is almost free in particular along θ to 25.3GPa where all rotations are forbidden. This pressure threshold is specific to MH-III and the locking-in of the methane rotations could be at the root of the enhanced water-methane interactions revealed by the change of slope of the modes frequencies occurring at the same pressure.

2.2.3 Methane-Water interaction

Both the orientational ordering and the rotation locking-in of the methane molecules induce an increase in the interaction between methane and water molecules. In this section, we will discuss the different consequences caused by this interaction on both the methane symmetry and on their vibrational mode coupling.

• Methane distortion

As shown in Figure 2.8, the methane molecule ordering and locking-in influences the system

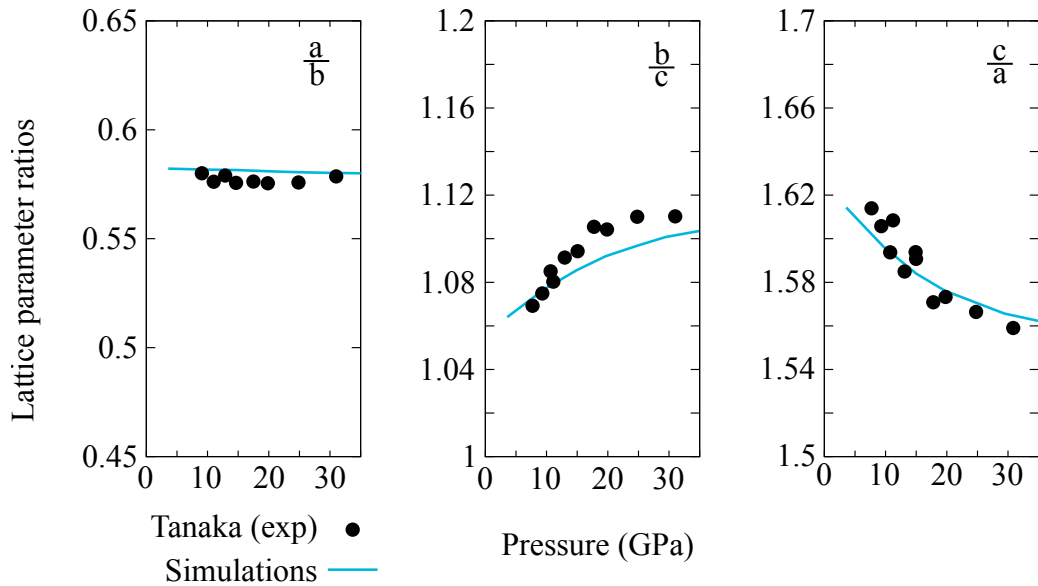


Figure 2.8. Lattice parameter ratios as a function of pressure. Experimental data from ref. [93].

compressibility. Indeed, the lattice parameter ratios as a function of pressure present the same behavior observed on the evolution of the mode frequency upon compression. While the $\frac{a}{b}$ lattice parameter ratio is almost constant within the explored pressure range, ratios involving the lattice parameter c present a change of slope at 20GPa. This change brings out the significant steric hindrance induced by the methane ordering and locking-in and points out the reinforced molecule-ice repulsive interaction, which could be at the root of molecule deformations. They are confirmed by the direct inspection of the angular distribution of the six \widehat{HCH} angles. We observe that at low pressure (3GPa), all angle probability distributions $P(\alpha_n)$ are centered around the tetrahedral angle of 109.47° , while, upon increasing pressure, two of them shift progressively away from the tetrahedral angle. We labelled these two \widehat{HCH} angles α_1 , which are almost parallel to the (a, b) plane, and α_2 the angles lying in the (b, c) plane. In Figure 2.9.a, we report the evolution of their mean value upon compression. The angle α_2 decreases with pressure due to the compressibility anisotropy observed along c , thus it makes the methane $H - H$ distances

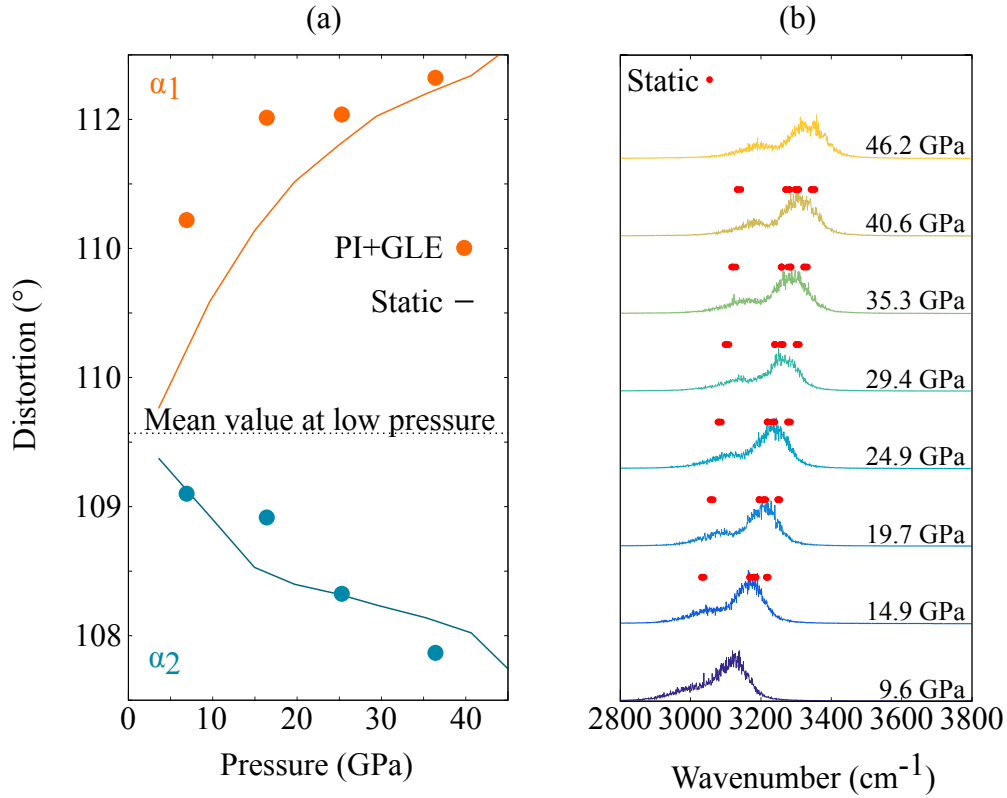


Figure 2.9. (a) Mean angles $\langle \alpha_{1,2} \rangle$ in CH_4 as a function of pressure from static relaxed configurations and PI-GLE simulations. (b) Lines: Fourier transform of the C-H autocorrelation function extracted from QTBS simulations; Dots: Methane stretching modes obtained within the harmonic approximation.

decrease along this direction. In contrast, the angle α_1 increases with pressure. This gives rise to the molecule flattening in the b direction where the nearest neighbors are the hydrogen atoms (see Figure 2.6).

The distortion of methane molecules enclosed in MH-III induces the observed change in the related vibrational modes. In addition, a signature of this distortion is accounted for by a lift of degeneracy of the CH_4 stretching modes: around 15 GPa for the antisymmetric ν_3 and around 25 GPa for the symmetric ν_1 C-H mode as shown in Figure 2.9.b. This lift of degeneracy present in static calculations within the harmonic approximation instead appears as a broadening (approximately 60cm^{-1}) while taking into account the dynamics of the molecules at ambient temperature.

• Mode coupling

The analysis provided earlier predicts a coupling between methane and water. Although the mode analysis within the harmonic approximation shows that at low pressure ($P < 10\text{GPa}$), the eigenvectors of the CH_4 rocking modes are fully localized on the methane molecules, as pressure increases, they progressively mix with the atomic displacements of the water frame. In order to quantify this coupling, we projected the mode eigenvectors $\vec{e}^{(\nu)}$ at each pressure on atomic displacements that are centered either on the deuterated water frame or the methane molecules:

$$\vec{e}^{(\nu)} = \sum_{i \in \text{D}_2\text{O}} b_i^{(\nu)} \vec{x}_i + \sum_{j \in \text{CH}_4} c_j^{(\nu)} \vec{x}_j \quad (2.2.1)$$

where $b_i^{(\nu)}$ and $c_j^{(\nu)}$ are the coefficients of the respective expansions for the mode at frequency ν .

We then calculated a methane participation ratio $P_{CH_4}(v)$ which describes the participation of the methane Degrees of Freedom (DoF) to the vibrational mode v :

$$P_{CH_4}(v) = \sum_{CH_4}^{DoF} \frac{c_j^{(v)^2}}{\vec{e}^{(v)} \cdot \vec{e}^{(v)}} \quad (2.2.2)$$

where the sum runs over all the CH_4 DoF.

The same expression holds for $P_{D_2O}(v)$ in which $c_j^{(v)}$ is replaced with $b_i^{(v)}$, which ensures that:

$$P_{CH_4}(v) = 1 - P_{D_2O}(v) \quad (2.2.3)$$

When $P_{CH_4}(v) = 1$ the mode v is totally characterized by the methane DoF contribution, while if $P_{CH_4}(v) = 0$ it is localized in the water frame. Figure 2.10 shows the participation ratios

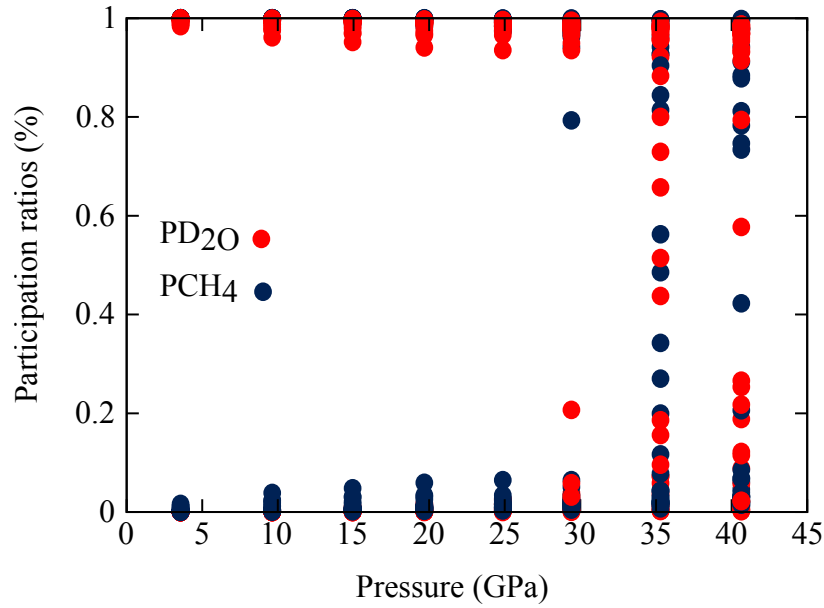


Figure 2.10. Mode participation ratios for methane (blue) and D_2O frame (red), computed according to equations 2.2.1 and 2.2.2.

(P_{CH_4}, P_{D_2O}) calculated for each methane bending and OD stretching modes as pressure increases. Up to 20GPa, $P_{CH_4} \sim 1$ or 0, the investigated modes are totally described either by the methane or the water DoF contribution. Starting at 20GPa some vibrational modes are described by a combination between the methane and water DoF contributions leading to a contribution coefficient $0 < P_{CH_4} < 1$. Due to the pressure induced mode coupling occurring in MH-III at 20GPa, it is not possible to attribute these modes to a methane bending or an OD stretching vibrational mode but rather to a mixed one. Their characters therefore deeply change in this pressure range.

To summarize, in this section, we mainly present the pressure effect on the methane molecules embedded in MH-III. We have shown that at low pressure, methane molecules almost behave as “free rotors” while upon compression, the progressive methane orientational ordering fully locks this rotation which becomes forbidden at 25GPa. This induces the distortion of methane tetrahedral angles triggering both the change of compressibility of the system along the lattice parameter c and the important coupling between methane and water vibrational modes. Having described the guest behavior, in the following section, we will focus our attention on the behavior

of the host, in particular, we will discuss the hydrogen bond symmetrization occurring within the water network.

2.3 The methane hydrate IIIs

In order to describe the hydrogen bond symmetrization transition in the MH-III structure, we first start by introducing this mechanism process in the simpler case of the ice VII \rightarrow X transition.

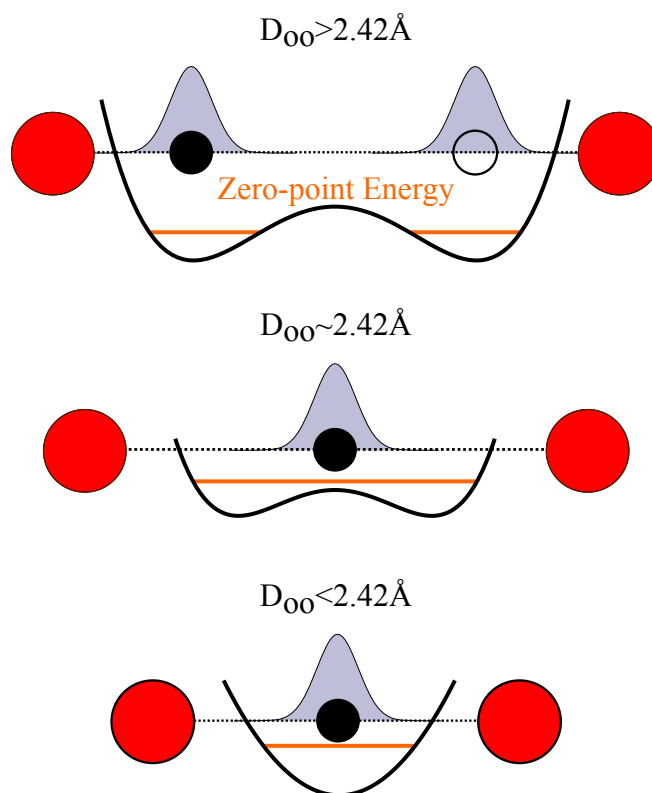


Figure 2.11. Description of the hydrogen bond symmetrization transition in the case of the ice VII \rightarrow X transition.

The ice VII \rightarrow X transition mechanism can be reduced to the description of the O-H...O bond in one dimension, as described in Figure 2.11. At low pressure, the proton between two oxygen atoms forms a covalent bond with one out of the two and a hydrogen bond with the other. This configuration leads to an effective double-well potential along the O-O direction^{98,99} as seen by the proton. This double-well potential is characterized by the OH vibrational frequency (stretching in 1D) of ~ 100 THz, the two equilibrium positions at ~ 0.96 Å from the oxygen atoms, and the effective barrier heights which depends on the O-O distance. Indeed, as pressure increases, the O-O distance decreases, lowering the barrier of the double-well potential. This decrease of the potential barrier induces proton delocalization in the two wells by the increase of tunneling. Finally, when the proton energy, taking into account zero-point contribution, is higher than the barrier height, the proton becomes centered in between the two oxygen atoms: this describes the hydrogen-bond symmetrization transition. We note in passing that the symmetrization transition can occur before the barrier has disappeared, because of zero-point energy.

In the case of the ice VII \rightarrow X transition, it occurs for a pressure of ~ 60 GPa, and O-O distance of ~ 2.42 Å. It has been shown,^{1,4} that taking into account NQE in the description of this transition is crucial as they downshift the transition pressure by ~ 40 GPa. Therefore, with a classical description of the nuclei, or by H/D isotopic substitution, the transition pressure is shifted toward ~ 100 GPa.

To describe such a mechanism, a standard order parameter χ has been extensively used⁴ to account for the location of the hydrogen nucleus between the two nearest oxygen atoms:

$$\chi = d(\text{O}^{[1]} - \text{H}) - d(\text{O}^{[2]} - \text{H}) \quad (2.3.1)$$

where $d(\text{O}^{[n]} - \text{H})$ is the distance between the selected proton and its n^{th} oxygen nearest neighbor.

So defined, this order parameter is null for proton-symmetric hydrogen bonds while its probability distribution allows one to observe the evolution of the proton position toward the transition, and could give information concerning proton tunneling or thermal fluctuation. In MH-III several considerations concerning the expected hydrogen bond symmetrization transition need to be addressed: firstly, as the O-O distances are shorter than in ice VII at all pressures, it is reasonable to expect the transition to occur at a lower pressure. Secondly, as described before, three different O-H-O bonds can be distinguished in MH-III due to inequivalent O-O distances. Therefore, we can expect a complete symmetrization of the structure to occur in three steps. Then, in contrast with the ice case, the host(water network)/guest(methane molecules) interactions could interfere during the transition. Finally, in analogy with the ice transition, it is reasonable to expect nuclear quantum effects to be relevant, and isotopic substitution to have an impact.

2.3.1 From MH-III to MH-IIIs

• Complete symmetrization

In Figure 2.12, we present the different probability distributions of the order parameter χ in protonated(left) and deuterated(right) MH-III systems calculated from all O-H-O bonds(top) and distinguishing the different inequivalent O-O pairs(bottom). In both systems, $P(\chi)$ evolves from a distribution with two maxima, which is characteristic of asymmetric hydrogen bonds, with significant tunneling between the two positions, to a single-peak distribution, which denotes the symmetric hydrogen bonds, around 40GPa. This points towards a symmetrization transition of the ice network in MH-III around 40GPa, therefore at a much lower pressure than in pure ice, as expected. We named the H-bond symmetrized MH-III phase “MH-IIIs”.

One can also note that even at quite low pressure the distribution does not vanish for $\chi = 0$ ($P(\chi = 0) \neq 0$) showing that the ice skeleton is proton disordered even at $P \sim 10\text{GPa}$.

A second confirmation of the transition is given by the vibrational spectra through the Fourier transforms of the time correlation functions. In particular, we examined the velocity-velocity time correlation functions $\langle \dot{r}_\alpha(t) \dot{r}_\alpha(0) \rangle$, where r_α is the α component of vector joining the proton (deuterium) in the ice cage and its oxygen first neighbor $\text{O}^{[1]} - \text{H}$. We then considered the projections of the previous vectors parallel or perpendicular (r_\parallel and r_\perp , respectively) to the $\text{O}^{[1]} - \text{O}^{[2]}$ axis. As shown in Figure 2.13, the spectra of the parallel components \dot{r}_\parallel show a shallow minimum around 35-40GPa, which is consistent with the softening of the shorter hydrogen bonds. Such a softening is a signature of the symmetrization transition, as discussed in the case of pure ice,^{4,99} which points towards a critical pressure around 35-40GPa, consistently with the indications from the distribution of the corresponding order parameter χ .

• Two steps process

In order to address the expected H-bond symmetrization in three steps, we pursue the same analysis by distinguishing the three inequivalent O-H-O bonds present within the MH-III structure. The corresponding probability distributions for the order parameter $P^{(\alpha)}(\chi)$, $\alpha = a, b$ or c are presented in Figure 2.12.b. $P^{(\alpha)}(\chi)$, for $\alpha = a$ and b , superimposed and shows two

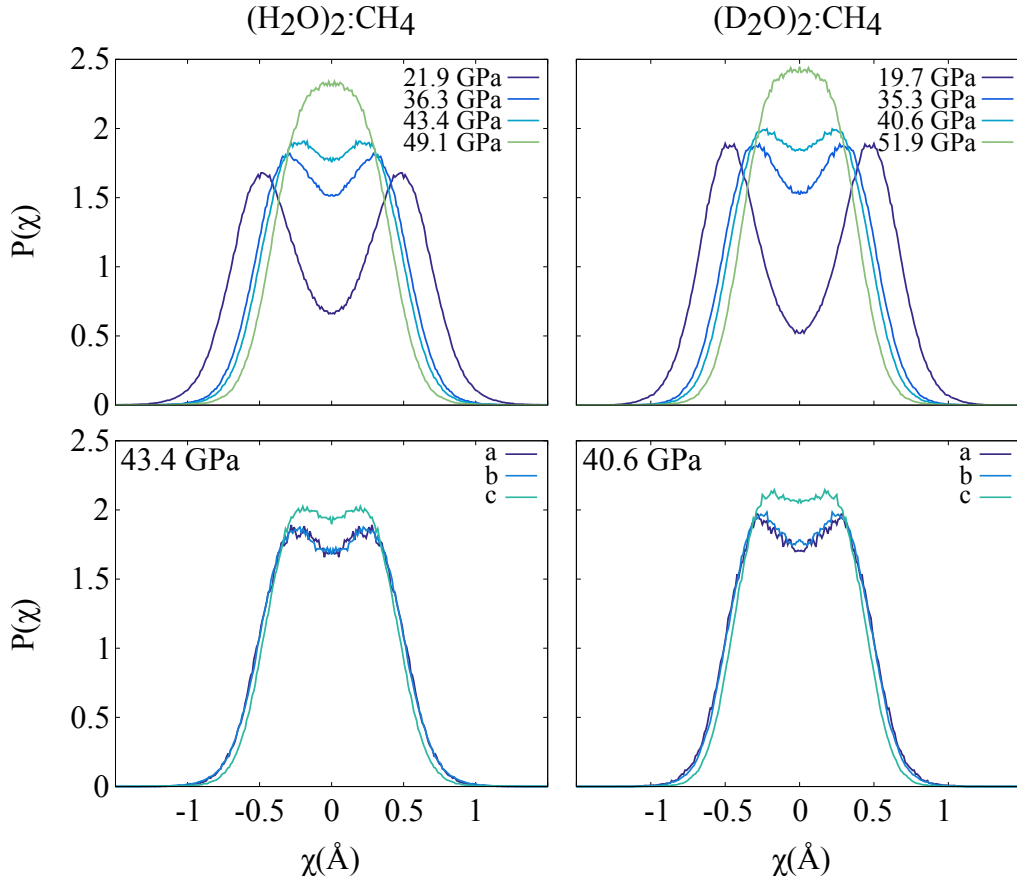


Figure 2.12. Distributions of the order parameter $P(\chi)$ calculated from QTB simulations of the protonated (left) and deuterated (right) ice skeleton, at several pressures. Upper panels: $P(\chi)$ is computed by integrating on all hydrogen bonds. Bottom panels: Distributions of the order parameter $P(\chi)$ for each group of O-O equivalent distances (a , b , c) (see text).

maxima at 40.6GPa and 43.4GPa for the deuterated and protonated ice skeletons, respectively, while $P^{(c)}(\chi)$ is flat around $\chi = 0$. The difference between the distributions reveals that the transition finally takes place in two steps due to the comparable O-O distances of two of them: at slightly lower pressures, the hydrogen bonds are symmetrized along the shorter O-O axes in group (c), and those in the remaining groups follow, with a delay corresponding to a few GPa. The picture that emerges from the $P^{(a)}(\chi)$ distributions is that of a symmetrization transition that extends over ~ 5 GPa around 40GPa rather than happening at a precise critical pressure, as in the case of pure ice.⁴

2.3.2 Nuclear quantum effects and isotopic substitution

In contrast with the case of pure ice, the isotopic substitution does not induce essential differences in the hydrogen bond symmetrization transition of the MH-III structure. Indeed, $P(\chi)$ behaves somewhat similarly in both protonated and deuterated water network. Secondly, as for the $P(\chi)$ distributions, the spectra for protonated and deuterated ice cages little differ once the latter have been renormalized by the mass ratio $\sqrt{2}$. This implies that isotope effects are practically negligible, and suggest modest overall nuclear quantum effects, in striking contrast with the case of ice VII \rightarrow X transition for which isotope effects induce a shift of ~ 40 GPa in the transition pressure. As shown in Figure 2.14, at 40GPa, PIMD simulations gives the MH-III structure to be symmetrized, while a classical Langevin description still describes an asymmetric hydrogen

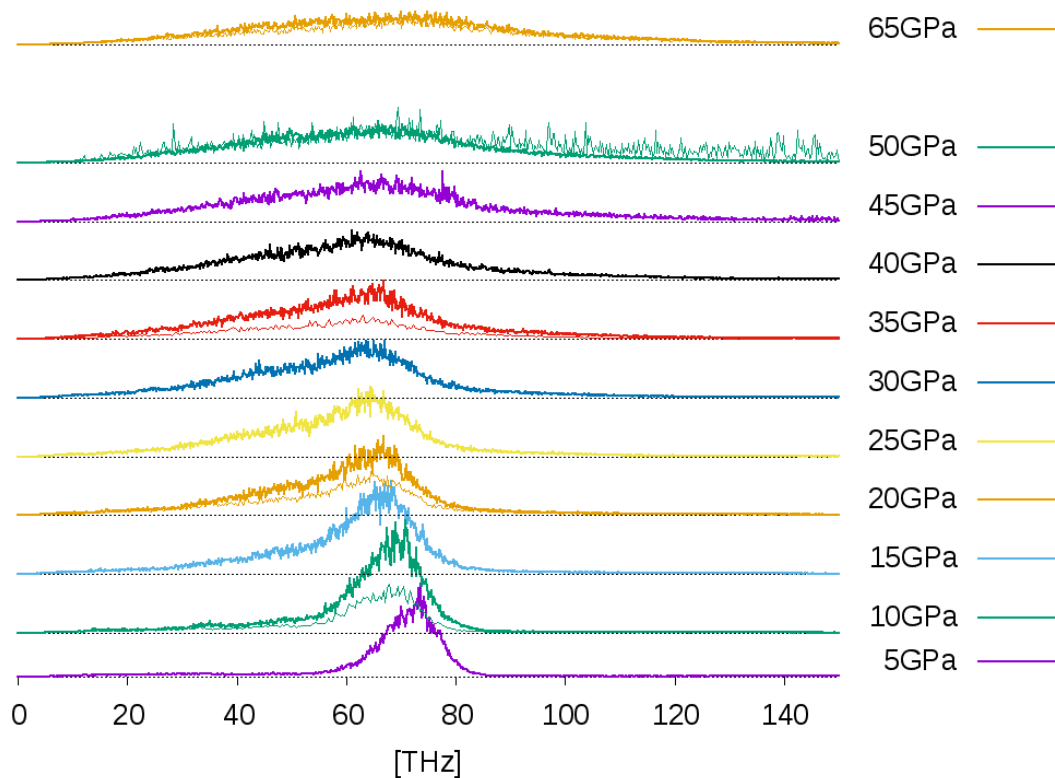


Figure 2.13. Fourier transforms in the frequency domain of the parallel component of the velocity-velocity time-correlation functions $\langle \dot{r}_{\parallel}(t)\dot{r}_{\parallel}(0) \rangle$ along the O-O axis extracted from QTB trajectories. Thick lines are for $\text{CH}_4\text{-D}_2\text{O}$, thin lines for $\text{CH}_4\text{-H}_2\text{O}$. The frequencies of the latter spectra were divided by $\sqrt{2}$ in order to take into account the mass difference.

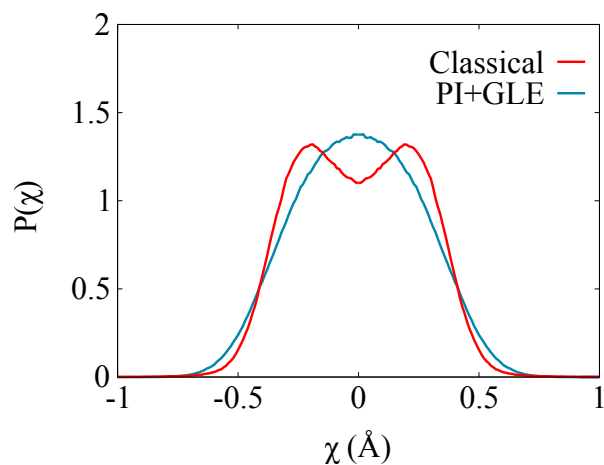


Figure 2.14. Comparison of the H-bond symmetrization occurring in deuterated MH-III between classical and quantum description around 40GPa. The nuclear quantum effects are taken into account by the use of path integral with a Generalized Langevin Equation (GLE) thermostat to reduce the number of replica.

bond. The influence of NQE has been evaluated to shift the transition by about 10GPa. This difference is much lower than the case of the ice VII \rightarrow X transition. We note in passing that it

also shows a small difference (few GPa) between PIMD and QTB descriptions.

Therefore, to understand both the unexpected absence of H/D isotope effect and the low overall NQE on the latter transition, a more in-depth analysis is required. Thus, in the following part, we will go beyond the usual one-dimensional representation of the hydrogen bond symmetrization by distinguishing the proton motion along or normal to the O-O axis.

• The proton normal delocalization

Using simulation data from⁴, we compare the hydrogen (and deuterium) distribution of MH-III

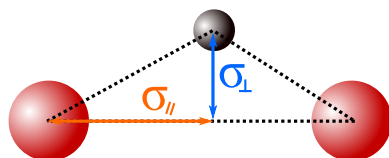


Figure 2.15. Sketch of the normal (r_{\perp}) and parallel (r_{\parallel}) components of the proton (deuteron) delocalization.

with that of ice under pressure, by decomposing the normal r_{\perp} and parallel r_{\parallel} delocalization components as shown in Figure 2.15.

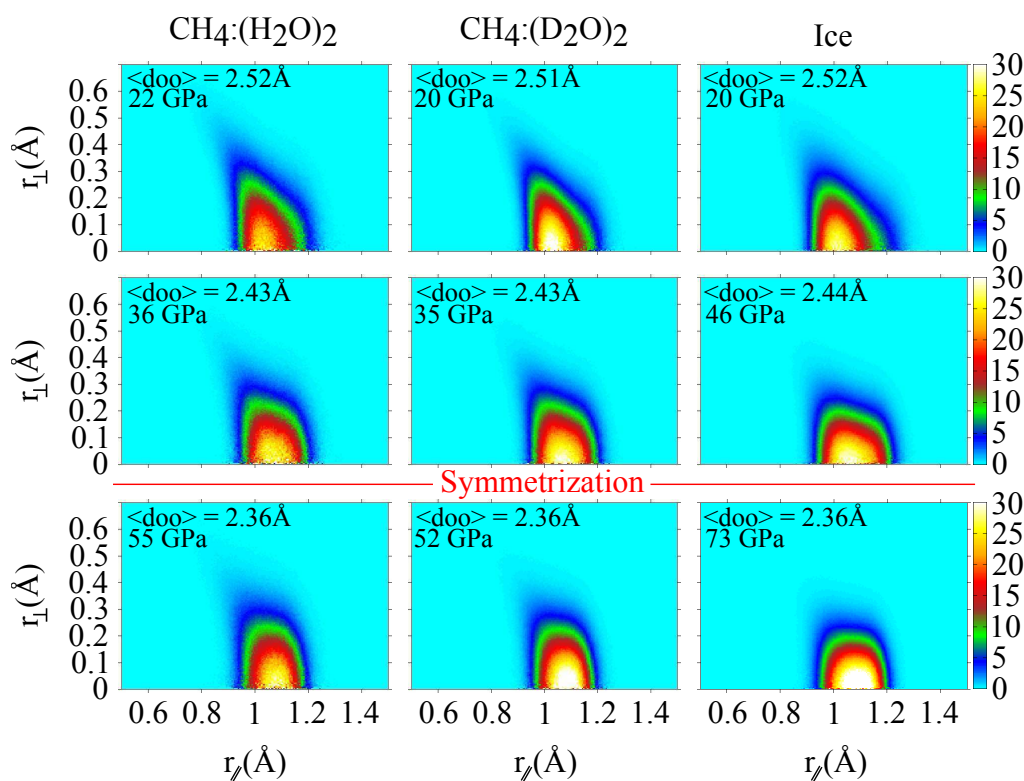


Figure 2.16. Probability density $P(r_{\parallel}, r_{\perp})$ calculated from QTB simulations of $\text{CH}_4:(\text{H}_2\text{O})_2$ (left) $\text{CH}_4:(\text{D}_2\text{O})_2$ (middle) and ice (right) systems at three pressures: one below the transition, one close to it and one above. Pressure values have been selected so that the mean OO distances $\langle d_{oo} \rangle$ in the three systems match, as the hydrogen bond symmetrization process is controlled by this parameter.

Figure 2.16 shows the proton probability distribution $P(r_{\parallel}, r_{\perp})$ for both ice and methane hydrate with protonated or deuterated water frame. One observes that the OH r_{\parallel} distances are approximately the same in both compounds as are the parallel widths, while the normal extension

is larger for the hydrates at all pressures, with a significant amplitude up to $r_{\perp} \approx 0.4 \text{ \AA}$. The inverted comma shape of the distribution indicates that the hydrogen atoms, as they move, tend to retain a relatively constant O-H distance. As pressure is increased, the shape of the distribution changes: the parallel contribution is sensitive to increased tunneling and thus broadens until approximately 40GPa while the normal contribution tends to shrink slightly. This analysis confirms a broader distribution in the normal direction than along the O-O axis, for all three systems, and suggests that purely one-dimensional model Hamiltonians, like those usually adopted^{99,98} are unable to catch the complexity of the hydrogen bond in methane hydrate or other highly anisotropic systems. A finer analysis based on the differences of $P(r_{\parallel}, r_{\perp})$ between the protonated and deuterated cages shows that the radial delocalization is larger in the case of $\text{CH}_4:(\text{H}_2\text{O})_2$ than in $\text{CH}_4:(\text{D}_2\text{O})_2$ which itself is more significant than in the ice case.

• 2D representation

In this section, we aim at describing the effect of the normal proton delocalization in the symmetrization process. As we have seen, the usual,^{99,4,6} convenient one-dimensional model along the O-O axis does not efficiently describe the H-bond symmetrization in MH-III. Therefore, we analyzed the system in a two-dimensional model with cylindrical symmetry around the O-O axis to describe the effective proton potential while a harmonic normal contribution can be tuned to model confinement effect. Then we solved the related Schrödinger equation. The two degrees of freedom are thus r_{\parallel} and r_{\perp} and OH interactions are described by the sum of two Morse potentials:

$$V_M(r_{\parallel}, r_{\perp}) = V_0 (e_+(e_+ - 2) + e_-(e_- - 2)) \quad (2.3.2)$$

$$e_{\pm} = e^{-\frac{\sqrt{(r_{\parallel} \pm r_O)^2 + r_{\perp}^2} - r_e}{r_w}} \quad (2.3.3)$$

where V_0 is the potential depth, $\pm r_O$ the positions of the two neighboring oxygen atoms, r_e the equilibrium distance and r_w a measure of the width of the potential well.

The full potential, the hydrogen atom is submitted to, thus writes:

$$V(\mathbf{r}) = V_M(r_{\parallel}, r_{\perp}) + \frac{k_{\perp}}{2} r_{\perp}^2 \quad (2.3.4)$$

where the last term is a normal harmonic potential that tends to confine the hydrogen atom to the O-O axis.

We present the potential in Figure 2.17.

The resulting wave functions shown in Figure 2.18 are clearly affected by the confinement term, which favors the symmetrization. In addition, an estimate of the importance of the NQE can be given by the tunneling rate $\Delta E/\hbar$, where $\Delta E = E^{[1st]} - E^{[GS]}$ is the energy difference between the first excited state and the ground state. The non-intuitive result of this analysis, shown in Figure 2.19, is that ΔE increases with the confinement of the hydrogen atom along the normal direction: conversely, when the hydrogen atom is allowed to move sideways, as in MH-III, the NQE tend to disappear. This model gives an insight into the reason why NQE are hardly visible in MH-III. In addition, as the normal delocalization of the protons is larger for the case of the protonated compound as compared with the deuterated one, the NQE along the parallel component is compensated, lowering the difference between the two systems. This explains the low difference of symmetrization pressure for H/D isotopic substitution. Therefore, rather than an absence of NQE in MH-III, we stress that the normal and parallel proton (deuteron) delocalization play opposite roles and tend to compensate each other.

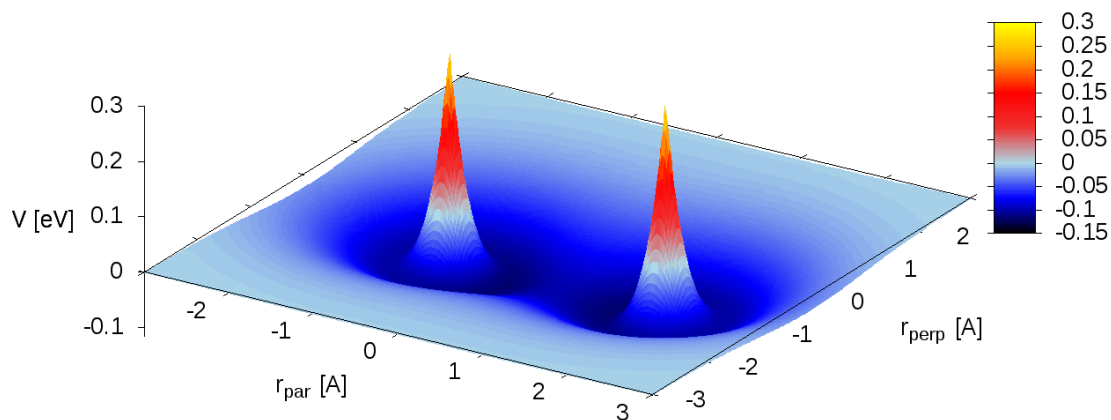


Figure 2.17. Double Morse potential as defined in equation 2.3.4 without the normal harmonic term (i.e. $k_{\perp} = 0$). The effect of the latter is to upcurve the edges in the perpendicular direction.

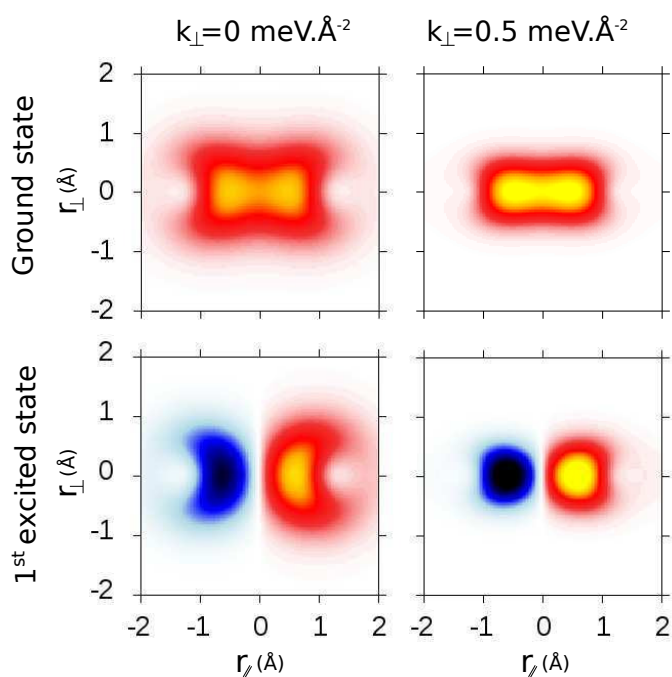


Figure 2.18. Ground state and first excited state wave functions resulting from the potential in equation 2.3.4 with no harmonic normal contribution (left) and with (right). Energy units are eV and length Å.

• H-H repulsive interaction

The conditional probability of the methane hydrogen to water hydrogen (resp. deuterium) distances given the normal delocalization $\rho(d_{\text{HH}}|r_{\perp})$ (resp. $\rho(d_{\text{DH}}|r_{\perp})$) presented in Figure 2.20,

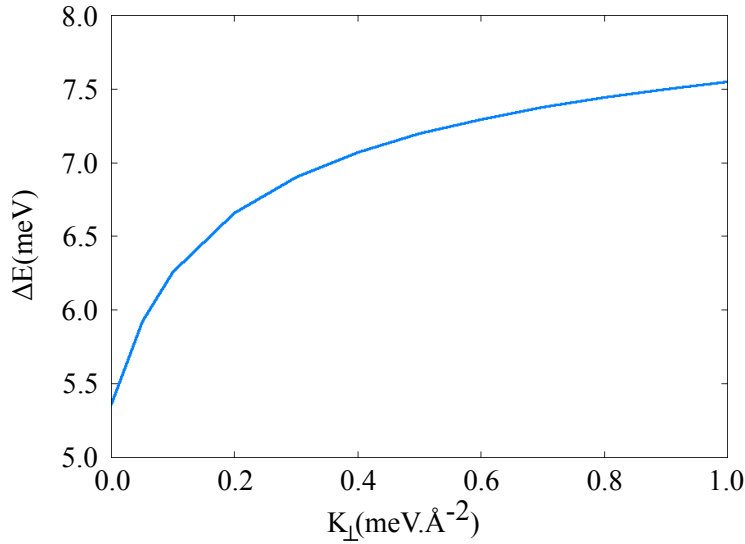


Figure 2.19. Energy difference $\Delta E = E^{[1st]} - E^{[GS]}$ between first excited state and ground state as a function of k_{\perp} .

show a clear correlation between the presence of a methane hydrogen and the sideways displacement of the cage hydrogen (deuterium) atoms. When protons in the CH_4 molecules approach the cage hydrogen (deuterium) below a typical distance ($\sim 2.0\text{\AA}$ at $P=10\text{GPa}$, $\sim 1.9\text{\AA}$ at $P=35\text{GPa}$ and $\sim 1.7\text{\AA}$ at $P=65\text{GPa}$), r_{\perp} tends to increase, in order to maximize d_{HH} (resp. d_{DH}). This shows that the normal delocalization is mainly a consequence of the repulsive interaction between the hydrogen (or deuterium) of the water network and those in the methane molecules.

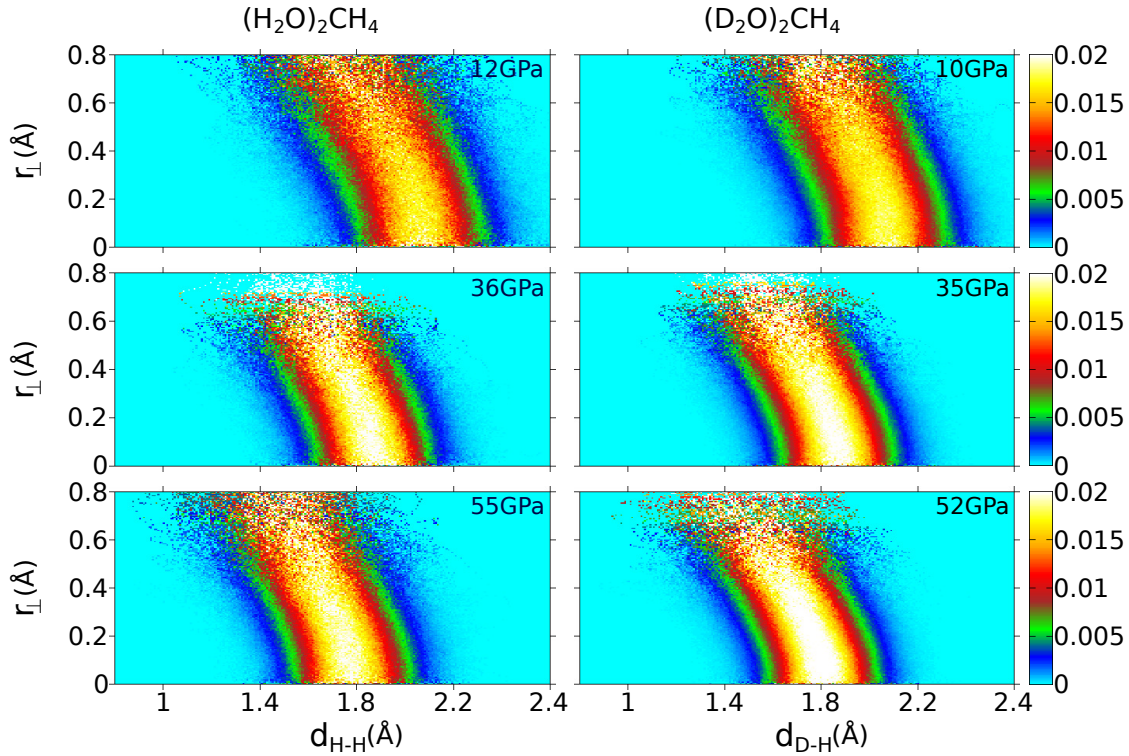


Figure 2.20. Conditional probability $\rho(d_{\text{HH}}|r_{\perp})$ for a protonated cage (left panels) or deuterated cage (right panels) extracted from QTB simulations.

Finally, the stability of the hydrogen bond network was analyzed by removing the methane molecules while keeping the oxygen atoms fixed to their original positions and letting the cage hydrogen atoms move freely. The result thereof is that these hydrogen atoms escape from the O-O axes, which shows that the repulsive interactions between the hydrogen of the guest CH₄ molecules and the hydrogen (resp. deuterium) of the water frame is also a key ingredient for the stability of the hydrogen bonds and thus of the overall system.

2.4 The methane hydrate IV

As discussed in the introduction, several experimental results suggest a pressure-induced phase transition of the MH-III at ~ 40 GPa. In particular, X-ray diffraction experiments^{81,80,87,97} indicate the presence of a new structure at 40 GPa, as the diffraction peaks are not compatible with MH-III. Raman spectroscopy yields two new vibrational modes and an important broadening of the two C-H stretching modes. Although guessed, this new structure has not been solved yet. In this context, we investigated a hypothetical destabilization of the MH-III structure from the proton dynamics as given by our QTB simulations.

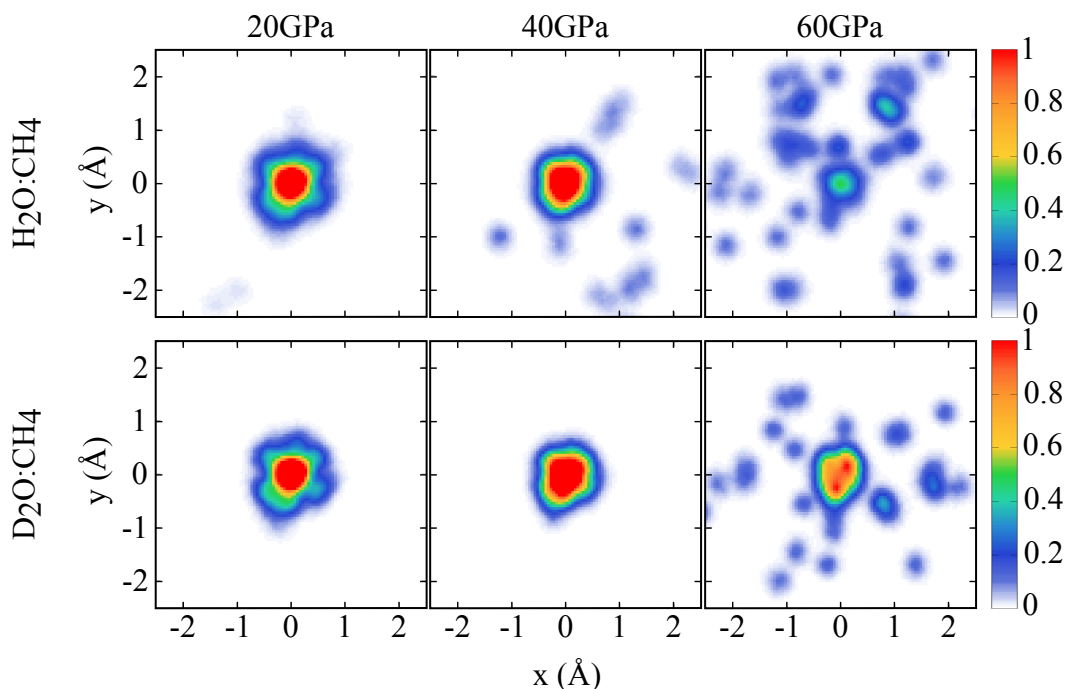


Figure 2.21. Probability distributions of the water protons (resp. deuterons) spatial delocalization within the (a,b) plane in MH-III, as given by the QTB simulations.

As shown in Figure 2.21, the analysis of the spatial delocalization of the water proton of MH-III within the (a,b) plane presents a pressure-induced diffusion of the proton within the ice frame. While in the protonated ice frame this process seems to start from 20 GPa and mainly increases at 40 and 60 GPa, a significant isotope effect is observed in the deuterated system, where the diffusion process seems to start for pressures close to 60 GPa. As we have seen for the case of Brucite minerals, the proton diffusion is indeed largely dependent of the NQE, which could ease the overcome of dissociation barriers. In addition, this process is visible by tracking the proton trajectories. However, this process begins to have a significant impact at 40 GPa only for the protonated system, and as discussed earlier, QTB method could overestimate proton hopping probabilities. Therefore, although we cannot rely on the exact pressure allowing diffusion as given by QTB simulations, these results provide an essential hint for structure destabilization through proton quantum delocalization. This was the starting point leading to the discovery of the new high-pressure methane hydrate phase.

In order to solve the new structure, a series of MH-III destabilized systems were optimized by force minimization through variable simulation cell relaxation. These structures were constructed by starting from MH-III from which one proton was taken away from a water molecule and replaced to form a non-stable H_3O^+ molecule within the ice frame to mimic the suggested proton

delocalization. All these new structures relaxed into the same configuration. While the methane molecules organization almost did not change, the ice frame reorganized into a structure much closer to the ice *Ih* phase as compared to MH-III. This result is unexpected, as a pressure-induced transition suggests a new denser ice phase for the composition of the host structure, as ice VII or X could be. However, taking the ice *Ih* as the host ice network and the methane molecules arrangement from our relaxation calculations led to a new stable high-pressure methane hydrate phase we named MH-IV, presented in Figure 2.22. In order to check the stability of the structure, we first tested other hypothetical systems with the MH-IV positions for the oxygen atoms and the MH-III positions for the methane, or the inverse. All these structures spontaneously relaxed to the MH-IV phase. Secondly, replacing methane molecules with large-radius rare gas atoms (Ar, Kr) resulted in a different structure, suggesting that the (quasi-)tetrahedral symmetry of methane molecule is a crucial parameter for this transition. This strengthens the emerging view of high-pressure methane hydrate as a strongly interacting inclusion compound, where a global optimization of both water and methane molecules should be fulfilled.

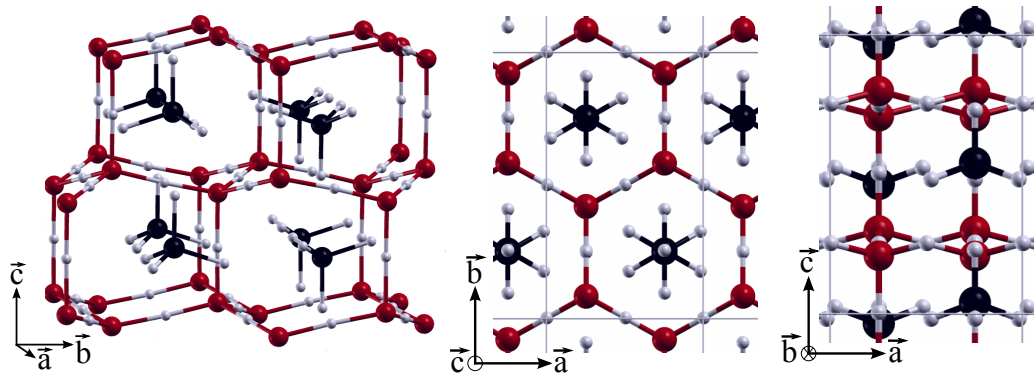


Figure 2.22. Ball-and-stick representation of the new high-pressure methane hydrate MH-IVs phase, seen in the three crystal planes. O atoms in red, C atoms in black, H in light gray. The reader can note in the left panel that methane molecules have a C-H bond oriented either along c (left) or \bar{c} (right).

Finally, to conclude on the stability of MH-IV, we calculated the free enthalpy difference $\Delta H = H_{\text{MH-III}} - H_{\text{MH-IV}}$ at $T = 0\text{K}$ as a function of pressure, obtained from static calculations. As shown in Figure 2.23, the MH-IV structure becomes more stable than MH-III for pressures higher than $\sim 30\text{GPa}$ while experimentally, MH-III seems to transform to a new phase at 40GPa .⁸⁰ Such a difference can be attributed to several factors. In particular, the fact that static energy calculations take into account neither thermal nor quantum effects but also the neglected entropy term of the methane rotational disorder. Therefore, from now on, we adopt 40GPa as the transition pressure. Upon further compression, the free enthalpy difference grows up to 400meV per methane molecule at 150GPa . Its trend shows that the stability of the new phase, with a smaller volume, increases steadily with pressure.

2.4.1 Structural properties

We investigated the structural similarities between the D_2O network in methane hydrate phases III and IV with respect to ice *Ih* through the topological distance D_X as given by:

$$D_X = \sum_{i=1}^N \sqrt{(r_i^X - r_i^{\text{Ih}})^2} \quad (2.4.1)$$

where N is the number of atoms; r_i^X indicates the reduced atomic positions of the i^{th} atom for the phase X ($X=\text{MH-III}$ or MH-IV) and r_i^{Ih} the corresponding ones in ice *Ih*.

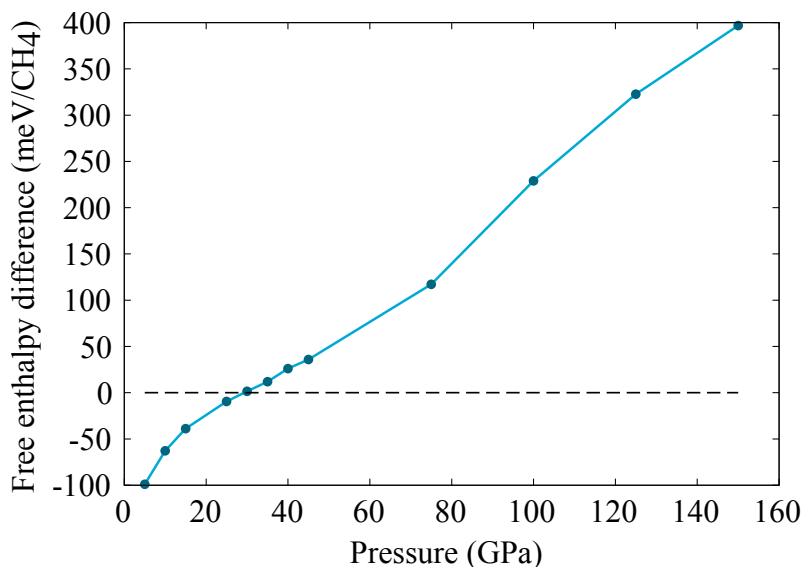


Figure 2.23. Computed free enthalpy difference $H_{\text{MH-III}} - H_{\text{MH-IV}}$ between MH-III and MH-IV structures at $T=0\text{K}$.

This allows us to determine that the topology of the D_2O network in the MH-IV phase ($D_{\text{MH-IV}} = 1.76$) is way closer to that of ice Ih than the MH-III phase ($D_{\text{MH-III}} = 10.87$). In addition, in MH-III there are four-, six- and eight-fold water rings while in MH-IV the H-bonded water network is composed of corrugated (a-b) sheets of edge-sharing six-member rings of water molecules which are cross-linked along \vec{c} as in ice Ih , thus avoiding the angular frustration that 4-member water rings imply.

Therefore, the new phase has an orthorhombic crystal cell based on an ice Ih skeleton. Both MH-III and MH-IV share the same stoichiometry, i.e. a 2:1 $\text{D}_2\text{O}:\text{CH}_4$ ratio. MH-IV space group is Pmnc ($n^\circ 62$) where oxygen and carbon atoms occupy 4c Wyckoff sites (Table 2).

In addition to a different water frame, MH-IV contains methane orientational ordering which differs from MH-III. Indeed, in MH-IV, the carbon atoms and a C-H bond in each methane molecule are aligned along the \vec{c} direction, where two symmetrical configurations that differ by a rotation of $\frac{\pi}{6}$ around \vec{c} alternate (Figure 2.22, lower left panel). Along \vec{b} , methane ordering presents another alternation by a rotation of $\frac{\pi}{3}$ around \vec{a} (Figure 2.22, upper panel). In this arrangement, all C-H bonds of the methane point toward the hexagonal channels formed by the host D_2O molecules, thus reducing repulsive methane-water interactions but also preventing methane rotations.

Finally, we reported in Figure 2.24 the simulated X-ray diffractogram of the MH-IV, for comparison with experimental observation present in the literature.⁸⁷

We can observe that the MH-IV simulated X-ray diffractogram quantitatively reproduces the location and intensity ratios of the main experimental x-ray diffraction peaks from ref.[87]. This provides a strong indication that the atomic positions of the C and O atoms of the simulated MH-IV structure match the experimental ones. Moreover, the suggested lattice parameters as calculated from the latter experimental X-ray study match the ones we obtained from variable-cell relaxation of MH-IV. We believe that such an excellent agreement is not accidental and that the MH-IV structure we propose corresponds to the unsolved one as obtained in ref. [87]. In Figure 2.25, we provide the evolution of the lattice parameters of the methane hydrate upon compression.

We can see that at the transition, while a and b increase a little, the significant change concerns c , which decreases by about 3.2% due to the particular methane ordering along this axis.

Phase	Group	Atom	Site	x	y	z
MH-III	Imcm 74	O	8i	0.250	0.080	0.830
		C	4e	0.250	0.680	0.000
MH-III _s	Pmcn 62	O	4c	0.250	0.400	0.190
		O	4c	0.250	0.420	0.810
		C	4c	0.250	0.800	0.980
MH-IV	Pmcn 62	O	4c	0.250	0.420	0.045
MH-IV _s		O	4c	0.250	0.420	0.455
MH-IV _s		C	4c	0.250	0.750	0.715

Table 2. Space group and fractional coordinates of oxygen and carbon atoms in the MH-III, MH-III_s, MH-IV and MH-IV_s phases of methane hydrate at 40GPa, as obtained from the AIMD simulations. For coherence sake with Imcm, the space group of the higher pressure phases is given in the non-conventional representation. The uncertainty on the fractional coordinates is ± 0.005 . Despite the different space group between MH-III and MH-III_s, the full oxygen positions are very similar. In MH-IV_s (H-bond symmetric phase IV), the oxygen and carbon atomic positions do not change significantly from those in MH-IV. Computed lattice parameters: MH-III_s (40GPa): $a = 4.006 \text{ \AA}$, $b = 6.911 \text{ \AA}$, $c = 6.249 \text{ \AA}$; MH-IV (40GPa): $a = 4.063 \text{ \AA}$, $b = 6.981 \text{ \AA}$, $c = 6.063 \text{ \AA}$.

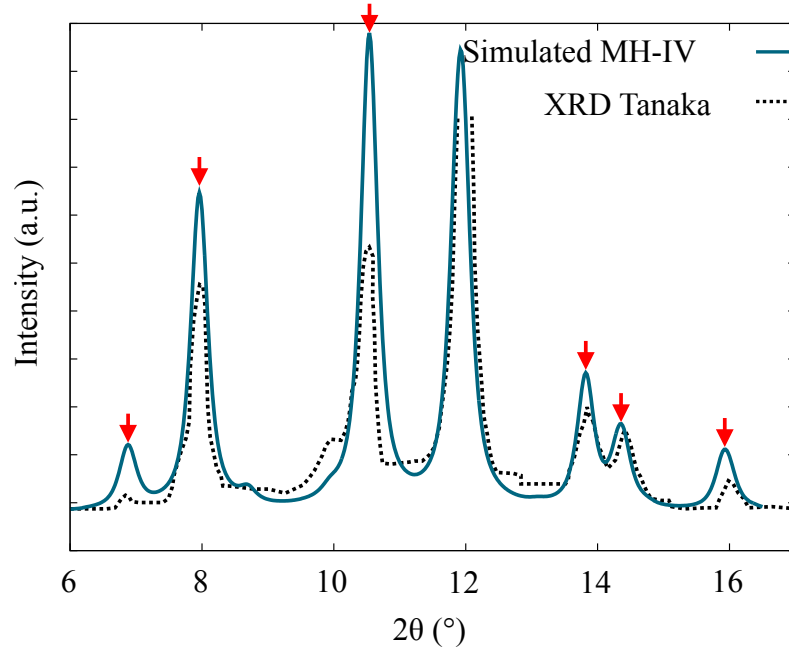


Figure 2.24. X-ray diffractogram at 55GPa from ref.[87], showing with red arrows the new peaks associated with the new phase, along with the simulated diffractogram ($\lambda = 0.4163 \text{ \AA}$) for our MH-IV structure.

2.4.2 Hydrogen bond symmetrization: MH-IV_s

The increase of the a and b lattice parameters also induces an increase of the O-O distances within this plane. As discussed in Section 2.3, O-O distances is the key parameter influencing the hydrogen bond symmetrization in such structures. Therefore, although before the transition toward MH-IV the system is already symmetrized, the increase of the O-O distances drive deuterons back to non-symmetric hydrogen bonds.

In order to characterize the hydrogen bond symmetrization, we calculated the probability distribution of the order parameter χ , already defined in Section 2.3, from our Path Integral

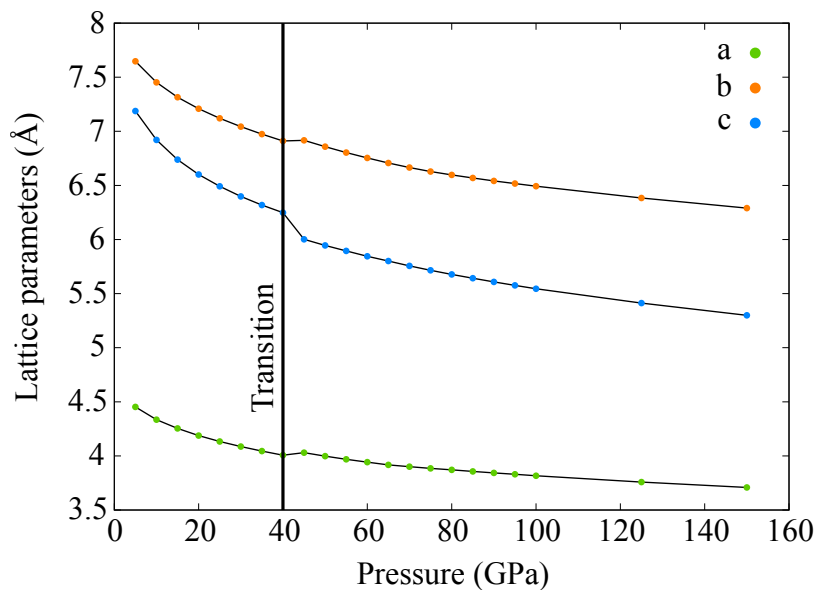


Figure 2.25. Simulated pressure evolution of the lattice parameters of the methane hydrate.

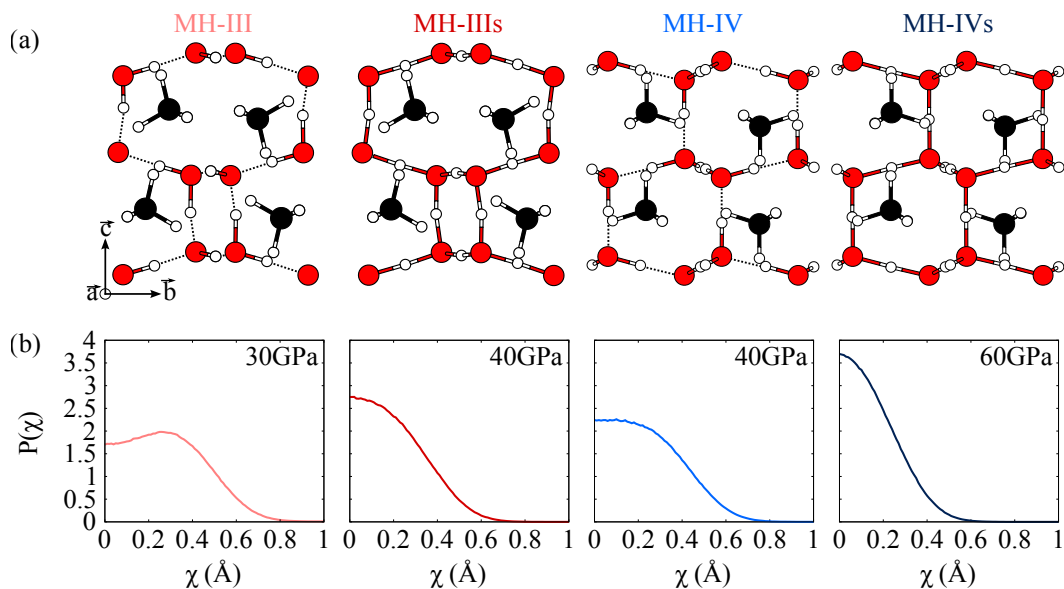


Figure 2.26. (a) Sketch of the main transitions from MH-III to MH-IVs, according to AIMD simulations. (b) Probability distributions of the order parameter χ of MH-III at 30GPa, MH-III_s at 40GPa, MH-IV at 40GPa and MH-IV_s at 60GPa, as obtained by PIMD.

Molecular Dynamics (PIMD) simulations. As shown in Figure 2.26.b, a slight desymmetrization effect indeed occurs while passing from MH-III_s to MH-IV. Then, further pressure increase triggers another transition, from MH-IV to MH-IV_s, where hydrogen bonds become symmetric. This leads to the following a sequence of high-pressure methane hydrate phases: MH-III, from 2.4 to 35GPa; MH-III_s around 35GPa; MH-IV at 40GPa; and finally MH-IV_s as shown in Figure 2.26.a.

2.4.3 Vibrational properties

The phase transition from MH-III to MH-IV can also be detected by looking into the behavior of the vibration modes as a function of the increasing pressure. In particular, and similarly to what occurs in MH-III, an important broadening of the C-H stretching mode is observed experimentally at 80GPa. In addition, two new vibrational modes appear beyond 100GPa. As these two experimental results could be signatures of the MH-IV(s) phase, we will first investigate the C-H stretching mode and then the presence of new vibrational modes.

• C-H stretching modes

As shown in Figure 2.27.a, the experimental full width at half maximum (FWHM) of the two

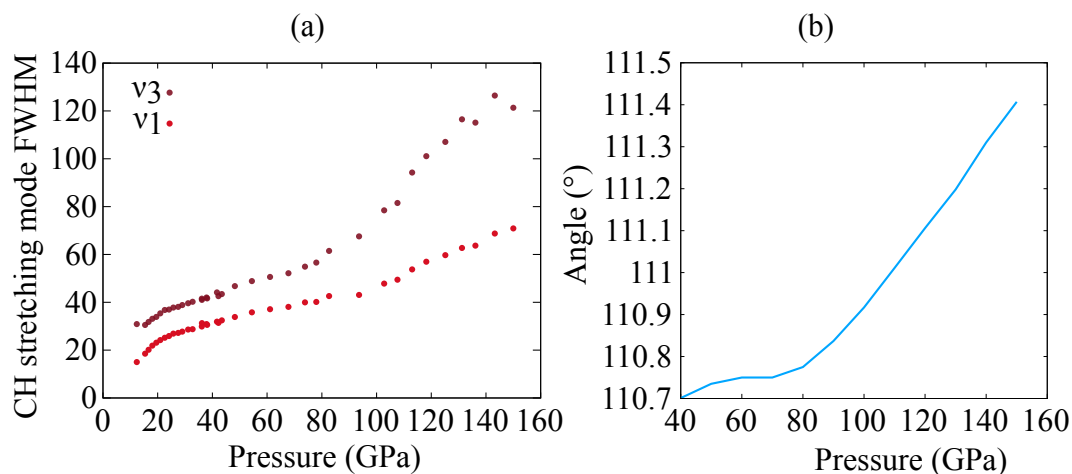


Figure 2.27. (a) Full width at half maximum (FWHM) of the CH₄ ν_1 and ν_3 stretching modes versus pressure as obtained from Raman spectra. (b) Angular distortion of one of the $\widehat{\text{HCH}}$ tetrahedral angles in MH-IV upon compression.

methane stretching modes in Raman spectra changes slope around 80GPa. To address this issue, in analogy with the methane distortion occurring in MH-III, we investigated the different tetrahedral angles evolution upon compression of the methane molecules in MH-IV. Indeed, as we have seen, in the MH-III structure, the methane molecules undergo an increasing distortion from tetrahedral symmetry upon compression leading to a broadening of the C-H stretching modes. It is interesting to note that after the transition to MH-IV, the $\widehat{\text{HCH}}$ angles of methane almost recover their tetrahedral value, as shown in Figure 2.27.b. However, while increasing pressure, we observe an important departure of the methane $\widehat{\text{HCH}}$ angle from the tetrahedral symmetry occurring at 80GPa. Therefore, the degenerate ν_3 and ν_1 modes split in similar, but non-degenerated modes. The computed width of the related frequency distribution explains the large broadening of the C-H stretching modes observed experimentally. A similar analysis also holds for MH-III under increasing methane distortion (Figure 2.27.b).

This effect deeply depends on the structure, as the methane distortion is due to both the steric hindrance and H-H repulsive interaction between methane and water molecules. In addition, as shown in Figure 2.28, the C-H stretching modes frequency evolution as a function of the pressure as obtained from our MD simulations perfectly match the experimental ones. Therefore, this experimental observation confirms the stability of the MH-IV phase up to, at least, 150GPa and this new phase represents the highest-pressure gas hydrate known up to now.

• Characteristic modes of MH-IV

Second confirmation is provided by the two new modes appearing beyond 100GPa, revealed

by Raman spectroscopy. These modes present between 900 and 1100 cm^{-1} are also detected in our MD simulations, as shown in Figure 2.28. Our theoretical analysis, within the harmonic approximation, describes these modes as being shared among the water and methane degrees of freedom in the MH-IV-structure. Indeed, this mixed vibrational mode involves both CH_4 bending and D_2O stretching modes. We denote them as IV-modes, as they are characteristic of the latter structure.

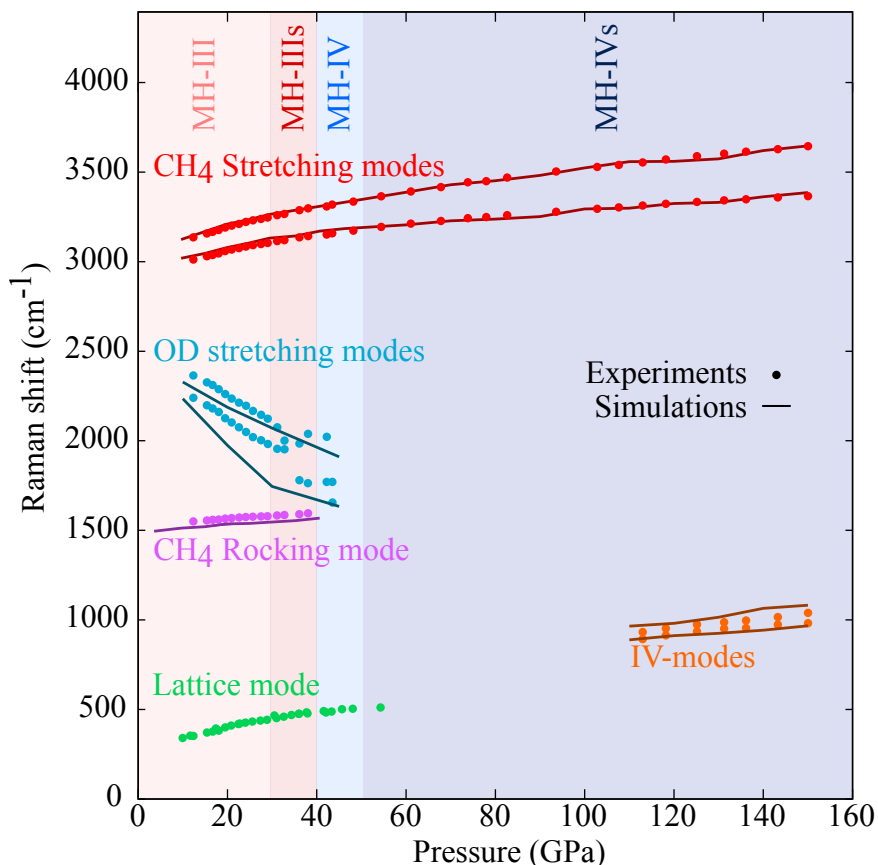


Figure 2.28. Experimental Raman frequencies (circles) and theoretical frequencies (lines) upon compression of the methane stretching and rocking modes, D_2O stretching modes, the lattice mode and the MH-IV characteristic modes (IV-modes). Theoretical frequency values were computed through the velocity time correlation functions as extracted from QTB trajectories, with the only exception of D_2O stretching modes, which were calculated in the harmonic crystal framework.

To summarize, we found a further high-pressure methane hydrate phase, the MH-IV, which follows the MH-III phase upon compression. This new phase is characterized by oxygen atoms arranged as in ice *Ih* and a significant deuterium tunneling or a symmetric hydrogen bond. The methane molecules are trapped in the ice-frame with a more symmetric orientational ordering as compared to MH-III. Several signatures of MH-IV was observed: (i) two new vibrational modes arise beyond 100GPa, (ii) a large broadening of the C-H stretching modes occurs at 80GPa and (iii) new X-ray peaks appears at 40GPa. The evolution of Raman spectra, as well as our theoretical analysis, confirm the stability of the structure up to, at least, 150GPa. At the transition, the hydrogen bonds slightly desymmetrize and give rise to another transition from MH-IV to MH-IVs with increasing pressure.

2.5 Transition description

In this section, we will describe the instability of the MH-III phase towards the MH-IV one, and characterize this transition. We will first describe the different atomic displacements this transition involves, and based on this analysis, we will analyze the different sources of instability in MH-III. Finally, minimum energy and free energy sampling along the transition will give access to a full characterization of the transition and reaction barrier.

2.5.1 Transition stages

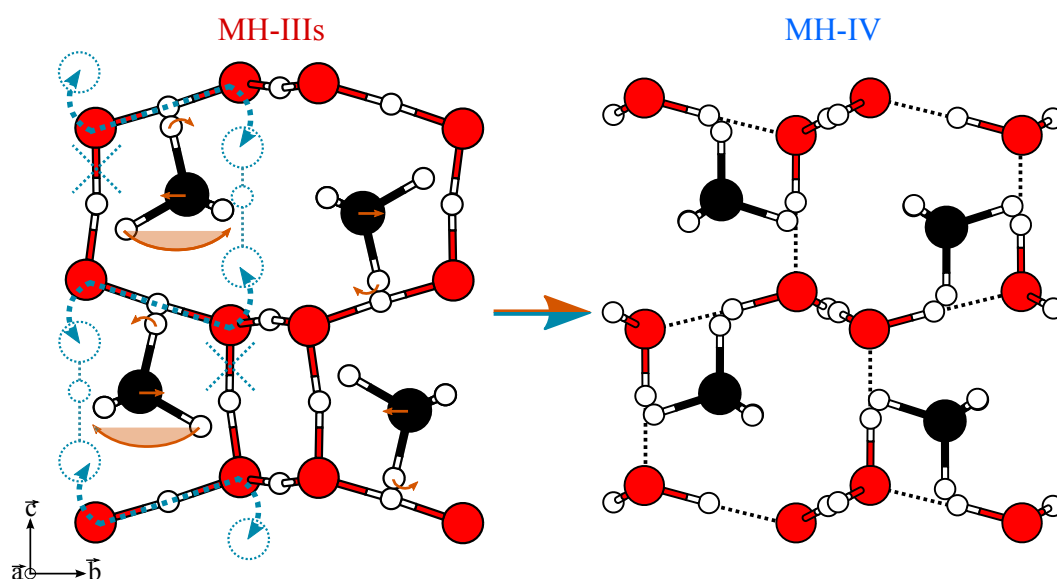


Figure 2.29. Description of the MH-III \rightarrow MH-IV transition: mainly two hydrogen bonds are impacted changing one of the oxygen atoms they were bonded to. Along with the hydrogen bond reorganization, the oxygen atoms involved are displaced along \vec{c} , forming 6-fold rings as in *ice-1h*. The methane molecules also present several rearrangements: a displacement along \vec{b} and a small rotation along \vec{a} lead to a perfect alignment of one of their C-H bond around \vec{c} ; a rotation of π around \vec{c} gives rise to the methane orientational ordering of MH-IV.

In Figure 2.29 we sketched the different atomic displacements required in MH-III phase to form MH-IV. As we can see, it requires both a structural reorganization of the hydrogen bonds as well as a significant change of the methane orientation. Interestingly, only half of the cell is mainly impacted along the transition. Indeed, while all the methane molecules require a small translation along \vec{b} and a small rotation along \vec{a} , only one half of them require a large rotation of π around \vec{c} . The second significant change concerns one half of the MH-III water network. In this part of the structure, both a reorganization of the hydrogen bonds and a displacement of the oxygen atoms are required. The rearrangement of the hydrogen bond occurs along \vec{c} , where the two hydrogen bonds forming 4-fold water rings break, while two other ones are created between oxygen atoms that were not bounded in phase III. These structural changes can be seen as a transfer of protons between O-O couples. Following the hydrogen bond rearrangement, the oxygen atoms are also displaced, in the same direction, in a “seesaw” mechanism. This induces the disappearance of the 4-fold and 8-fold water rings in favor of 6-fold water rings composing the water network of MH-IV and leads to hexagonal channels along both a and c directions, where the methane molecules are arranged.

These key displacements describing the transition reveal the essential mechanisms to be accounted for to understand the transition and the higher stability of the MH-IV phase under very high pressure. The organization of the methane molecule is not optimized within MH-III, which displays noticeable distortion of the molecules, thus decreasing the stability of the overall structure upon compression. Furthermore, the presence of 4-fold within the water network could lead to the instability of the structure by inducing an angular frustration of the water molecules as compared to their natural tetrahedral symmetry. Finally, the proton transfer between O-O pairs is one of the most important mechanism triggering the transition; it is, therefore, essential to account for nuclear quantum effects and describe the quantum spread of protons(deuterons) in order to have a faithful picture of the transition. Therefore, we first address the stability of the ice frame and related water rings. Then, we discuss a transition path as given by the minimum and free energy paths, and finally, we conclude on the importance of the NQE in this transition.

2.5.2 Stability of the ice frame

In order to distinguish the different contributions leading to the instability of MH-III, towards MH-IV, we compute the distinct contributions to their enthalpy at $T = 0\text{K}$. To do so, from the optimized methane hydrate structures, we removed either the methane molecules or the water network and calculated their energies by fixing the ion positions. This leads to an estimation of the water-water interaction energy $E_{(\text{H}_2\text{O}-\text{H}_2\text{O})}$ and of the methane-methane interaction energy $E_{(\text{CH}_4-\text{CH}_4)}$, to be compared with the full hydrate energy $E_{(\text{MH})}$. The water-methane interaction energy is computed through the difference: $E_{(\text{H}_2\text{O}-\text{CH}_4)} = E_{(\text{MH})} - E_{(\text{H}_2\text{O}-\text{H}_2\text{O})} - E_{(\text{CH}_4-\text{CH}_4)}$ while The term PV is added to the internal energies to recover the corresponding enthalpy $H_{(\text{MH})} = E_{(\text{MH})} + PV_{(\text{MH})}$ at $T = 0\text{K}$.

As shown in Figure 2.30, while the water-methane interaction energy largely contributes to the stability of MH-III, both the methane-methane and water-water interaction energies favor MH-IV. Although the sum of these energies (ΔE_{tot}) goes in the direction of the stability of MH-III, while taking into account the pressure energy term $P\Delta V$, the enthalpy difference (ΔH) gives the MH-IV denser structure stabler than MH-III.

As already discussed, to accurately describe the stability of MH-III, we have to take into account the entropy related to methane orientational disorder, which disappears beyond 25GPa. Indeed, we note that the locking-in of methane molecules should significantly contribute to reducing the stabilizing configurational entropy in the MH-III phase as pressure increases. To estimate its contribution, we consider methane molecules to be free rotors below 5GPa. Then for $5 < P < 25\text{GPa}$, we consider the disorder between the 4 (A_{\pm}, B_{\pm}) configurations to be equiprobable. Finally, these entropy terms have been used to estimate the Gibbs free energy (ΔG) presented in Figure 2.30.

From this analysis, we understand that the main instability of MH-III resides in the structural arrangement of the water network, which is the major contribution favoring MH-IV. Therefore, we analyzed the stability of the different 8-fold, 6-fold and 4-fold water rings present in MH-III in comparison with the 6-fold ones present in MH-IV (see Figure 2.31). To this purpose, we extracted water clusters by cutting the different water rings present in both structures and calculated their respective cohesive energy freezing the oxygen positions. By doing so, the O-O distances are reminiscent of the pressure in the original crystal, while the deuterons are free to rearrange.

As shown in Table 3, the energy analysis gives the MH-IV water rings more stable than the MH-III ones at any pressure. In particular, in accordance with other study of the H-bond angular flexibility,¹⁰⁰ 4-member rings, which are found in MH-III only, display the most important reduction of the cohesive energy with increasing pressure. This type of ring is thus the main

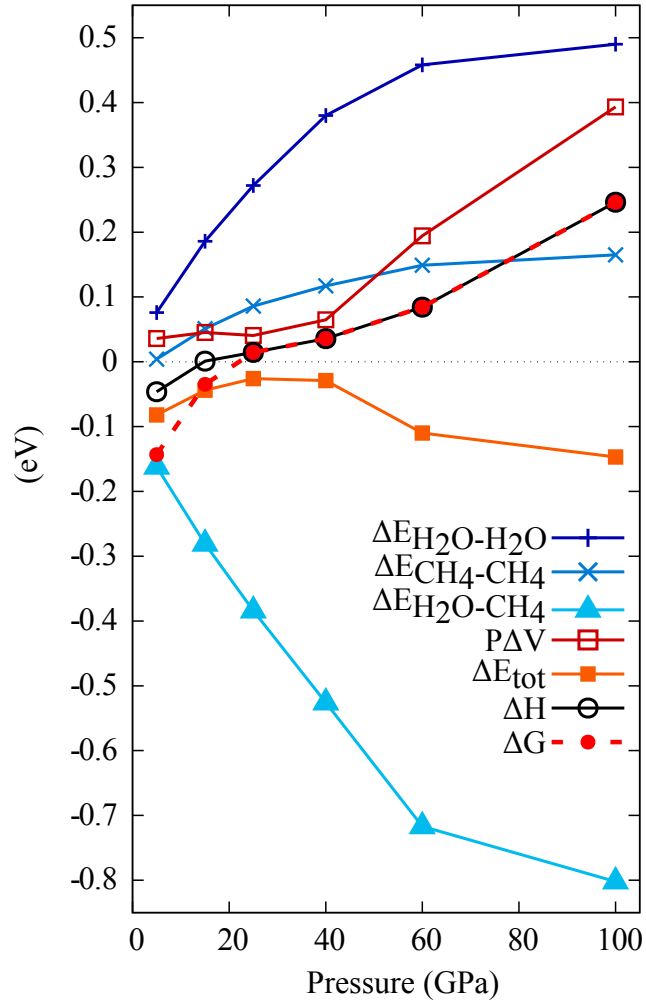


Figure 2.30. Difference of the ice-ice, methane-methane, ice-methane and PV energies between MH-III and MH-IV, for all contributions:

$$\Delta E \equiv E_{(\text{MH-III})} - E_{(\text{MH-IV})}$$

$$\Delta V \equiv V_{(\text{MH-III})} - V_{(\text{MH-IV})}$$

Negative (resp. positive) values therefore stabilize MH-III (resp. MH-IV) with respect to MH-IV (resp. MH-III). ΔG induces an estimate of the orientational disorder of CH_4 molecules in MH-III. Values are in eV per unit formula $\text{CH}_4:(\text{D}_2\text{O})_2$.

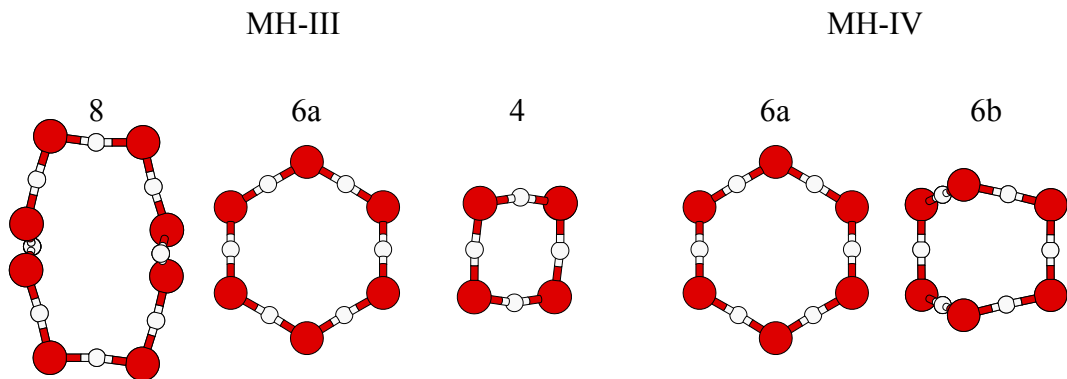


Figure 2.31. Sketch of the different water rings present in MH-III and MH-IV phases.

		Cohesive energy (eV/H ₂ O)		O-O distances (Å)	
		60GPa	20GPa	60GPa	20GPa
MH-III	Rings				
	4	0.177	0.348	2.32, 2.28	2.49, 2.46
	6a	0.181	0.363	2.29, 2.28	2.46, 2.44
	8	0.201	0.367	2.32, 2.29, 2.28	2.49, 2.46, 2.44
MH-IV	6a	0.270	0.391	2.37, 2.35, 2.33	2.56, 2.54, 2.51
	6b	0.262	0.380	2.37, 2.35, 2.33	2.56, 2.54, 2.51

Table 3. Cohesive energy and O-O distances of the different kinds of ice clusters: 4-member, 6-member, and 8-member rings (see Figure 2.31), in eV per H₂O molecule. The zero of the energy is that of an isolated water molecule. Second and third columns report the cohesive energy of ice rings obtained from MH-III and MH-IV, where O atoms are clamped at their values in the respective crystals (MH-III or MH-IV) at the indicated pressures (20 or 60GPa). The different 4, 6a, and 6b rings are sketched in Figure 2.31.

source of the MH-III instability upon compression. This effect is due to a significant angular frustration in 4-fold ice rings, where hydrogen bonds significantly deviate from linearity. In contrast, the MH-IV rings are more symmetric, and the O-O distances show less dispersion. Thus, they are closer to hexagonal symmetry and compatible with the high-pressure structure in which the methane molecules are stacked along an effective 3-fold symmetry axis.

On the other hand, as the O-O distances shorten under increasing pressure, the O-H covalent bond weakens, and the O...H hydrogen bond strengthens. However, the overall cohesive energy of the O-H...O configuration decreases when moving away from the optimal O-O distances in the fully optimized clusters. Therefore, in addition to the instability of the 4-fold and 8-fold water rings present in MH-III, the contraction of O-O distances favors proton(deuteron) tunneling and hydrogen bond symmetrization which triggers the transition toward MH-IV. A detailed analysis of the MH-III→MH-IV transition path provides relevant information on the sequence of transformations and the significance of nuclear quantum effects.

2.5.3 Transition path

In order to investigate both the transition stage sequence and the reaction barriers, first, we investigated the minimum energy path and then the free energy landscape. While the initial path was chosen from $T = 0$ K calculations employing the Nudged Elastic Band (NEB),¹⁰¹ it was refined through metadynamics using PIV as the metric for the Path CVs allowing a free energy sampling within the ($s - z$) space. As the transition only involves tiny changes in terms of lattice parameters and volume, we were able to study the transition at constant volume, taking an average value of the MH-III and MH-IV lattice parameters. This approximation was checked by monitoring the internal stress tensor at each point of the transition, giving a maximum error of ± 5 GPa out of 40GPa. Therefore, our approximation should provide a reasonably good estimate of the corresponding free energy barrier at constant pressure.

• Classical picture

As shown in Figure 2.32, the reaction path from MH-IV to MH-III provided by free energy sampling is complex and passes through several stages which display the different mechanisms that we mentioned earlier:

- Between $s = 1$ and $s = 1.6$ a rather large and deep free energy well is found and corresponds to structures within the MH-IV basin, which differ by hydrogen bond disorder.
- For $1.6 \leq s \leq 1.7$, the transition path shows a peculiar trend and varies mostly along

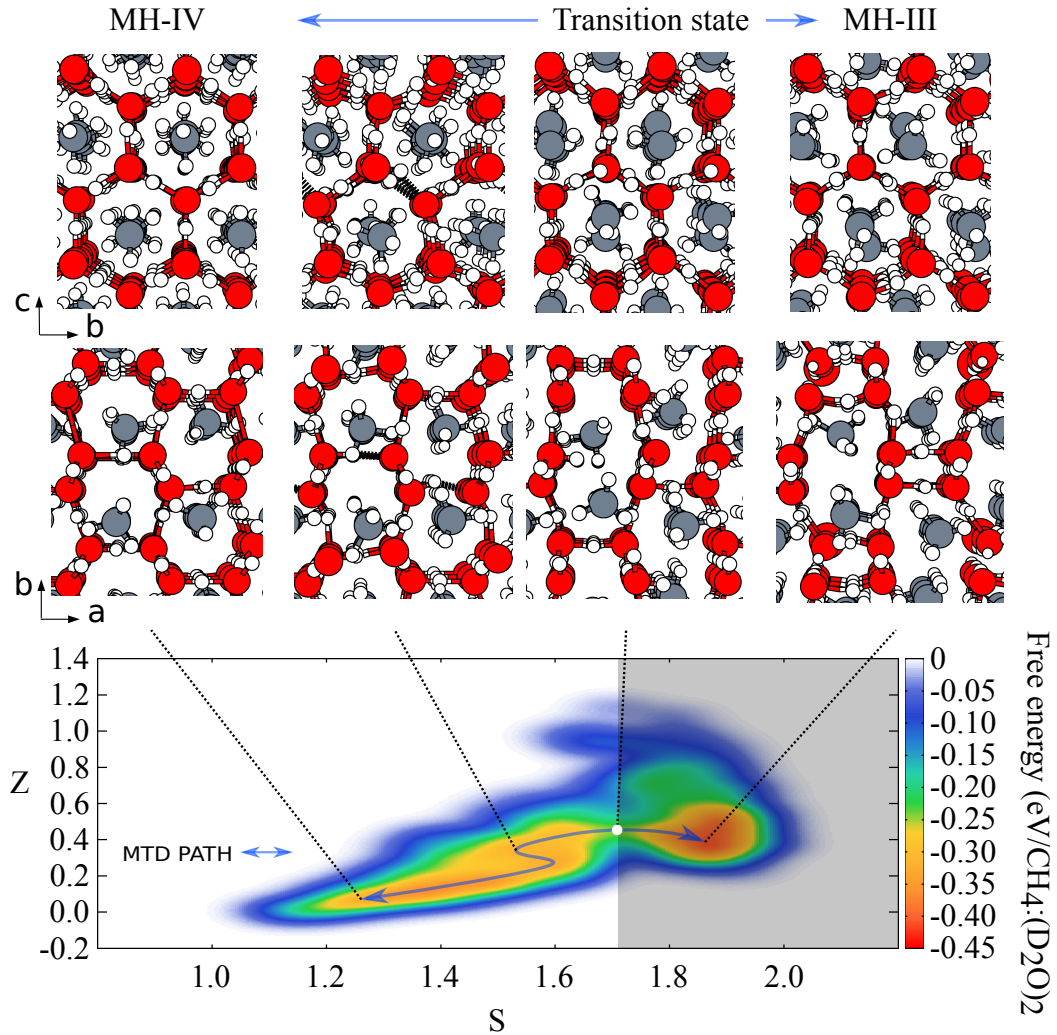


Figure 2.32. Free energy landscape of the (s, z) space as given by metadynamics. $s \approx 1.3, z \approx 0.1$: MH-IV; $s \approx 1.9, z \approx 0.4$: MH-III. The free energy values in the right part of the plot, shadowed in gray, are biased, in the absence of recrossing dynamics. The estimated barrier of reaction (white circle) is $E_r = 0.36$ eV per unit $\text{CH}_4:(\text{D}_2\text{O})_2$ formula.

z . This stage is characterized by the change of the orientation of half of the methane molecules. Methane ordering in MH-IV follows an A/B/A... stacking along \vec{b} , where A describes methane molecule oriented upward along \vec{z} and B downward along the same direction. Half of the methane molecules in this (s, z) region rotate, inducing an A/A/A ordering along \vec{b} . This is the onset of the typical MH-III methane ordering. This also happens along the NEB reaction coordinate but, according to metadynamics, the precise rotations of methane molecules are different and occur before any hydrogen bond breaking or formation, in contrast with the NEB sequence that we adopted as an input.

- At $s \approx 1.7, z \approx 0.4$, we find the transition state which is related to the “seesaw” displacement of the oxygen atoms and hydrogen bond reorganization. Following the methane rotation, some hydrogen bonds break down and other are formed, so that the ice network of MH-IV, which is formed by 6-fold rings, reorganizes. In Figure 2.32, we see the onset of 4-fold water rings induced by the shortening of the related oxygen atoms with the consequent formation of hydrogen bonds, while other O atoms move apart from each

other, breaking the related hydrogen bonds and beginning the formation of 8-fold rings, in a seesaw fashion.

- Finally, for $1.8 \leq s \leq 2.0$, we recover the MH-III phase by completing the hydrogen bond reorganization and the final reorientation of the methane molecules. The energy cost that is connected to those steps is small compared to the barrier, as the system moves within the MH-III basin.

According to our metadynamics simulations, the seesaw displacement, which involves the rearrangement of the O atoms as well as some hydrogen bond breaking and formation, is the key point and the broadest part of the free energy landscape along the transition. When adopting a classical picture for the nuclei, the corresponding MH-IV \rightarrow MH-III energy barrier amounts to $E_r = 0.36$ eV/unit formula.

• Quantum corrections

Whereas the displacement of the O atoms is little affected by NQE, the quantum deuteron delocalization plays a key role in the hydrogen bond breaking and reforming. As we have seen, this delocalization is enhanced by both the hydrogen bond symmetrization and the NQE. Therefore, we took into account both thermal and quantum effects in a perturbative way, by performing PIMD simulation along the MEP with fixed oxygen atomic positions, in order to estimate their importance on the transition barrier. In addition, we performed the same analysis taking into account thermal effects only, at 300K, via Langevin dynamics.

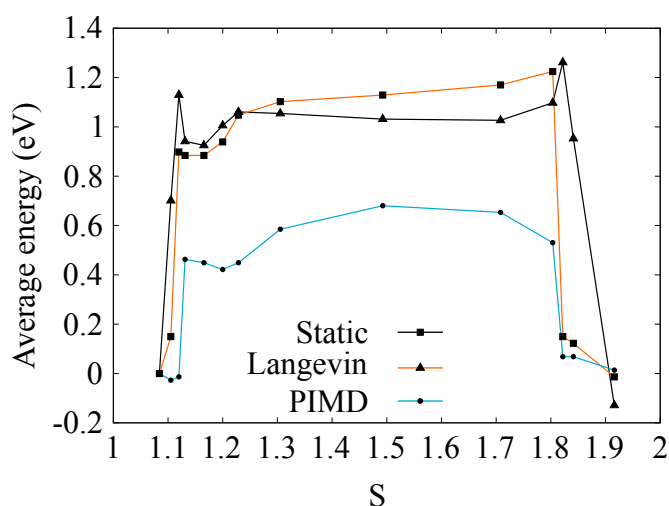


Figure 2.33. Average energy of the structure following the path given by NEB.

As shown in Figure 2.33, while the thermal effects are negligible, quantum corrections change the classical picture and significantly decrease the barriers corresponding to H-bond breaking, mainly because of deuterium quantum spread due to tunneling and zero-point energy. Indeed, within the quantum description, we observe a decrease of the energy barrier at the transition state of about 0.15 eV/unit formula. Thus, we expect the reaction barrier found with MTD simulations to be downshifted by roughly the same value at $E_r \approx 0.2$ eV/unit formula. This reveals the importance of NQE which therefore triggers the MH-III \rightarrow MH-IV transition, firstly by inducing the proton symmetrization and secondly allowing proton exchange between O-O pairs through quantum delocalization.

2.6 Conclusion

In this chapter, we studied the behavior of methane hydrate under high pressure in the [2-150] GPa range.

Firstly, we characterized the behavior of the methane molecules enclosed within the water frame. We observed their progressive orientational ordering and the locking-in of their rotation, which induces an enhancement of the guest-host interactions. Leading to distortion of the methane molecule tetrahedral symmetry, these interactions are also observed in the vibrational mode coupling occurring between the water network and the methane molecules. Therefore by increasing pressure, the system undergoes a transformation from pure methane-filled ice to a strongly interacting mixed molecular crystal.

Secondly, we investigated the expected hydrogen bond symmetrization transition from the MH-III to the MH-IIIs phase. This transition occurs around 40GPa within a broad pressure range due to non-equivalent O-O distances in MH-III. Interestingly, the hydrogen bond symmetrization occurring leading to the MH-IIIs phase differs from that in pure ice¹ in several respects. Indeed, due to the H(guest)-H(host) repulsive interaction, a noticeable delocalization of the protons normal to the O-O direction is found. Therefore, the widely-used one-dimensional model of the transition is not relevant for methane hydrates. While the normal delocalization weakens the hydrogen bond, the parallel delocalization strengthens it. The two effects roughly compensate each other, which results in almost null isotope effects, for H→D substitution. Therefore, rather than the absence of NQE in methane hydrate, we point out that they are more complex than those occurring in the ice VII→X transition. Both the balance between normal and parallel proton(deuteron) delocalization and host-guest strong interaction makes isotope effects negligible along the MH-III→MH-IIIs transition.

Thirdly, we discovered a new high-pressure methane hydrate phase: the MH-IV which follows the MH-III phase by increasing pressure. This phase has been found to become more stable than MH-III between 30 and 40GPa and remains stable up to at least 150GPa, which represents the highest pressure reached by any hydrate. MH-IV is characterized by a water network similar to the ice *Ih* wherein methane molecules are ordered. Several signatures of the latter confirm the presence of this phase under very high pressure. The MH-IV structure matches the experimental X-ray diffractogram, and our simulations confirm the presence of two new vibrational modes appearing beyond 100GPa along with a significant broadening of the C-H stretching modes starting at 80GPa observed in the Raman spectra. In addition, although the volume of the latter phase is slightly lower than MH-III, two of its lattice parameters increases, leading to an increase of the O-O distances within this plane. Therefore, the transition occurs from MH-IIIs, with symmetric hydrogen bonds, to MH-IV, whose ice skeleton is proton-disordered with massive proton tunneling. Upon further compression, another transition towards the MH-IVs phase takes place characterized by symmetric hydrogen bonds. Unexpectedly, the ice lattice could preserve the methane from dissociation, which has been observed in some¹⁰² but not all¹⁰³ Raman experiments on pressurized methane at ambient temperature and suggested by ab-initio calculations.¹⁰⁴

Finally, we studied the instability of the MH-III phase in favor of the MH-IV one, and we characterized this transition by investigating both the minimum energy path and the free energy landscape taking into account nuclear quantum effects. The main instability of the MH-III structure comes from the presence of 4-fold water cycles, methane repulsion, and a larger volume than the phase IV. In particular, the angular frustration of both water and methane molecules drastically increases the internal energy of MH-III upon compression. In addition, the hydrogen bond symmetrization of the latter structure weakens the water network. On the other hand, the complex transition path found by minimum and free energy sampling shows that

the hydrogen bond reorganization is the most significant contribution to the reaction barrier. Therefore, nuclear quantum effects, which are at the root of both hydrogen bond symmetrization and proton delocalization off the water rings, favor the destabilization of the MH-III phase and thus drastically lower the transition barrier and might induce proton diffusion within the water frame.

This study, therefore, illustrates how a relatively complex system can give rise to both subtle and often paradoxical quantum effects. The MH-III→MH-IV transition is a clear example where NQE not only trigger the phase transition (as in ice under pressure) but also cause a deep and complex rearrangement of the whole structure, including carbon and oxygen atoms, in contrast with the ice VII→X transition.

The Quantum equilibrium structure of sodium hydroxide

3.1 Introduction

Upon increasing temperature, sodium hydroxide displays several phase transitions before the melting point at 596K.¹⁰⁵ The protonated system evolves from an orthorhombic^{106,107} structure at low temperature toward a $P2_1/m$ monoclinic crystal at 500K and then a $Fm\bar{3}m$ cubic structure at 566K. In striking contrast, the deuterated system displays a first order,^{108,109} phase transition^{110,111} toward a monoclinic structure below 153K which is not observed in NaOH. This specific low-temperature structure is characterized by a proton-ordered antiferroelectric configuration of the O-H bonds. In addition, induced by a significant decrease of one lattice parameter, a formation of hydrogen bonds^{108,112} along that direction occurs by cooling the system. NaOH, as LiOH, does not adopt the hydrogen-bond structure that the chemically analog NaOD counterpart shows, as other hydroxides of heavy alkali metals (KOH, RbOH).^{107,113,114} This puzzling behavior cannot be explained on a classical basis and is purely quantum-induced. In addition to x-ray diffraction experiments,^{108,106} the low-temperature NaOD phase transition has been observed by a change in IR absorption¹¹⁵ and Raman spectra,¹⁰⁷ while both heat capacity,^{109,116} and dielectric measurements¹¹⁶ present anomalies at the transition temperature. Excess of heat capacity in NaOH as compared with NaOD has been related^{115,116} to the thermal population of quantum states connected to tunneling in an effective double-well potential.¹¹⁷

On the other hand, NaOH presents a phase transition upon compression toward a structure expected to be analogous to the low-temperature hydrogen-bonded NaOD phase.^{117,107} It has been suggested¹¹⁶ that H/D isotopic substitution could change the temperature-induced transition as observed in NaOD to a pressure-induced transition in NaOH.

While both transitions were observed experimentally,^{117,116,118,109,107} a microscopic description of the transition mechanism, and the associated nuclear quantum effects, are still lacking up to now. Therefore, in this study, we address this important isotope effect by the use of ab-initio simulations taking into account nuclear quantum effects within the path integral scheme. Firstly, we will demonstrate the importance of nuclear quantum effects in the description of the lattice parameters evolution upon increasing temperature. Secondly, we will focus on the specific ordering of proton and deuteron, which evolves at the transition. Finally, we will conclude by a comparison between the low-temperature transition occurring in NaOD and the pressure-induced one of NaOH.

Technical details of the simulations employed for this analysis can be found in the Appendix C.

3.2 Sodium hydroxide structure

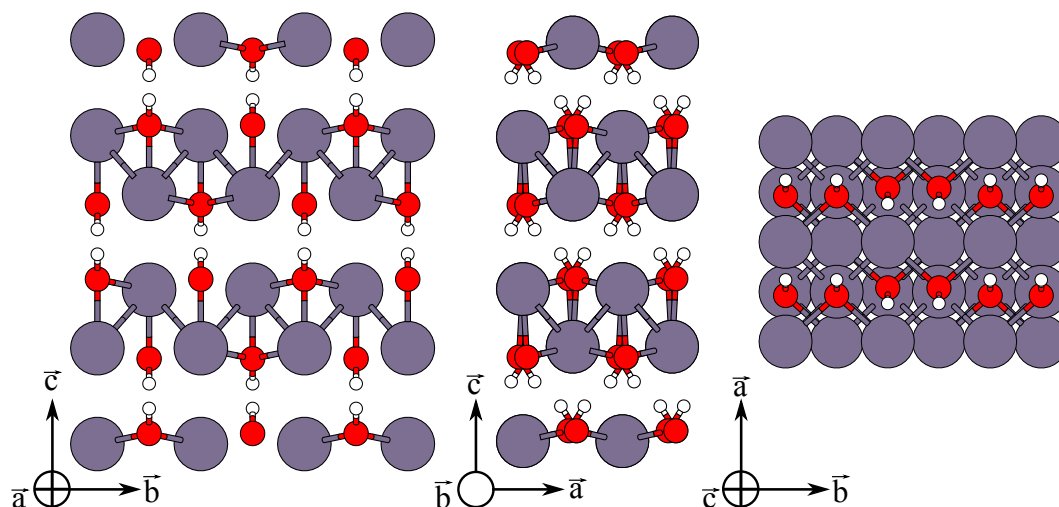


Figure 3.1. Sketch of the orthorhombic sodium hydroxide structure, in an antiferroelectric configuration.

As shown in Figure 3.1, sodium hydroxide is a layered structure composed of stacks of sodium, oxygen, and hydrogen atoms along lattice parameter c . At room temperature, the sodium hydroxide structure belongs to the $Bmmb$ space group while at low temperature, the NaOH system undergoes a phase transition toward a monoclinic structure of the $P2_1/a$ space group due to the particular deuteroxide group ordering. The latter structure can be approximately reproduced by the use of an orthorhombic supercell that we employed in both NaOH and NaOD simulations. In doing so, we neglect the small departure ($<1^\circ$) from the orthogonality between a and c of the monoclinic structure which induces rather small variations of the stress tensor, below our precision threshold of ± 0.5 kbar.

3.3 Quantum mechanical description of structural properties

As introduced earlier, the phase transition occurring in NaOH at 153K induces noticeable structural changes. Between the low-temperature monoclinic structure and the ambient-temperature orthorhombic crystal, the major structural change concerns the c lattice parameter. It drastically increases ($\sim 4.6\%$), as a result of the weakening of the inter-layer hydrogen bonds, as detailed later. Being a signature of the transition, this important structural change must be reproduced in our simulations to describe the transition mechanisms faithfully. As shown in Figure 3.2, lattice parameter c is correctly reproduced neither at low nor at ambient temperature when the nuclei are described as classical particles. Indeed, classical AIMD simulations, thermostatted through a Langevin equation, yield some major differences with respect to the experimental picture: first, the c parameter increases smoothly with temperature from the low-T to ambient-T phases (Figure 3.2.c); second, c differs as much as 10% from the experimental value, a much larger difference than what is usually provided by the GGA in related compound ($Mg(OH)_2, Ca(OH)_2, \dots$). Third, as expected, isotope effects are completely absent. Those facts suggest that the overall mechanism of the transition is missed within the classical frame for the nuclei. The quantum nature of nuclei (especially the lightest, H and D) indeed plays a crucial role. By volume optimization of the structures within the Path Integral scheme shown in Figure 3.1, we recover the experimental values of lattice parameters. They are almost constant within our temperature range for NaOH.

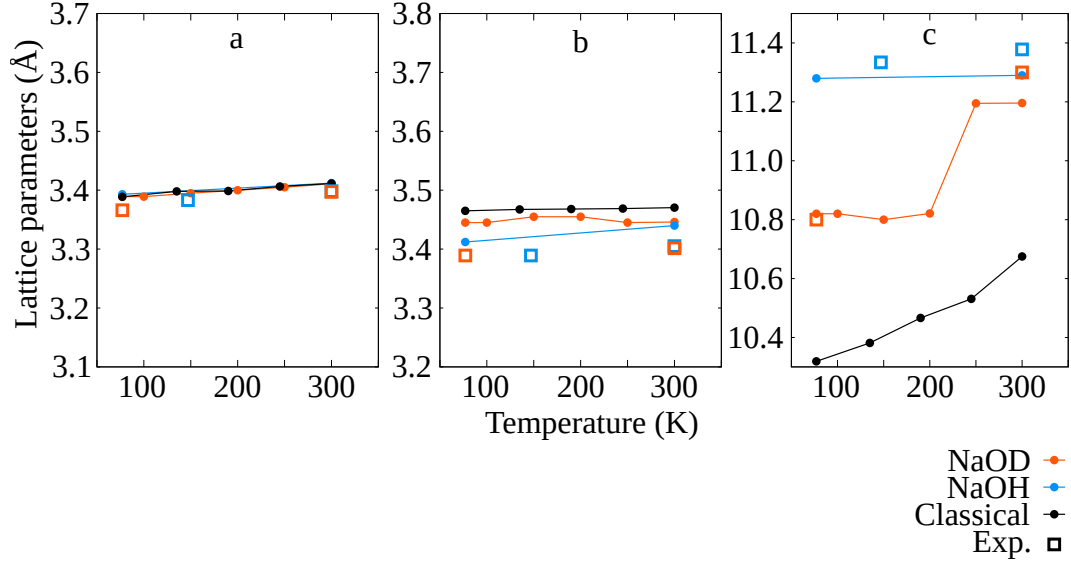


Figure 3.2. Lattice parameters evolution of NaOH and NaOD with increasing temperature as described by PIMD, or classical Langevin dynamics. Reported experimental values are taken from ref. [108] for NaOD and [119] for NaOH.

In contrast, NaOD displays a sharp increase of the lattice parameter c occurring at 200K. This demonstrates that the presence of nuclear quantum effects within this system is an essential factor to characterize the transition. As compared with the experimental value, the transition is up-shifted by about 100K, which can be traced back to a difference of 8meV of the reaction barrier, a rather precise value within our approximation. The change of the c lattice parameter in NaOD induces an increase of the O-O interlayer distance by about 4.4% which accompanies the deuteron order-to-disorder transition. Thus, this effect suggests a strong correlation between the O-O interlayer distance and the electric dipole orientation, which can be characterized by the O-H polar angles as presented in Figure 3.3, which is also related to the O-H bending vibrational mode.

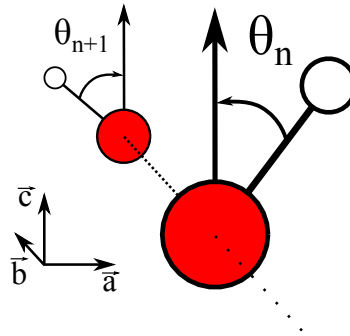


Figure 3.3. Sketch of successive θ O-H polar angles characterizing the proton ordering.

The latter assumption is confirmed by investigating the joint probability density $P(D_{OO}, \theta)$, of the O-O interlayer distance D_{OO} and the angle θ . As shown in Figure 3.5, a strong correlation is indeed observed between the two parameters in NaOD at 77K and is also found at higher temperatures and for the case of NaOH. As the O-O interlayer distance increases, the θ angle gets closer to 0° , namely a paraelectric disordered state.

Therefore, the cohesion between the NaO layers is expected to be the key parameter triggering

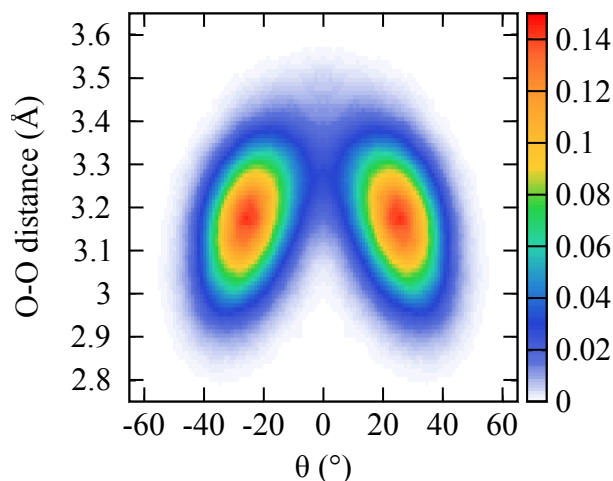


Figure 3.4. Probability distribution of the O-O interlayer distance as a function of the OH polar angle θ in NaOD at 77K.

the transition. In the low-temperature antiferroelectric phase of NaOD, this cohesion is mainly due to hydrogen bonding, whereas in NaOH at the same temperature, the O-H covalent bonds are in a paraelectric configuration, oriented predominantly along c , and the protons do not form hydrogen bonds with the atoms of the other layers leading to the observed increase of the c lattice parameter.

• Isotope effects on the hydrogen bonds

In this respect, nuclear quantum effects can either stabilize hydrogen bonds by enhancing the proton delocalization along the bond direction, related to the O-H stretching motion, or destabilize the hydrogen bonds due to the proton quantum delocalization in the normal direction, here linked to the O-H bending motion. The net balance between these two competing effects depends on the nature of the system. Michaelides¹²⁰ and coworkers have shown that NQE tend to strengthen strong H-bonds and to weaken the weak ones. Experimentally, the impact of NQE on the H-bond strength can be probed by measuring the change in the X-X distance upon H \rightarrow D substitution. In the context of H-bonded crystals and H-bonded ferroelectrics, this is known as the “Ubbelohde” effect:¹²¹ in systems with relatively strong H-bonds, an increase of the hydrogen bond length is observed upon deuteration, characteristic of a weakening of the bond (due to the decrease in zero-point energy). This corresponds to the positive (normal) Ubbelohde effect, whereas in more weakly-bonded systems, negative (inverse) Ubbelohde effect is observed with a shortening of the hydrogen bond length upon deuteration. In order to address this issue, we investigated the influence of the nuclear quantum effects on the quantum spread of the O-H covalent bonds and the quantum delocalization along the O-H bending motion.

Firstly, we focus on the O-H and O-D covalent bond lengths, shown in Figure 3.5.a. While simulating the NaOH system at 77K within the lattice parameters optimized for NaOD at the same temperature, we observe that although the mean value of the covalent O-H bonds is comparable for both systems, the spread of the protonated one is significantly larger. Secondly, as shown in Figure 3.5.b, the probability distribution $P(\theta)$ indicates the presence of a double-well potential along this coordinate, as suggested in the literature,¹¹⁶ whose equilibrium positions are closer one to the other in the protonated, not-optimized, system than in NaOD, with probability to overcome the barrier which is significantly larger in NaOH. While the more extensive quantum spread of the O-H covalent bond tends to strengthen the hydrogen bonds, the zero-point bending motion dominates, leading to an overall weaker H-bond in NaOH. Although in competition

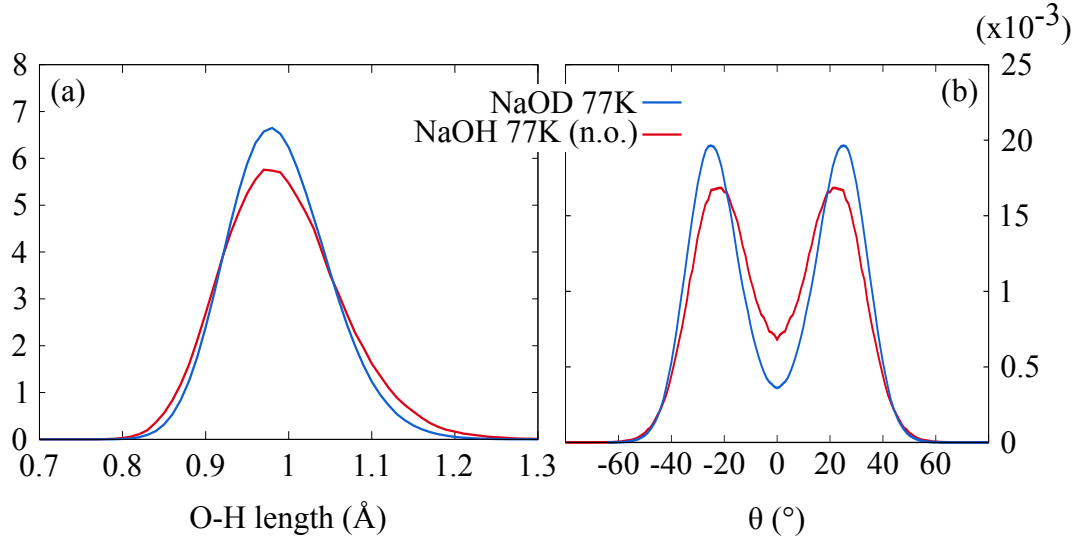


Figure 3.5. Probability distributions of the O-H length (a) and of the O-H polar angle θ (b). n.o. stands for “not optimized”, referring to the NaOH structure within the same lattice parameters as NaOD at 77K.

concerning H-bond stability, the combination of the two delocalization effects induces a pressure increase along the c direction. Indeed, the analysis of the stress tensor shows a significant isotope effect: the kinetic stress tensor difference $\sigma_{zz}^{NaOH} - \sigma_{zz}^{NaOD} \simeq 2GPa$ at the constrained NaOD lattice parameters at 77K. The overall pressure ($P = \text{Tr}\{\sigma\}$) of NaOH is around 1.5GPa, showing a clear tendency for NaOH to expand, essentially along the c axis. The interlayer distance stretch and destroys the weak hydrogen bonds in NaOD upon D \rightarrow H substitution. Therefore, the proton, because of its larger intrinsic quantum spread and zero-point motion, prevents the contraction of the inter-layer spacing and the formation of strong hydrogen bonds between them. The two phenomena are truly entangled and are at the root of the absence of transition for NaOH.

The quantum description of nuclei is central in these conclusions. Not only, nuclear quantum effects lead to profound structural changes, but they also impact the dynamical properties of the proton and deuteron which characterize the transition. Indeed, the latter can not be captured by harmonic zero-point corrections on top of a classical picture: the potential energy surface is highly anharmonic and thus rather sensitive to the mode amplitude. Only a dynamical, self-consistent treatment of the intrinsically quantum difference between protons and deuterons can provide a comprehensive picture of the NaOD transition and its absence for NaOH at ambient pressure. Therefore, in order to complete the picture of the low-temperature NaOD transition, we address in the following the NaOH and NaOD dielectric properties, related to the orientation of the O-H and O-D bonds, as well as their thermal behavior and response to external pressure.

3.4 Towards a dynamical paraelectric state

In the anti-ferroelectric configuration at low temperature (Figure 3.1), NaOD is characterized by slanted O-D bonds in the (a,c) plane, making a θ angle with the c axis. This configuration is characterized by successive θ_n angles which change sign while moving along the b axis, giving the specific alternating profile of OD groups as sketched in Figure 3.1. Each slanted OD group carries a dipole moment along a , which is globally null in the AFE configuration. The θ_n angles, therefore, appear as the natural order parameters to characterize the transition from the AFE to the para-electric (PE) configurations in NaOD. In particular, joint angle probability distribution $P(\theta_n, \theta_{n+1})$ of two adjacent OD groups along b allows the characterization of three classes of the

proton(deuteron) ordering: AFE (θ_n and θ_{n+1} are non-zero and have opposite sign), FE (θ_n and θ_{n+1} are non-zero and have same sign, either negative or positive), and PE (θ_n and θ_{n+1} are both centered at zero).

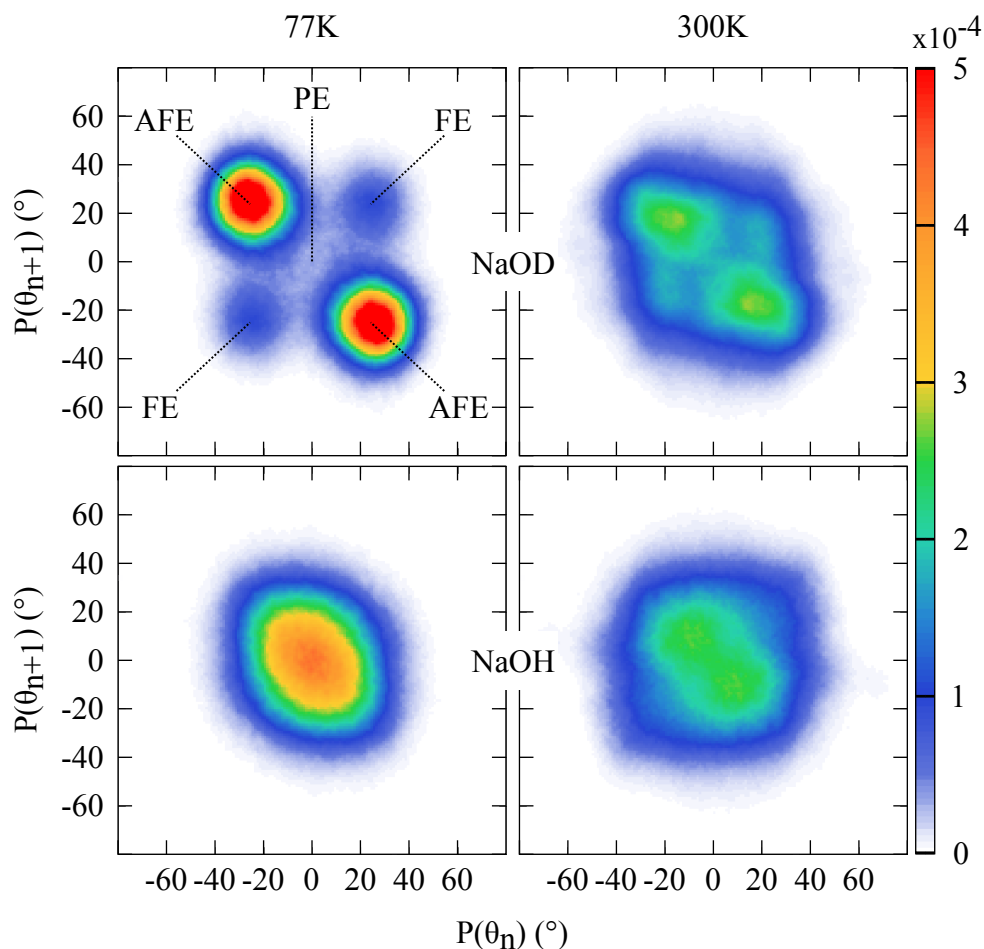


Figure 3.6. Probability distribution $P(\theta_n, \theta_{n+1})$ of adjacent O-D bonds describing the dielectric character of NaOD (top) and NaOH (bottom) at 77K (left) and 300K (right). AFE: anti-ferroelectric, FE: ferroelectric, and PE: paraelectric

As shown in Figure 3.6, at low temperature, NaOD displays the three classes. However, the $P(\theta_n, \theta_{n+1})$ maxima are clearly at $\theta_n = 25^\circ$, $\theta_{n+1} = -25^\circ$ or the reverse, that are characteristic of the AFE configuration. The FE configurations represent local maxima with a much lower probability as compared to the AFE state but at the same time the AFE \rightarrow FE \rightarrow AFE paths correspond to the lower barrier to overcome while passing from one AFE to the other AFE configuration. In contrast, the PE appears as a maximum along the path connecting either the two AFE or the two FE configurations. Therefore, in accordance with experimental results, at 77K, NaOD is in an almost permanent AFE state which is a more stable state than FE which here act as “bridge” configurations allowing the transfer between the two AFE configurations.

Significant changes are observed while increasing the temperature to 300K of NaOD. While the same topology is recovered, the FE maxima fade and the probability of the PE configuration, which is still a minimum, is appreciable. The AFE maxima are much lower than at $T=77K$ and get closer ($\theta_n = 15^\circ$, $\theta_{n+1} = -15^\circ$, or reverse), with a mild slope when approaching $\theta_n = -\theta_{n+1} \sim 0$. The angles are thus much less correlated than at low temperature, which is related to a significant weakening of the hydrogen bonds between opposite layers. The system indeed goes back and

forth through the AFE configurations, spending a non-negligible time in the PE configuration, which is typical of a deuteron-disordered configuration leading in this case to a dynamical PE configuration. Upon further increase of temperature, the PE minimum at $\theta_n = \theta_{n+1} = 0$ eventually becomes a maximum; however, this could appear at the onset of other structural transitions.¹¹⁷

The behavior of NaOH upon increasing temperature is very different as compared with NaOD. Indeed, while the probability distribution at low temperature displays almost isotropic distributions centered at $\theta_n = \theta_{n+1} \simeq 0^\circ$, at ambient temperature, the two AFE configurations become distinguishable, as very shallow minima, at $\theta_n = 8^\circ$, $\theta_{n+1} = -8^\circ$ or inverse. Counter-intuitively, the effective double-well potential wherein the proton lay recovers a barrier by increasing the temperature. This effect is due to the temperature-induced population of the excited state of the latter. Indeed, as shown in Figure 3.7, the probability distribution of the first excited states of

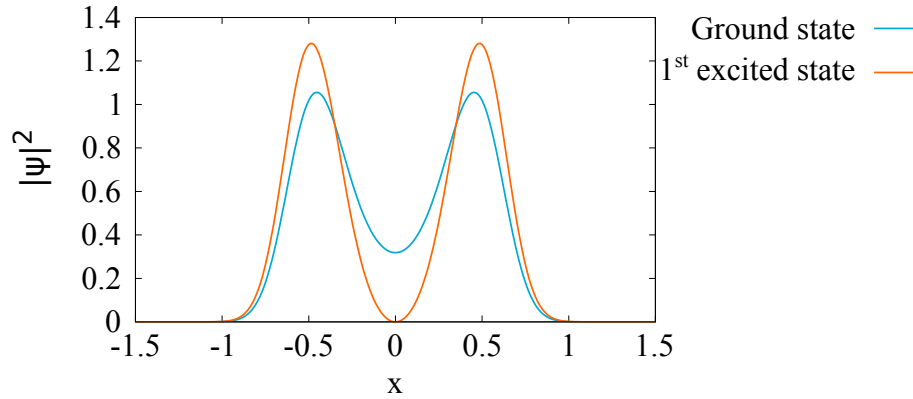


Figure 3.7. Probability density $|\Psi(x)|^2$ of the ground and first excited state of a particle within a one-dimensional double-well potential.

the generic example of a particle in a one-dimensional double-well is significantly lower at the barrier maximum as compared with the ground state. Therefore, by increasing the population of the first excited state, the overall probability density of the particle decreases at $x = 0$ leading, in the case of NaOH, to a transition from a static toward a dynamical PE state.

As suggested earlier, the topological difference between the two crystals is induced by the combination of the larger quantum spread for protons than deuterons and the significant zero-point energy effect on the O-H(D) bending mode: the typical proton angular spread in NaOH is $\Delta\theta \sim 40^\circ$, thus larger than the angular displacement that we computed by considering the proton as a purely classical particle. The para-electric state is thus stabilized by the zero-point quantum fluctuations, which is typical of quantum para-electrics.^{122,123} Interestingly, the distortion here impacts angular distributions, while in perovskites, such as SrTiO_3 , the order parameter is a linear displacement of Ti from the cell center.

• The bending zero-point motion

To complete the previous picture, we investigated the double-well potential along θ , characterizing the O-H bending motion. From the probability distribution $P(\theta)$, we computed an effective free energy $F(\theta) = -k_b T \log P(\theta)$, as a function of the azimuthal angle θ , as shown in Figure 3.8. Expectedly, we observe a free-energy barrier at $\theta = 0^\circ$ in NaOD at low and ambient temperature. This barrier, that includes quantum effects, decreases with temperature, from ~ 112 meV at 77K to ~ 31 meV at 300K. Therefore NaOD qualitatively behaves as a “classical” system: at low temperatures, the barrier is higher than the thermal energy and the system has two symmetric distorted states at $\theta = -20^\circ$ and $\theta = 20^\circ$ while it is comparable to thermal energy at ambient

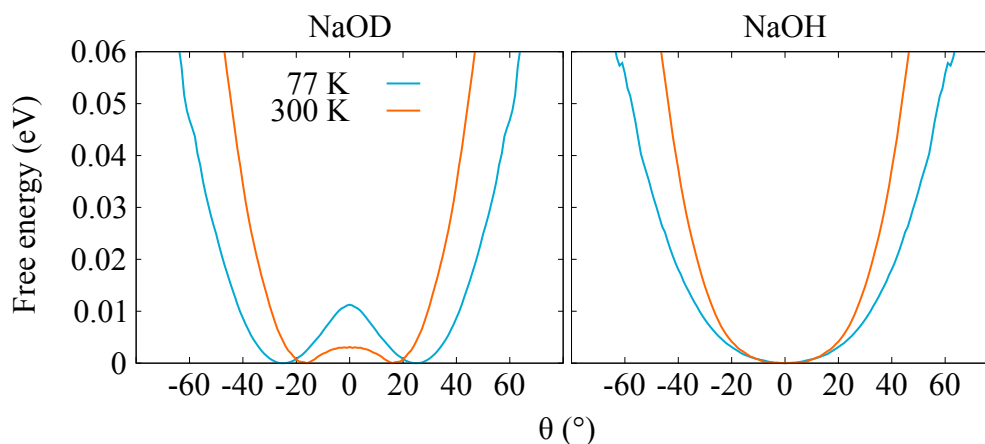


Figure 3.8. Free energy profile along the O-H θ angle of NaOD(left) and NaOH (right) at 77 and 300K.

temperature allowing the system to fluctuate around the symmetric $\theta = 0^\circ$ orientation. In contrast, the NaOH corresponding free-energy $F(\theta)$ shows a minimum at $\theta = 0^\circ$, at all temperatures. While at low temperature it is direct evidence of the observed static PE state, at ambient temperature it depicts both the large proton quantum spread ($> 20^\circ$), and the fact that both AFE states almost merge. Therefore, in addition to the destabilization of the H-bonds, the important zero-point contribution to the O-H bending motion also prevents NaOH from any symmetry-breaking transition.

3.5 From temperature- to pressure-induced transition

In agreement with experimental results,^{116,109} our simulations show that, at ambient pressure, NaOH remains a quantum para-electric at all temperatures. However, a pressure-induced transition¹¹⁷ is found to occur at 1GPa toward a structure expected to be analogous to the deuterated system at low temperature. Nonetheless, as the positions of hydrogen atoms could not be refined, the high-pressure, ambient temperature, structure of NaOH is not fully resolved, but compressibility measurements suggest the formation of H-bonds upon compression of the structure. In this context, it was suggested¹¹⁶ that the protonation of NaOD could change the temperature-induced transition of NaOD toward a pressure-induced one in NaOH. This assumption is strengthened by the resulting pressure of 1.5GPa, that we found for NaOH constrained at the NaOD lattice parameter at 77K.

Therefore, we simulated the NaOH system at 300K for pressure of 1GPa in a similar orthorhombic cell with lattice parameters optimized taking into account nuclear quantum effects. As shown in Table 4, the resulting parameters well agree with the experimental ones. This optimization mainly impacts the lattice parameter c , which almost recovers the value of the NaOD structure at 77K. As shown in Figure 3.9.a, the probability distribution $P(\theta_n, \theta_{n+1})$ brings out the AFE

	a	b	c
Exp.	3.338	3.338	10.843
Theory	3.373	3.403	10.899

Table 4. Optimized lattice parameters of NaOH at 300K and 1GPa. Experimental data from ref. [117].

character of NaOH at ambient temperature and 1GPa. The two maxima are indeed recovered at $\theta_n = 25^\circ$, $\theta_{n+1} = -25^\circ$ or reverse, similarly to NaOD at 77K. Moreover, the FE configurations are

NaOH at P=1GPa and T=300K

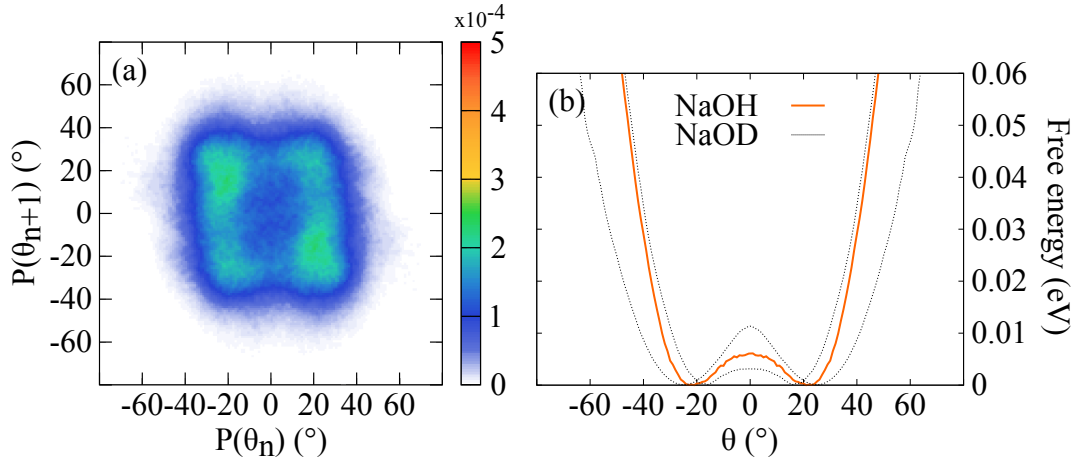


Figure 3.9. (a) Probability distribution $P(\theta_n, \theta_{n+1})$ of adjacent O-D bonds describing the dielectric character of NaOH (b) Free energy profile along the O-H θ angle. Probability distribution for NaOD at 77K and 300K are reported for comparison. Results are provided by simulations of NaOH ambient temperature and pressure of 1GPa.

less negligible than in the latter case but still represent “bridge” states between the two AFE configurations while PE state, although non-negligible, represents a probability minimum. In Figure 3.9.b, we report the free energy $F(\theta)$, where we observe the pressure-induced double-well formation occurring in NaOH upon compression. Its barrier height as high as 60 meV (thus almost $3k_bT$) is found at $\theta = 0^\circ$, which can be overcome by thermal fluctuations. These two analyses, therefore depict the NaOH at ambient temperature and 1GPa to be analogous to NaOD at 77K and ambient pressure. Indeed, both the stabler AFE state and the double-well potential along θ , characteristic of the latter structure, are recovered by increasing the pressure in NaOH at 300K. Thus, it confirms that the protonation of NaOD change the significant thermodynamical parameter determining the transition from temperature to pressure.

However, the similarity between AFE and FE states probabilities in NaOH at high pressure suggests that at lower pressure or for higher temperatures both state could be equivalently stable, leading to a disordered FE or AFE. Further studies are therefore needed in order to determine the competition between the two configurations and to see whether the temperature increase or a pressure decrease below 1GPa might induce proton disordering. In this respect, accurate measurements of the evolution of lattice parameter c under decreasing pressure and increasing temperature would be highly desirable. As found for NaOD at ambient pressure and varying temperature, the discontinuous evolution of the lattice parameter c that governs the interlayer distance might indeed reveal the existence of a phase transition.

3.6 Conclusion

In this study, we addressed the low temperature phase transition occurring in NaOD at 153K, not observed in NaOH. Among other effects, the phase transition is characterized by a significant increase (+5%) of the c lattice parameter in NaOD. This change is completely absent upon protonation, as the structural parameters of NaOH are well continuous in the 77-300K temperature range. This dramatic isotope effect cannot be reproduced if nuclear quantum effects are not taken into account. Both the quantum delocalization of protons as well as the zero point motion prevent the protonated system from displaying such a transition.

At low temperature, NaOD is a hydrogen-bonded structure which presents a proton-ordered anti-ferroelectric configuration. Analysis of the O-H bond orientation shows that along with the more stable anti-ferroelectric states, ferroelectric ones are also present at 77K. The latter configurations act as “bridge” states allowing the switching from one anti-ferroelectric state to the other while direct transition through a para-electric configuration is hindered. Beyond the transition temperature, this mechanism is thermally activated, leading to a dynamical para-electric deuteron disordering.

In contrast, while the NaOH system displays a static quantum para-electric state at low temperature, at ambient temperature, due to the increasing population of the excited state along the bending degree of freedom, a transition toward a dynamical quantum para-electric configuration, analogous to the observed one in NaOD at the same temperature, occurs.

Both AFE and FE configurations imply the formation of weak inter-layer hydrogen bonds, which are broken in paraelectric configurations, whatever their nature (classical, static quantum or dynamical quantum). As a consequence, the interlayer spacing significantly increases in PE configurations, which explains the abrupt change of the c lattice parameter upon the AFE→PE transition in NaOD. The change of the macroscopic parameter c is intimately related with quantum delocalization, which in the case of NaOH is strong enough to destroy the weak hydrogen bonds between the layers and to lower the barrier of the effective double-well potential along the OH bending motion. This transition is therefore recovered while submitting the system to an external pressure of 1GPa, thus confirming that H/D isotopic substitution in sodium hydroxide changes the temperature-induced phase transition in NaOD toward a pressure-induced one in NaOH.

Conclusion

From Planck's discovery in the XIX century up to today, the study of quantum mechanics led to non-intuitive and unexpected effects within the various fields which were explored. In this study, we have seen that nuclear quantum effects in condensed matter do not escape that rule.

The description of quantum systems remains a delicate subject. Solving Schrödinger's equation for real physical systems with many degrees of freedom is not feasible in practice. Approximation and smart modelization are thus required to account for the quantum nature of particles. While standard reference methods to describe the electronic part (DFT, Quantum Monte-Carlo,...) already exist, the nuclei have been considered as being classical particles for a long time. This thesis is dedicated to cases of light and/or cold nuclei for which the classical approximation is no more valid. In this framework, Feynman's Path integrals formalism, and Langevin equation based QTB were employed to successfully address both the quantum statistical distribution and the dynamical properties of the hydrogen atom present in three different hydrated environments.

One of the well-known examples of nuclear quantum effects consequence is the pressure-induced transition of ice, from VII to the X phase, occurring around 60 GPa. While investigating this system with PIMD simulations, Benoit et al.¹ brought out the importance of both zero-point energy and tunneling of the proton in the mechanism of the hydrogen-bond symmetrization. Accounting for nuclear quantum effects yields a downshift of the transition pressure. This effect is characteristic of a particle in a double-well potential for which the barrier is indeed lowered by pressure as the oxygen atoms move closer to one another: the effect of the zero-point energy then becomes quite important. This situation is also present in the case under study in this thesis, but important conclusions one can draw from this work are the variety and subtlety of effects in which nuclear quantum effects are involved.

This complexity not only arises from nuclear quantum effects but is also entangled with other phenomena of different kinds. Specifically, we saw how the competition between nuclear quantum and thermal effects could drastically influence the diffusion mechanism in Brucite minerals. This layered hydroxide structure was expected to display a proton diffusion mechanism involving two processes: a reorientation, and dissociation of the hydroxyl groups. While thermal fluctuations mainly drive the former, the latter depends strongly on the proton nuclear quantum effects. Thermal study⁵⁰ of this diffusion mechanism concluded that the reorientation motion enhanced by the temperature was the proton diffusion limiting factor. In contrast, we saw that, in analogy with the hydrogen bond symmetrization, the pressure tends to increase the dissociation process while reorientation is hindered. While both mechanisms are required for long-range proton diffusion within this structure, these two opposite effects lead to a pressure sweet spot, with the highest probability for proton diffusion. In this pressure range, the potential barriers are reachable with thermal fluctuations or nuclear quantum effects for the reorientation and dissociation processes, respectively.

In addition, the different delocalization induced by nuclear quantum effects can, in some cases, be in competition. In compounds where hydrogen bonds coexist with other bonding types in anisotropic environments, the simple and elegant picture of a proton in a one-dimensional double-well is no more able to account for the complex phenomena that we observed. The competition between quantum delocalization along non-equivalent directions, on one side, and between quantum and classical degrees of freedom, on the other side, could even lead to a small overall impact of nuclear quantum effects. This was seen in our study of methane hydrate under high pressure (CH₄-H₂O). This is indeed composed of methane molecules confined within

channels formed by hydrogen-bonded water structure close to the ice phase *I_h*. Therefore, a hydrogen bond symmetrization transition was expected to occur as pressure is increased, and in comparison with the ice VII \rightarrow X transition, both nuclear quantum effects and H/D isotopic substitution were expected to be significant. Remarkably, isotope effects are negligible, and the pressure downshift of the transition induced by nuclear quantum effects is relatively low while quantum delocalization is present. From our analysis, we concluded that the larger normal delocalization with respect to the hydrogen bond of the protonated water frame as compared with both the deuterated system and the pure ice induced disappearance of isotope effects and the lowering of the nuclear quantum effects contribution. This is a prototypical case where the usual one-dimensional double-well approximation cannot explain the observed phenomena.

On the other hand, nuclear quantum effects can be an essential factor to consider while investigating phase transitions. Not only can they facilitate the overcome of reaction barriers as we have seen for the ice, but they can also trigger them. In particular, along with experimental results, the important proton quantum delocalization of the water network in the MH-III structure led us to the discovery of a new methane hydrate high-pressure phase, the MH-IV, stable at pressures never reached by any hydrate before. The study of this transition demonstrated the importance of nuclear quantum effects while the thermal contribution was negligible. This transition was indeed found to be triggered by both the water structure destabilization through hydrogen bond symmetrization, and proton exchange between O-O pairs. Both mechanisms represent the main contributions to the transition path between MH-III and MH-IV; nuclear quantum effects roughly half the classical barrier that includes purely thermal fluctuations.

Quantum delocalization in layered hydroxides gives rise to non-intuitive and sometimes contrasting effects. Indeed, for both Brucite ($\text{Mg}(\text{OH})_2$) and sodium hydroxide (NaOH) the classical picture of point particle does not allow the understanding of mechanism involving quantum indetermination. In Brucite minerals, layers of hydrogen atoms are facing each other and get closer with increasing pressure. In a classical picture, this mechanism leads to two distinguishable space probability distributions which eventually merge. However, within the quantum picture, at some point, the proton quantum spread is of the order of the distance separating these two distributions, leading to indiscernible layers and thus a “quantum” two-dimensional plane of protons.

The changes induced by the quantum representation of nuclei is even more apparent in sodium hydroxide, where the quantum delocalization of protons drives the structural properties. Indeed, while a classical description gives rise to wrong lattice parameters, a quantum description allows recovering experimental results of this system. In this study, we showed that this important difference was due to both the proton kinetic energy contribution to the pressure, along with the quantum spread of nuclei. Therefore, this effect can be understood by the large volume occupied by hydrogen atoms within the structure, through quantum delocalization, in addition to the zero-point bending motion causing H-bond breaking. Although a deuteron is also a light particle and should be considered as a quantum particle, the effective volume it occupies and the related zero-point energies are less than for a proton. In sodium hydroxide, this induces an important isotope effect. While a phase transition from a deuteron ordered antiferroelectric structure toward a deuteron disorder para-electric phase is observed as the temperature is increased above 153K, the protonated structure only presents a proton disordered para-electric structure. We demonstrate the correlation of this transition with the structural properties of the system. Indeed, as the deuteron and proton disordered phase share the same lattice parameters, the deuteron structure shows a significant increase of one lattice parameter at the transition. The important quantum delocalization and the zero-point contribution to the kinetic energy of the protonated system hinder the transition that occurs in NaOD. This result was then confirmed by increasing the pressure in the protonated system, recovering a proton-ordered anti-ferroelectric

state analogous to the low-temperature deuterated system.

Throughout our investigations, we have seen how the quantum nature of nuclei deeply impacted both structural description and dynamical properties of the complex systems we studied. In the light of these findings, it appears that nuclear quantum effects are fundamental properties which should be accounted for in theoretical simulations of many physical systems. Taking into account the quantum nature of nuclei in condensed matter systems can pave the way for a better understanding of physical properties and lead to the discovery of new structures.

Appendices

The simulation results present in this thesis were carried out within the NVT ensemble. They were performed using the Quantum Espresso package¹²⁴ for the DFT calculations while nuclear quantum effects were taken into account through QTB with a local modified version of Quantum Espresso and PIMD simulations via the i-Pi¹²⁵ interface. These methods allowed to compute approximate velocity-velocity time correlation functions, and correct quantum distributions respectively.

The electronic structure and atomic forces were described within the GGA approximation and the interaction between ionic cores and valence electrons were described by ultra-soft pseudo-potentials provided by Quantum Espresso. Lattice parameters were obtained through systematic volume relaxation of the system ensuring isotropic stress tensors for each pressure and the typical duration time of the simulations was **30 ps** with a time step of **0.48 fs**.

In the following section, we provide the technical requirement, and set of parameters, to reproduce the simulations of the different systems investigated in this thesis.

A.1 Computational details

Both Brucite ($\text{Mg}(\text{OH})_2$) and Portlandite ($\text{Ca}(\text{OH})_2$) were simulated by the use of a tetragonal supercell containing 15 atoms with 4 magnesium (or calcium), 8 oxygen and 8 hydrogen atoms. The following pseudo-potentials were used with a plane-waves expansion cutoff of $E_{\text{cut}} = 50\text{Ry}$ ensuring total energy convergence.

- Mg.pw91-np-van.UPF
- Ca.pw91-nsp-van.UPF
- O.pw91-van_ak.UPF
- H.pw91-van_ak.UPF

The Brillouin zone was sampled with a $2 \times 2 \times 2$ k-point grid.

On top of DFT calculations, we used PIMD-based RPMD approach to account for the nuclear

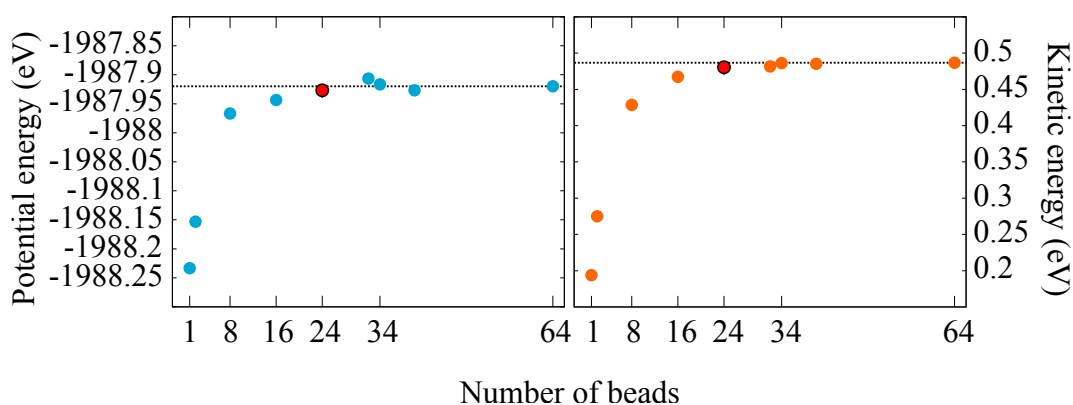


Figure A.1. Convergence of the potential and kinetic energies as a function of the number of beads within RPMD simulations of Brucite.

quantum effects. The number of beads in the RPMD simulations was set to 24 and checked to provide convergence of kinetic and potential energies as shown in Figure A.1.

B.1 Computational details

For each phase, the samples consist of 4 methane and 8 water molecules ($\text{CH}_4:(\text{D}_2\text{O})_2$) in an orthorhombic crystal cell. Finite-size effects on equilibrium configurations were systematically checked. We added a Van der Waals correction via the semi-empirical D2 scheme by Grimme,¹²⁶ in order to better reproduce the experimental lattice constants and compressibility of MH-III. The resulting lattice parameters were chosen to provide an isotropic stress tensor, at all simulated pressures.

The following pseudo-potentials were used with a plane-waves expansion cutoff of $E_{\text{cut}} = 40\text{Ry}$.

- O.pbe-rrkjus.UPF
- H.pbe-rrkjus.UPF
- C.pbe-rrkjus.UPF

The Brillouin zone was sampled with a $2 \times 1 \times 2$ k-point grid.

Both QTB and PIMD approaches were used to describe dynamical properties and quantum

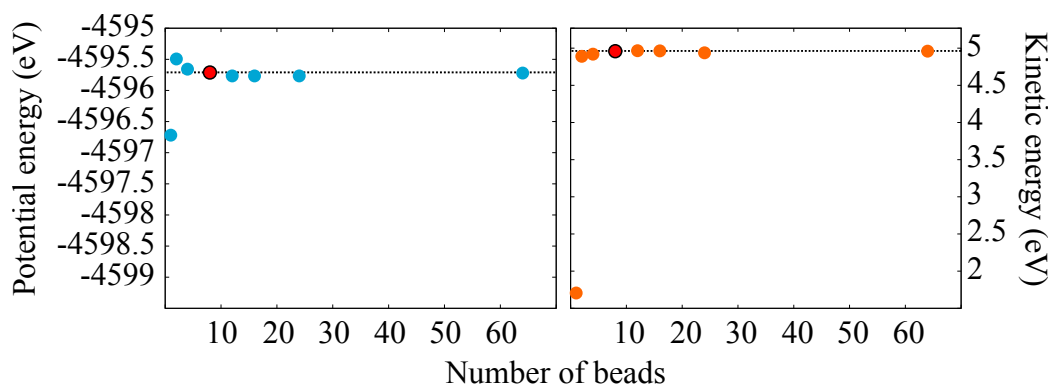


Figure B.1. Convergence of the potential and kinetic energies as a function of the number of beads within RPMD simulations of Methane Hydrate.

distributions. Specifically, we used the Path Integral Generalized Langevin Equation Thermostat (PIGLT)^{127,128} method which, as other methods such as PI-QTB,^{129,130} allows a faster convergence, thus reducing the required number of replicas. The friction coefficient used in QTB

simulations was set to $\gamma = 10\text{THz}$ and the number of beads in the PIGLET simulations was set to **8** and checked to provide convergence of kinetic and potential energies as shown in Figure B.1.

B.2 Methane rotation characterization

In order to characterize the methane rotational motions, we extract this motion while removing other internal vibrational modes by the use of the following method.

Let \vec{r}_ℓ^m , $\ell \in [1, n]$ designates the unit vectors that point to the atoms in the molecule (i. e. a bond vector), this in the molecular frame. These are constants that define the molecule.

Now the molecule may have undergone a rotation in the laboratory (or crystal) frame. The vectors that point to the atom now write:

$$\vec{r}_\ell^{lab}(t) = \mathbf{R}^{-1}(t)\vec{r}_\ell^m = \mathbf{R}^T(t)\vec{r}_\ell^m$$

where $\mathbf{R}(t)$ is the rotational matrix that goes from the laboratory frame to the molecular frame (and $\mathbf{R}^{-1} = \mathbf{R}^T$ since it is a rotation matrix). This matrix can be defined through Euler angles (ϕ, θ, ψ) or quaternions $\mathbf{Q} = (q_0, q_1, q_2, q_3)$ with $q_0^2 + q_1^2 + q_2^2 + q_3^2 = 1$, and

$$q_0 = \cos \frac{\theta}{2} \cos \frac{\phi + \psi}{2} \quad (\text{B.2.1})$$

$$q_1 = \sin \frac{\theta}{2} \cos \frac{\phi - \psi}{2} \quad (\text{B.2.2})$$

$$q_2 = \sin \frac{\theta}{2} \sin \frac{\phi - \psi}{2} \quad (\text{B.2.3})$$

$$q_3 = \cos \frac{\theta}{2} \sin \frac{\phi + \psi}{2} \quad (\text{B.2.4})$$

$$(\text{B.2.5})$$

while

$$\mathbf{R} = \begin{pmatrix} q_0^2 + q_1^2 - q_2^2 - q_3^2 & 2(q_1q_2 + q_0q_3) & 2(q_1q_3 - q_0q_2) \\ 2(q_1q_2 - q_0q_3) & q_0^2 - q_1^2 + q_2^2 - q_3^2 & 2(q_2q_3 + q_0q_1) \\ 2(q_1q_3 + q_0q_2) & 2(q_2q_3 - q_0q_1) & q_0^2 - q_1^2 - q_2^2 + q_3^2 \end{pmatrix}$$

One can also carry out the same operation at time $t + dt$ where dt is presumably small:

$$\vec{r}_\ell^{lab}(t + dt) = \mathbf{R}^T(t + dt)\vec{r}_\ell^m$$

Assuming one can extract the quaternions at time t , $\mathbf{Q}(t)$, and $t + dt$, $\mathbf{Q}(t + dt)$, one can estimate the time derivative $\dot{\mathbf{Q}}$ thereof.

We now have the relation:

$$\dot{\mathbf{Q}} = \frac{1}{2} \begin{pmatrix} q_0 & -q_1 & -q_2 & -q_3 \\ q_1 & q_0 & -q_3 & q_2 \\ q_2 & q_3 & q_0 & -q_1 \\ q_3 & -q_2 & q_1 & q_0 \end{pmatrix} \begin{pmatrix} 0 \\ \omega_x^m \\ \omega_y^m \\ \omega_z^m \end{pmatrix}$$

where, of course $|\dot{\mathbf{Q}}|^2 = 2(\dot{q}_0q_0 + \dot{q}_1q_1 + \dot{q}_2q_2 + \dot{q}_3q_3) = 0$, which can be easily checked from the above equation. This is thus, in practise, a (3×3) system which yields the rotation vector in the molecular frame:

$$\vec{\Omega}^m = \begin{pmatrix} \omega_x^m \\ \omega_y^m \\ \omega_z^m \end{pmatrix}$$

where ω_x^m , ω_y^m and ω_z^m are the angular velocities. The same vector can be obtained in the laboratory frame:

$$\vec{\Omega}^{lab} = \mathbf{R}^T \vec{\Omega}^m$$

Finally, in order to extract the quaternions from a molecular dynamics configuration, one may write:

$$\chi^2 = \sum_{\ell} \left(\vec{r}_{\ell}(t) - \mathbf{R}^T \vec{r}_{\ell}^m \right)^2 + \lambda (q_0^2 + q_1^2 + q_2^2 + q_3^2 - 1)$$

where $\vec{r}_{\ell}(t)$ are the units vectors associated with each atom, and λ is a Lagrange multiplier that ensures the quaternion normalization.

We want to find a set of quaternions for χ^2 to be at a minimum, thus:

$$\begin{cases} \frac{\partial \chi^2}{\partial q_{\alpha}} = 2 \sum_{\ell} \left(\mathbf{R}^T \vec{r}_{\ell}^m - \vec{r}_{\ell}(t) \right) \frac{\partial \left(\mathbf{R}^T \vec{r}_{\ell}^m \right)}{\partial q_{\alpha}} + 2\lambda q_{\alpha} = 0, & \alpha \in [0, 3] \\ \frac{\partial \chi^2}{\partial \lambda} = q_0^2 + q_1^2 + q_2^2 + q_3^2 - 1 = 0 \end{cases}$$

a set of non-linear equations to be solved by standard Newton-style methods or through a direct minimization of χ^2 via a conjugate-gradient method.

C.1 Computational details

NaOD and NaOH were simulated by the use of an orthorhombic supercell containing 24 atoms with 8 sodium, 8 oxygen and 8 hydrogen (or deuterium) atoms.

The following pseudo-potentials were used with a plane-waves expansion cutoff of $E_{\text{cut}} = 40\text{Ry}$.

- Na.pbe-mt_fhi.UPF
- O.pbe-rrkjus.UPF
- H.pbe-rrkjus.UPF

The Brillouin zone was sampled with a $2 \times 1 \times 3$ k-point grid.

On top of DFT calculations, we used PIMD-based PIGLET approach to account for the nuclear quantum effects. The number of beads in the PIGLET simulations was set to 24 and checked to provide convergence of kinetic and potential energies as shown in Figure C.1.

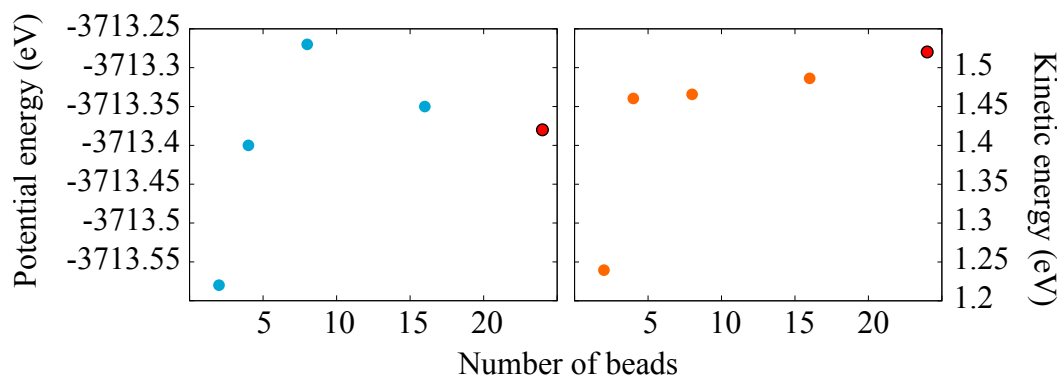


Figure C.1. Convergence of the potential and kinetic energies as a function of the number of beads within RPMD simulations of Brucite.

C.2 Volume optimization

As the pressure could trigger the transition observed in NaOD and NaOH, we performed simulations within the NVT ensemble in order to prevent artificial transition that a barostat could induce. Therefore, a systematic optimization of the volume was performed at different temperatures in order to obtain lattice parameters at an hydrostatic pressure as provided in Table 5.

T	NaOD			NaOH			NaOH (1GPa)		
	a	b	c	a	b	c	a	b	c
77K	3.389	3.445	10.819	3.393	3.412	11.280			
100K	3.389	3.445	10.819						
150K	3.395	3.455	10.800						
200K	3.400	3.455	10.821						
250K	3.405	3.445	11.195						
300K	3.411	3.446	11.196	3.412	3.440	11.290	3.373	3.403	10.899

Table 5. Optimized lattice parameters of NaOH and NaOD.

Communications

The studies carried out during this thesis gave rise to the following communications:

• **Articles:**

Published or accepted

- Sofiane Schaack, Philippe Depondt, and Fabio Finocchi. “H-bond symmetrization in high pressure methane hydrate”. *Journal of Physics: Conference Series*. Vol. 1136. 1. IOP Publishing. 2018, p. 012018
- Sofiane Schaack et al. “Orientational Ordering, Locking-in, and Distortion of CH₄ Molecules in Methane Hydrate III under High Pressure”. *The Journal of Physical Chemistry C* 122.20 (2018), pp. 11159–11166
- Sofiane Schaack et al. “Observation of methane filled hexagonal ice stable up to 150 GPa”. *PNAS* (Accepted)

Submitted or to be submitted

- Sofiane Schaack et al. “Quantum induced proton diffusion in Brucite minerals under high-pressure” (Submitted)
- Sofiane Schaack et al. “How methane hydrate recovers at very high pressure the hexagonal ice structure.” (Submitted)
- Sofiane Schaack et al. “The quantum equilibrium structure of NaOH.” (To be submitted)
- Mathieu Moog et al. “Unsupervised Exploration of MoS₂Nanoclusters Configurations : Structures, Energetics, and Electronic Properties” (Submitted)

• **Conferences:**

- IUPAP XXIX Conference on Computational Physics, 2017, Paris-France
- 56th EHPRG Meeting, 2018, Aveiro-Portugal

Bibliography

- [1] M. Benoit, D. Marx, and M. Parrinello. “Tunnelling and zero-point motion in high-pressure ice”. *Nature* 392.6673 (1998), p. 258.
- [2] Mark Tuckerman. *Statistical mechanics: theory and molecular simulation*. Oxford university press, 2010.
- [3] Laroche M. Hayoun M. Greffet J-J. Dammak H. Chalopin Y. “Quantum thermal bath for molecular dynamics simulation”. *Phys. Rev. Lett.* 103.19 ((2009)), p. 190601.
- [4] Y. Bronstein et al. “Quantum-driven phase transition in ice described via an efficient Langevin approach”. *Phys. Rev. B* 89.21 (2014), p. 214101.
- [5] Yael Bronstein, Philippe Depondt, and Fabio Finocchi. “Thermal and nuclear quantum effects in the hydrogen bond dynamical symmetrization phase transition of δ -AlOOH”. *European Journal of Mineralogy* 29.3 (2017), pp. 385–395.
- [6] Yael Bronstein et al. “Quantum versus classical protons in pure and salty ice under pressure”. *Physical Review B* 93.2 (2016), p. 024104.
- [7] Florent Calvo et al. “Vibrational spectra of polyatomic molecules assisted by quantum thermal baths”. *Phys. Chem. Chem. Phys.* 14 (2012), p. 10503.
- [8] Noëlle Pottier. *Physique statistique hors d'équilibre-Processus irréversibles linéaires*. EDP Sciences, 2012.
- [9] Nicolas Borghini. *Topics in Nonequilibrium Physics*. [Online; accessed 05-May-2019]. 2016. URL: <https://www.physik.uni-bielefeld.de/~borghini/Teaching/Nonequilibrium/Nonequilibrium.pdf>.
- [10] Fabio Finocchi. *Density Functional Theory for beginners*. [Online; accessed 05-May-2019]. 2011. URL: http://www.attacalite.com/wp-content/uploads/2017/04/pdf_DFT4beginners.pdf.
- [11] Rep Kubo. “The fluctuation-dissipation theorem”. *Reports on progress in physics* 29.1 (1966), p. 255.
- [12] Ryogo Kubo. “Statistical-Mechanical Theory of Irreversible Processes. I. General Theory and Simple Applications to Magnetic and Conduction Problems”. *Journal of the Physical Society of Japan* 12.6 (1957), pp. 570–586.
- [13] T. A. Callen H. B.; Welton. “Irreversibility and Generalized Noise”. *Phys. Rev.* 83 (1 1951), p. 34.
- [14] Walter Kohn and Lu Jeu Sham. “Self-consistent equations including exchange and correlation effects”. *Physical review* 140.4A (1965), A1133.
- [15] Pierre Hohenberg and Walter Kohn. “Inhomogeneous electron gas”. *Physical review* 136.3B (1964), B864.
- [16] Robert Brown. *The miscellaneous botanical works of Robert Brown*. Vol. 27. Ray society, 1866.

- [17] Albert Einstein. “Über die von der molekularkinetischen Theorie der Wärme geforderte Bewegung von in ruhenden Flüssigkeiten suspendierten Teilchen”. *Annalen der physik* 322.8 (1905), pp. 549–560.
- [18] Jean Perrin. *Translated from "Annales de chimie et de Physique 8ème série, septembre 1909" : Brownian movement and molecular reality*. Courier Corporation, 2013.
- [19] Paul Langevin. *On the theory of Brownian motion*. 1908.
- [20] Etienne Mangaud et al. “The fluctuation-dissipation theorem as a diagnosis and cure for zero-point energy leakage in quantum thermal bath simulations”. *Journal of chemical theory and computation* (2019).
- [21] Sofiane Schaack, Philippe Depondt, and Fabio Finocchi. “H-bond symmetrization in high pressure methane hydrate”. *Journal of Physics: Conference Series*. Vol. 1136. 1. IOP Publishing. 2018, p. 012018.
- [22] Sofiane Schaack et al. “Orientational Ordering, Locking-in, and Distortion of CH₄ Molecules in Methane Hydrate III under High Pressure”. *The Journal of Physical Chemistry C* 122.20 (2018), pp. 11159–11166.
- [23] Paul AM Dirac. “The Lagrangian in quantum mechanics”. *Feynman’s Thesis—A New Approach To Quantum Theory*. World Scientific, 2005, pp. 111–119.
- [24] Richard Phillips Feynman. “Space-time approach to non-relativistic quantum mechanics”. *Feynman’s Thesis—A New Approach To Quantum Theory*. World Scientific, 2005, pp. 71–109.
- [25] R. Gilmore. “Baker-Campbell-Hausdorff formulas”. *Journal of Mathematical Physics* 15.12 (1974), pp. 2090–2092.
- [26] Jianshu Cao and Gregory A Voth. “The formulation of quantum statistical mechanics based on the Feynman path centroid density. IV. Algorithms for centroid molecular dynamics”. *The Journal of chemical physics* 101.7 (1994), pp. 6168–6183.
- [27] D.E. Craig I. R.; Manolopoulos. “Quantum statistics and classical mechanics: Real time correlation functions from ring polymer molecular dynamics”. *J. Chem. Phys.* 121 (2004), p. 3368.
- [28] Timothy JH Hele et al. “Boltzmann-conserving classical dynamics in quantum time-correlation functions: “Matsubara dynamics””. *The Journal of chemical physics* 142.13 (2015), p. 134103.
- [29] Michele Parrinello and Aneesur Rahman. “Study of an F center in molten KCl”. *The Journal of chemical physics* 80.2 (1984), pp. 860–867.
- [30] Alessandro Laio and Michele Parrinello. “Escaping free-energy minima”. *Proceedings of the National Academy of Sciences* 99.20 (2002), pp. 12562–12566.
- [31] Davide Branduardi, Francesco Luigi Gervasio, and Michele Parrinello. “From A to B in free energy space”. *The Journal of Chemical Physics* 126.5 (2007), p. 054103. eprint: <https://doi.org/10.1063/1.2432340>. URL: <https://doi.org/10.1063/1.2432340>.
- [32] S. Pipolo et al. “Navigating at Will on the Water Phase Diagram”. *Phys. Rev. Lett.* 119 (24 2017), p. 245701. URL: <https://link.aps.org/doi/10.1103/PhysRevLett.119.245701>.
- [33] Hichem Dammak et al. “Isotope effects in lithium hydride and lithium deuteride crystals by molecular dynamics simulations”. *J. Phys. Condens. Matter* 24.43 (2012), p. 435402.

- [34] K. C. Liang and A. S. Nowick. “High-temperature protonic conduction in mixed perovskite ceramics”. *Solid State Ionics* 61 (1993), pp. 77–81.
- [35] Mariana Rossi, Michele Ceriotti, and David E. Manolopoulos. “Nuclear Quantum Effects in H^+ and OH^- Diffusion along Confined Water Wires”. *The Journal of Physical Chemistry Letters* 7 (15 2016), pp. 3001–3007.
- [36] Asami Sano-Furukawa et al. “Direct observation of symmetrization of hydrogen bond in δ -AlOOH under mantle conditions using neutron diffraction”. *Scientific Reports* 8 (1 2018), p. 15520.
- [37] Changjun Zhang and Angelos Michaelides. “Quantum nuclear effects on the location of hydrogen above and below the palladium (100) surface”. *Surface Science* 605 (2011), pp. 689–694.
- [38] Mohammad Wahiduzzaman, Christian F. J. Walther, and Thomas Heine. “Hydrogen adsorption in metal-organic frameworks: The role of nuclear quantum effects”. *The Journal of Chemical Physics* 141.6 (2014), p. 064708.
- [39] A. B. Yaroslavstev. “Proton conduction of inorganic hydrates”. *Russian Chemical Reviews* 63 (1994), pp. 429–435.
- [40] Gianfranco Ulian and Giovanni Valdrè. “Equation of state and second-order elastic constants of portlandite $Ca(OH)_2$ and brucite $Mg(OH)_2$ ”. *Physics and Chemistry of Minerals* 46.2 (2019), pp. 101–117.
- [41] Simone Raugei, Pier Luigi Silvestrelli, and Michele Parrinello. “Pressure-induced frustration and disorder in $Mg(OH)_2$ and $Ca(OH)_2$ ”. *Physical Review Letters* 83.11 (1999), p. 2222.
- [42] Mainak Mookherjee and Lars Stixrude. “High-pressure proton disorder in brucite”. *American Mineralogist* 91.1 (2006), pp. 127–134.
- [43] John B Parise et al. “Pressure-induced H bonding: Neutron diffraction study of brucite, $Mg(OH)_2$, to 9.3 GPa”. *American Mineralogist* 79.1 (1994), pp. 193–196.
- [44] M Catti et al. “Static compression and H disorder in brucite, $Mg(OH)_2$, to 11 GPa: a powder neutron diffraction study”. *Physics and Chemistry of Minerals* 22.3 (1995), pp. 200–206.
- [45] Hongwu Xu et al. “In situ neutron diffraction study of deuterated portlandite $Ca(OD)_2$ at high pressure and temperature”. *Physics and Chemistry of Minerals* 34.4 (2007), pp. 223–232.
- [46] MB Kruger, Q Williams, and R Jeanloz. “Vibrational spectra of $Mg(OH)_2$ and $Ca(OH)_2$ under pressure”. *The Journal of Chemical Physics* 91.10 (1989), pp. 5910–5915.
- [47] Thomas S Duffy et al. “High-pressure phase transition in brucite, $Mg(OH)_2$ ”. *American Mineralogist* 80.3-4 (1995), pp. 222–230.
- [48] Andreas Hermann and Mainak Mookherjee. “High-pressure phase of brucite stable at Earth’s mantle transition zone and lower mantle conditions”. *Proceedings of the National Academy of Sciences* 113.49 (2016), pp. 13971–13976.
- [49] Yingwei Fei and Ho-Kwang Mao. “Static compression of $Mg(OH)_2$ to 78 GPa at high temperature and constraints on the equation of state of fluid H_2O ”. *Journal of Geophysical Research: Solid Earth* 98.B7 (1993), pp. 11875–11884.
- [50] Romain Dupuis et al. “Quantum Nuclear Dynamics of Protons within Layered Hydroxides at High Pressure”. *Scientific reports* 7.1 (2017), p. 4842.

- [51] C.J. Theodor de Grotthuss. "Sur la décomposition de l'eau et des corps qu'elle tient en dissolution à l'aide de l'électricité galvanique". *Ann. Chim.* 58 (1806), 54–73.
- [52] Charles Meade and Raymond Jeanloz. "Static compression of $\text{Ca}(\text{OH})_2$ at room temperature: observations of amorphization and equation of state measurements to 10.7 GPa". *Geophysical Research Letters* 17.8 (1990), pp. 1157–1160.
- [53] T Nagai, T Hattori, and T Yamanaka. "Compression mechanism of brucite: An investigation by structural refinement under pressure". *American Mineralogist* 85.5-6 (2000), pp. 760–764.
- [54] George A Jeffrey. "Water structure in organic hydrates". *Acc. Chem. Res.* 2.11 (1969), pp. 344–352.
- [55] Jr E Dendy Sloan and Carolyn Koh. *Clathrate hydrates of natural gases*. CRC press, 2007.
- [56] Ayhan Demirbas. *Methane gas hydrate: as a natural gas source*. Springer, 2010.
- [57] M. Mitarai et al. "Surfactant Effects on the Crystal Growth of Clathrate Hydrate at the Interface of Water and Hydrophobic-Guest Liquid". *Cryst. Growth Des.* 15 (2015), p. 812.
- [58] P. M. Naullage, A. A. Bertolazzo, and V. Molinero. "How do surfactants control the agglomeration of clathrate hydrates?" *ACS Cent. Sci.* 5 (2019), p. 428.
- [59] Marco Lauricella et al. "Methane Clathrate Hydrate Nucleation Mechanism by Advanced Molecular Simulations". *The Journal of Physical Chemistry C* 118 (Oct. 2014), pp. 22847–22857.
- [60] Flavio Romano and Francesco Sciortino. "Patterning symmetry in the rational design of colloidal crystals". *Nature communications* 3 (2012), p. 975.
- [61] E Dendy Sloan and Carolyn A Koh. "Clathrate Hydrates of Natural Gases (3rd ed.)" *CRC Press* 119 (2008).
- [62] Wendy L Mao and Ho-kwang Mao. "Hydrogen storage in molecular compounds". *PNAS* 101.3 (2004), pp. 708–710.
- [63] Viktor V Struzhkin et al. "Hydrogen storage in molecular clathrates". *Chem. rev.* 107.10 (2007), pp. 4133–4151.
- [64] Peter G Brewer et al. "Direct experiments on the ocean disposal of fossil fuel CO_2 ". *Science* 284.5416 (1999), pp. 943–945.
- [65] JS Loveday et al. "Transition from cage clathrate to filled ice: the structure of methane hydrate III". *Phys. Rev. Lett.* 87.21 (2001), p. 215501.
- [66] JS Loveday and RJ Nelmes. "High-pressure gas hydrates". *Phys. Chem. Chem. Phys.* 10.7 (2008), pp. 937–950.
- [67] JS Loveday et al. "Stable methane hydrate above 2 GPa and the source of Titan's atmospheric methane". *Nature* 410.6829 (2001), pp. 661–663.
- [68] H Hirai et al. "Structural changes in gas hydrates and existence of a filled ice structure of methane hydrate above 40 GPa". *J. Phys. Chem. Sol.* 65 (2004), p. 1555.
- [69] Wendy L Mao, Carolyn A Koh, and E Dendy Sloan. "Clathrate hydrates under pressure". *Physics Today* 60 (2007), p. 42.
- [70] Leonardo Del Rosso, Milva Celli, and Lorenzo Ulivi. "New porous water ice metastable at atmospheric pressure obtained by emptying a hydrogen-filled ice". *Nature communications* 7 (2016), p. 13394.

- [71] Daniel M Amos et al. “A Chiral Gas–Hydrate Structure Common to the Carbon Dioxide–Water and Hydrogen–Water Systems”. *J. Phys. Chem. Lett.* 8.17 (2017), pp. 4295–4299.
- [72] JS Loveday and RJ Nelmes. “High-pressure neutron diffraction and models of Titan”. *High Pres. Res.* 23.1-2 (2003), pp. 41–47.
- [73] Amanda Mascarelli. “A sleeping giant?” *Nat. rep. Clim. Change* (2009), pp. 46–49.
- [74] Hisako Hirai et al. “Methane hydrate, amoeba or a sponge made of water molecules”. *Chem. Phys. Lett.* 325.5 (2000), pp. 490–498.
- [75] A Witze. “Mars methane hunt comes up empty, flummoxing scientists.” *Nature* 568.7751 (2019), p. 153.
- [76] Olivier Mosis et al. “Methane clathrates in the solar system”. *Astrobiology* 15.4 (2015), p. 308.
- [77] Hisako Hirai et al. “Methane hydrate behavior under high pressure”. *J. Phys. Chem. B* 104.7 (2000), pp. 1429–1433.
- [78] H Hirai et al. “High-pressure structures of methane hydrate observed up to 8 GPa at room temperature”. *J. Chem. Phys.* 115.15 (2001), pp. 7066–7070.
- [79] H Hirai et al. “Retention of filled ice structure of methane hydrate up to 42 GPa”. *Phys. Rev. B* 68.17 (2003), p. 172102.
- [80] Hisako Hirai et al. “Stabilizing of methane hydrate and transition to a new high-pressure structure at 40 GPa”. *Amer. Mineral.* 91 (2006), p. 826.
- [81] S-I. Machida et al. “A new high-pressure structure of methane hydrate surviving to 86GPa and its implications for the interiors of giant icy planets”. *Phys. Earth Planet. Inter.* 155.1 (2006), pp. 170–176.
- [82] I-Ming Chou et al. “Transformations in methane hydrates”. *PNAS* 97.25 (2000), pp. 13484–13487.
- [83] Tatsuya Kumazaki et al. “Single-crystal growth of the high-pressure phase II of methane hydrate and its Raman scattering study”. *Chem. Phys. Lett.* 388.1 (2004), pp. 18–22.
- [84] Hiroyasu Shimizu et al. “In situ observations of high-pressure phase transformations in a synthetic methane hydrate”. *J. Phys. Chem. B* 106.1 (2002), pp. 30–33.
- [85] S-I. Machida et al. “Raman spectra of methane hydrate up to 86 GPa”. *Phys. Chem. Miner.* 34.1 (2007), pp. 31–35.
- [86] Mathieu Choukroun et al. “Stability of methane clathrate hydrates under pressure: Influence on outgassing processes of methane on Titan”. *Icarus* 205.2 (2010), pp. 581–593.
- [87] Takehiko Tanaka et al. “Phase changes of filled ice Ih methane hydrate under low temperature and high pressure”. *J. Chem. Phys.* 139 (2013), p. 104701.
- [88] DD Klug et al. “Hydrogen-bond dynamics and Fermi resonance in high-pressure methane filled ice”. *J. Chem. Phys.* 125.15 (2006), p. 154509.
- [89] Toshiaki Iitaka and Toshikazu Ebisuzaki. “Methane hydrate under high pressure”. *Phys. Rev. B* 68.17 (2003), p. 172105.
- [90] Umbertoluca Ranieri et al. “Fast methane diffusion at the interface of two clathrate structures”. *Nature Comm.* 8 (2017), p. 1076.
- [91] L Bezacier et al. “Experimental investigation of methane hydrates dissociation up to 5GPa: Implications for Titan’s interior”. *Phys. Earth Planet. Inter.* 229 (2014), pp. 144–152.

- [92] J. S. Loveday. “Neutron Diffraction Studies of Ices and Ice Mixtures”. *High-Pressure Crystallography*. Ed. by Andrzej Katrusiak and Paul McMillan. Dordrecht: Springer Netherlands, 2004, pp. 69–80.
- [93] T. Tanaka et al. “Phase changes of filled ice Ih methane hydrate under low temperature and high pressure”. *J. Chem. Phys.* 139.10 (2013), p. 104701.
- [94] J Baumert et al. “Lattice dynamics of methane and xenon hydrate: Observation of symmetry-avoided crossing by experiment and theory”. *Phys. Rev. B* 68.17 (2003), p. 174301.
- [95] H Schober et al. “Guest-host coupling and anharmonicity in clathrate hydrates”. *Eur. Phys. J. E* 12 (2003), p. 41.
- [96] Thomas Meier et al. “Observation of Nuclear Quantum Effects and Hydrogen Bond Symmetrisation in High Pressure Ice”. *Nature Communications* 9 (July 2018).
- [97] Hirokazu Kadobayashi et al. “In situ Raman and X-ray diffraction studies on the high pressure and temperature stability of methane hydrate up to 55 GPa”. *J. Chem. Phys.* 148 (2018), p. 164503.
- [98] Lin Lin, Joseph A Morrone, and Roberto Car. “Correlated tunneling in hydrogen bonds”. *J. Stat. Phys.* 145.2 (2011), pp. 365–384.
- [99] Kenneth S Schweizer and Frank H Stillinger. “High pressure phase transitions and hydrogen-bond symmetry in ice polymorphs”. *J. Chem. Phys.* 80.3 (1984), pp. 1230–1240.
- [100] Frank Smallenburg and Francesco Sciortino. “Tuning the liquid-liquid transition by modulating the hydrogen-bond angular flexibility in a model for water”. *Physical review letters* 115.1 (2015), p. 015701.
- [101] Hannes Jónsson, Greg Mills, and Karsten W. Jacobsen. “Nudged Elastic Band Method for Finding Minimum Energy Paths of Transitions”. *Classical and Quantum Dynamics in Condensed Phase Simulations*. Ed. by G. Ciccotti B. J. Berne and D. F. Coker. Singapore: World Scientific, 1998.
- [102] H Hirai et al. “Solid methane behaviours under high pressure at room temperature”. *J. Phys.: Conf. Series*. Vol. 121. 2008, p. 102001.
- [103] JE Proctor et al. “Raman spectroscopy of methane (CH₄) to 165 GPa: Effect of structural changes on Raman spectra”. *J. Raman Spectr.* 48 (2017), p. 1777.
- [104] Guoying Gao et al. “Dissociation of methane under high pressure”. *J. Chem. Phys.* 133 (2010), p. 144508.
- [105] William M Haynes. *CRC handbook of chemistry and physics*. CRC press, 2014.
- [106] H-J Bleif and H Dachs. “Crystalline modifications and structural phase transitions of NaOH and NaOD”. *Acta Crystallographica Section A: Crystal Physics, Diffraction, Theoretical and General Crystallography* 38.4 (1982), pp. 470–476.
- [107] MP Krobok, PG Johannsen, and WB Holzapfel. “Raman and FTIR study of NaOH and NaOD under pressure”. *Journal of Physics: Condensed Matter* 4.41 (1992), p. 8141.
- [108] TJ Bastow et al. “Low Temperature Phase of NaOD”. *Zeitschrift für Naturforschung A* 41.1-2 (1986), pp. 283–285.
- [109] Mary Anne White and Stanley A Moore. “A calorimetric investigation of the low-temperature phase transition in NaOD”. *The Journal of chemical physics* 85.8 (1986), pp. 4629–4632.

- [110] Mizuhiko Ichikawa and Takasuke Matsuo. “Deuteration-induced structural phase transitions in some hydrogen-bonded crystals”. *Journal of molecular structure* 378.1 (1996), pp. 17–27.
- [111] TJ Bastow, MM Elcombe, and CJ Howard. “Low temperature phase transition in CsOH and CsOD”. *Solid state communications* 62.3 (1987), pp. 149–151.
- [112] DT Amm et al. “A low temperature phase transition in NaOD near 150 K”. *Thermochimica acta* 95.2 (1985), pp. 447–451.
- [113] James A Ibers, Junji Kumamoto, and Robert G Snyder. “Structure of Potassium Hydroxide: An X-Ray and Infrared Study”. *The Journal of Chemical Physics* 33.4 (1960), pp. 1164–1170.
- [114] H Jacobs et al. “Bonding conditions in crystalline phases of RbOH and RbOD”. *Zeitschrift fuer Anorganische und Allgemeine Chemie (1950)* 544 (1987).
- [115] Mary Anne White et al. “Thermodynamic characterization of the low-temperature phase transformations in KOH and KOD”. *The Journal of chemical physics* 89.7 (1988), pp. 4346–4348.
- [116] Paul WR Bessonette and Mary Anne White. “Why is there no low-temperature phase transition in NaOH?” *The Journal of chemical physics* 110.8 (1999), pp. 3919–3925.
- [117] Horst P Beck and Gunda Lederer. “High pressure transformations of NaOH”. *The Journal of chemical physics* 98.9 (1993), pp. 7289–7294.
- [118] William R Busing. “Infrared spectra and structure of NaOH and NaOD”. *The Journal of Chemical Physics* 23.5 (1955), pp. 933–936.
- [119] H Jacobs, J Kockelkorn, and Th Tacke. “Hydroxide des Natriums, Kaliums und Rubidiums: Einkristallzüchtung und röntgenographische Strukturbestimmung an der bei Raumtemperatur stabilen Modifikation”. *Zeitschrift für anorganische und allgemeine Chemie* 531.12 (1985), pp. 119–124.
- [120] Xin-Zheng Li, Brent Walker, and Angelos Michaelides. “Quantum nature of the hydrogen bond”. *Proceedings of the National Academy of Sciences* 108.16 (2011), pp. 6369–6373.
- [121] John Monteath Robertson and Alfred Rene Jean Paul Ubbelohde. “Structure and thermal properties associated with some hydrogen bonds in crystals I. The isotope effect”. *Proceedings of the Royal Society of London. Series A. Mathematical and Physical Sciences* 170.941 (1939), pp. 222–240.
- [122] K. Alex Müller and E. Berlinger W.and Tosatti. “Indication for a novel phase in the quantum paraelectric regime of SrTiO₃”. *Zeitschrift für Physik B Condensed Matter* 84.2 (1991), pp. 277–283.
- [123] R. Rousev and A. J. Millis. “Theory of the quantum paraelectric-ferroelectric transition”. *Phys. Rev. B* 67 (1 2003), p. 014105.
- [124] Paolo Giannozzi et al. “QUANTUM ESPRESSO: a modular and open-source software project for quantum simulations of materials”. *J. Phys.: Cond. Matt.* 21 (2009), p. 395502.
- [125] Michele Ceriotti, Joshua More, and David E. Manolopoulos. “i-PI: A Python interface for ab initio path integral molecular dynamics simulations”. *Computer Physics Communications* 189 (2014).
- [126] S. Grimme. “Semiempirical GGA-type density functional constructed with a long-range dispersion correction”. *J. Comput. Chem.* 27.15 (2006), pp. 1787–1799.
- [127] Michele Ceriotti and David E Manolopoulos. “Efficient first-principles calculation of the quantum kinetic energy and momentum distribution of nuclei”. *Phys. Rev. Lett.* 109 (2012), p. 100604.

- [128] Michele Ceriotti, David E Manolopoulos, and Michele Parrinello. “Accelerating the convergence of path integral dynamics with a generalized Langevin equation”. *J. Chem. Phys.* 134 (2011), p. 084104.
- [129] Fabien Briec, Hichem Dammak, and Marc Hayoun. “Quantum thermal bath for path integral molecular dynamics simulation”. *J. Chem. Th. Comp.* 12 (2016), p. 1351.
- [130] Christoph Schran, Fabien Briec, and Dominik Marx. “Converged Colored Noise Path Integral Molecular Dynamics Study of the Zundel Cation Down to Ultralow Temperatures at Coupled Cluster Accuracy”. *J. Chem. Th. Comp.* 14 (2018), p. 5068.
- [131] Sofiane Schaack et al. “Observation of methane filled hexagonal ice stable up to 150 GPa”. *PNAS* (Accepted).
- [132] Sofiane Schaack et al. “Quantum induced proton diffusion in Brucite minerals under high-pressure” (Submitted).
- [133] Sofiane Schaack et al. “How methane hydrate recovers at very high pressure the hexagonal ice structure.” (Submitted).
- [134] Sofiane Schaack et al. “The quantum equilibrium structure of NaOH.” (To be submitted).
- [135] Mathieu Moog et al. “Unsupervised Exploration of MoS₂Nanoclusters Configurations : Structures, Energetics, and Electronic Properties” (Submitted).

